JACOBS
UNIVERSITY

Advanced Detection Schemes of Digital Signals in Impulse Noise

by

Khodr Ahmad Saaifan

A thesis submitted in partial fulfillment

of the requirements for the degree of

Doctor of Philosophy
in Electrical Engineering

Approved, Dissertation Committee:

Prof. Dr.-Ing. Werner Henkel
Jacobs University Bremen

Prof. Dr.-Ing. A. J. Han Vinck
Universität Duisburg-Essen

Dr. rer. nat. habil. Mathias Bode
Jacobs University Bremen

Date of Defense: January 6, 2015

Abstract

In this thesis, we investigate the optimum approach to mitigate the effects of impulse noise in wireless communication channels. First, we present a measurement campaign to verify the statistical properties of a Middleton Class-A (MCA) model for impulse noise. This campaign measures wireless interference that corrupted a 2.4 GHz industrial, scientific, and medical (ISM) band. We extend this verification to characterize the spatial coupling and correlation of impulse noise for multiple antenna systems.

We then investigate the optimum detector for binary signals corrupted by MCA noise. We approximate the MCA model to a single weighted Gaussian density such that the nonlinearities of the optimum detector can be evaluated in a closed-form expression. The approximate MCA model discriminates the noise probability density function (PDF) of Gaussian and impulsive events using a threshold detection scheme. By means of such approximations, we provide a precise analysis for the behaviors of optimum nonlinearities in reducing the effects of impulse noise. We also introduce a decision boundary analysis to justify and analyze the performance of the optimum detector in different MCA noise environments. We also approximate the nonlinearities to investigate the behaviors of the other suboptimum detectors such as a locally optimum detector (LOD) and a clipping detector. As a suboptimum approach, we further approximate the optimum nonlinearities using linear segments to introduce new suboptimum detectors such as a piecewise linear detector and a clipping-like detector.

Next, we extend the approximate MCA model to derive the optimum combining schemes for time and space diversity in the presence of fading and impulse noise. We assume perfect knowledge of noise states to evaluate the analytical performances of the optimum combining schemes for time, receive, and transmit/receive diversity in Rayleigh fading and MCA noise. Although this assumption is unrealistic, it leads to a tight performance bound for the optimum combining schemes in impulse noise. These evaluations allow us to study the performance loss of spatial diversity with respect to the number of transmit and receive antennas.

Finally, we utilize the spectral dimensions in the mitigation problem of impulse noise for orthogonal frequency division multiplexing (OFDM) systems. We start with the receiver design of OFDM systems applied to fading channels with MCA noise, such as the optimum receiver and a conventional OFDM detector. We then evaluate an upper performance bound for the optimum receiver in flat fading with MCA noise. This analysis indicates a significant performance improvement of the optimum detector over a conventional OFDM detector in impulse noise. We finally develop a sphere decoding along with sparse Bayesian learning (SBL) to realize the optimum OFDM detector in MCA noise.

Acknowledgment

This work is the result of my research in the transmission system group at Jacobs University Bremen, Germany.

Foremost, I would like to express my deepest thanks to my supervisor Prof. Dr.-Ing. Werner Henkel. His patience, encouragement, and immense knowledge were key motivations throughout my PhD. I am deeply indebted to him, not only for his great support, but also for the spirit and the research liberty he gave me during my work in this thesis. Furthermore, I wish to thank Dr. Mathias Bode and Prof. Dr.-Ing. Han Vinck for accepting to join the dissertation committee.

I also would like to thank my colleagues Khaled Hassan, Oana Graur, Humberto Beltrão Neto, Hashem Ziyabar, Alexandra Filip, Fangning Hu, Abdul Wakeel, Jalal Etesami, Apirath Limmanee, Volodymyr Cherkashyn, Dawit Nigatu, and Nazia Islam for their company, confidence, valuable discussions, and support.

I would like to express my sincere love and special thanks to my wife Inas. Without her understanding and genuine support, this thesis would have remained a dream. I cannot forget my little kids, Ahmad and Juri. They have made my life full of happiness. This part would not be complete if I did not mention my late dad Ahmad and my mom Khawla. I could not forget their consistent prayers and moral support to make this work come true. Additionally, I would like to mention my brother Ibrahim, and sisters Zainab, Jumana, and Rema. Words cannot say enough to express their support and help.

Of course, I have to thank my friends, inside and outside Bremen, for making the years so enjoyable. This includes: Elkhouly, Foad, Raouf, Hussein, Azzez, Amin, Marwan, and Hamdy.

Finally, I would like to thank Jacobs University for providing the necessary environment and infrastructure. Additionally, I would like to thank the German Research Foundation (DFG) for their financial support.

Statutory Declaration

(on Authorship of a Dissertation)

I, Khodr Ahmad Saaifan hereby declare that I have written this PhD thesis independently, unless where clearly stated otherwise. I have used only the sources, the data and the support that I have clearly mentioned. This PhD thesis has not been submitted for conferral of degree elsewhere.

I confirm that no rights of third parties will be infringed by the publication of this thesis.

Bremen, June 30, 2015

Signature _____

Dedication

To my late father, my mother, and my wife Inas

Contents

List of Figures

Chapter 1

Introduction

Interference is one of the main factors that severely limits the performance of wireless communication systems. Since the communication channels are not interference-free media, the signal transmission is often corrupted by adding noise or interference, e.g., additive white Gaussian noise (AWGN), radio frequency interference (RFI), and co-channel radio interference. The sources of interference can be either natural or man-made such as natural atmospheric processes, switching transients of electrical devices, household appliance, car ignitions, etc. In environments with a large number of interfering sources, a Gaussian distribution dominates as a statistical model. A well-known example is an AWGN model. However, when the potential sources of interference emit strong impulses, the noise exhibits impulsive nature [1–3]. Thus, the AWGN model will not be accurate for modeling such interference.

Recent studies show sufficient evidences of impulse noise in indoor and outdoor wireless channels [1, 4, 5], wireless data transceivers deployed in laptops [6], co-channel interference [3, 7], and aeronautical communication systems [8–11]. One of the most important steps in the development of the signal detection in impulse noise environments is the statistical modeling of interference. The most accepted models for impulse noise are a Middleton Class-A (MCA) model and symmetric alpha-stable (S$\boldsymbol{\alpha}$S) distributions [1, 12]. The MCA and SαS models are derived for a Poisson distributed interferer under bounded and unbounded path-loss assumptions [1, 13], respectively. Since the unbounded path-loss assumption of the SαS model is not realistic, the MCA model appears to be more physically relevant.

The effects of impulse noise on the operation of a communication system designed under the assumption of AWGN are drastic. This elevates the need for redesigning communication systems to effectively differentiate the signal from noise. The researchers have

been working hard on the development of a communication system over impulse noise channels [14–17]. A signal detection in MCA noise shows that the optimum detector provides a significant performance improvement over a conventional detector [14], even though the impulse noise is strong. However, the research towards the optimum approach is limited so far.

One of the research directions for mitigating the effects of impulse noise is to use time and spatial dimensions such as time diversity, space diversity, and space-time (ST) coding. However, conventional combining schemes of diversity could not maintain the same diversity advantages in MCA noise [18, 19]. Therefore, one of the challenging problems is to exploit the advantages of the optimum combining scheme for fading channels in the presence of impulse noise. The same challenge is observed in orthogonal frequency division multiplexing (OFDM) systems, which suffer severely in strong impulse noise, since then, the spreading effect is actually a disadvantage in contrast to weaker impulse noise.

This thesis introduces a modern study of the optimum detection schemes in the presence of MCA noise. We treat the effects of impulse noise using time, space, and frequency dimensions. Since the available physical modeling of MCA noise is limited to two receive antennas, impulse noise measurements are required to verify and extend the MCA model for an arbitrary number of receive antennas.

1.1 Statistical Models of Impulse Noise

The statistical modeling of impulse noise leads to heavy-tailed distributions as models for the amplitude distribution of impulse noise. The tails of these distributions decay at a rate less than those of a Gaussian distribution, which admits a large number of models. The existing models of impulse noise are classified as either empirical models or statistical-physical models. On the one hand, the empirical models provide tractable distributions, which fit the statistical distributions of measured data. On the other hand, the statistical-physical models admit more accurate and complex distributions whose parameters have a direct physical significance. In this section, we have looked on the most accepted models for impulse noise, such as the MCA model, the SαS distribution, a Gaussian mixture model, and generalized Gaussian distributions.

1.1.1 The Middleton's Class-A Model

In 1972, Middleton developed three analytical models for impulsive effects of RFI [1,20,21]. Among them, the Class-A model is the most accepted one for impulse noise superimposed

to AWGN. The MCA model assumes that the received interference, $w(t) = w_G(t) + w_I(t)$, consists of two additive noise components: a Gaussian component $w_G(t)$ and an impulsive component $w_I(t)$. The Gaussian component is thought to represent AWGN while the second part comprises impulsive events. The probability density function (PDF) of a real-valued noise observation, w, is given by [1]

$$p_w(w) = \sum_{m=0}^{\infty} \frac{\alpha_m}{\sqrt{2\pi\sigma_m^2}} \mathrm{e}^{-\frac{w^2}{2\sigma_m^2}} , \tag{1.1}$$

where

$$\alpha_m = \frac{A^m \mathrm{e}^{-A}}{m!} , \tag{1.2}$$

and

$$\sigma_m^2 = \sigma^2 \frac{m/A + \Upsilon}{1 + \Upsilon} . \tag{1.3}$$

The average variance of the MCA process is defined by $\sigma^2 = \sigma_G^2 + \sigma_I^2$, where σ_G^2 and σ_I^2 are the variances of $w_G(t)$ and $w_I(t)$, respectively. The MCA model is defined using two parameters A and Υ, which are related to the underlying physical process generating the impulse noise. The impulse index, A, represents the mean number of impulses that occur in a specified time interval. The Gaussian factor, $\Upsilon = \sigma_G^2/\sigma_I^2$, defines the Gaussian to impulse noise power ratio. The term $A\Upsilon$ controls the impulsiveness of MCA noise. In (1.1), we note that the MCA density is a weighted linear combination of an infinite number of Gaussian densities with different variances, σ_m^2. The weights of Gaussian densities, α_m, $\forall m$, can be seen as a Poisson distribution of a random variable m. For this reason, m sometimes refers to the noise states of MCA noise, i.e., $m = 0$ is a Gaussian state and $m > 1$ represent the impulsive states. Mathematically, the average variance of MCA noise can be obtained as

$$\begin{aligned} \mathrm{E}\{w^2\} &= \sum_{m=0}^{\infty} \alpha_m \sigma_m^2 , \\ &= \sigma^2 . \end{aligned} \tag{1.4}$$

In Fig. 1.1, we depict the MCA distribution with different values of A and Υ. From this figure, we observe that the tails of the MCA density become wider for ΥA below 1. However, when ΥA is increased to infinity, the variance σ_m^2 in (1.3) converges to σ^2. Therefore, the tails of the MCA density asymptotically approach those of a Gaussian density with variance σ^2. The applications of MCA models have been seen in the modeling of interference by the switching transients in power lines, car ignition, and home appliances. The MCA model also approximates multiuser interference in ultra-

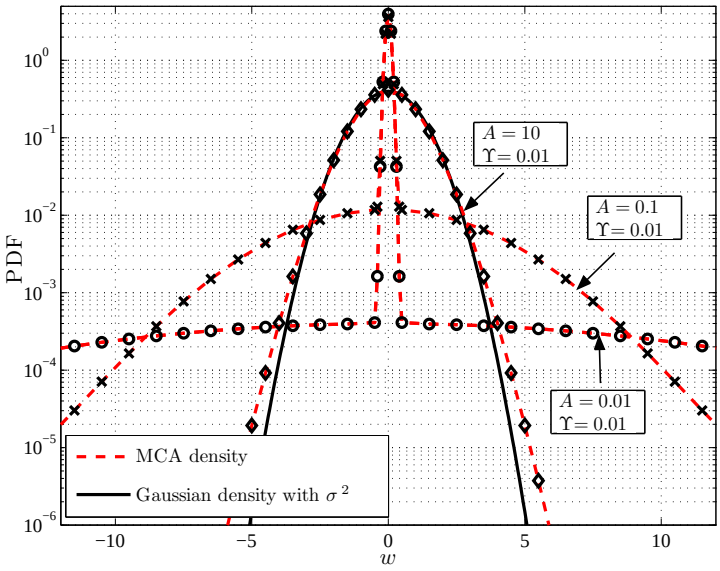

Figure 1.1: PDF of MCA noise with different values of Υ and A. Note that the noise variance, σ^2, is unity

wideband communication systems [22]. Besides the MCA model, Middleton proposes two additional models for broadband impulse noise. A Middleton Class-B model is used for interference whose spectrum is broader than a receiver bandwidth. A Class-C noise is a mixture of Class-A and Class-B interference. The practical application of the Middleton Class-B model is limited because it has a complex density function, which requires up to 5 parameters.

1.1.2 The Symmetric Alpha-Stable Model

The $S\alpha S$ model captures the impulsive phenomena that encountered in many applications such as digital communications, biomedicine, and radar. The $S\alpha S$ model lacks of a closed-form expression for its PDF. Then, the best description of the $S\alpha S$ model can be given by its characteristic function [12, 13, 23]

$$\varphi(\varpi) = \exp\left(j\upsilon\varpi - \gamma|\varpi|^{\alpha}\right) , \tag{1.5}$$

where $0 < \alpha \leq 2$ is the characteristic exponent, υ $(-\infty < \upsilon < \infty)$ is the location parameter, and γ $(\gamma > 0)$ is the dispersion of the distribution. When $1 < \alpha \leq 2$, the location parameter υ corresponds to the mean of the $S\alpha S$ distribution, while for $0 < \alpha \leq 1$, υ corresponds to its median. The parameter γ determines the spread of the distribution around its location parameter υ, which is similar to the variance of the Gaussian distribution. The characteristic exponent α is the most important parameter

of the $S\alpha S$ distribution, which controls the tails of the distribution. Figure 1.2 depicts the $S\alpha S$ distribution for different values of α. We observe that a smaller α corresponds to heavier tails of the $S\alpha S$ density. This implies that the random variables of small

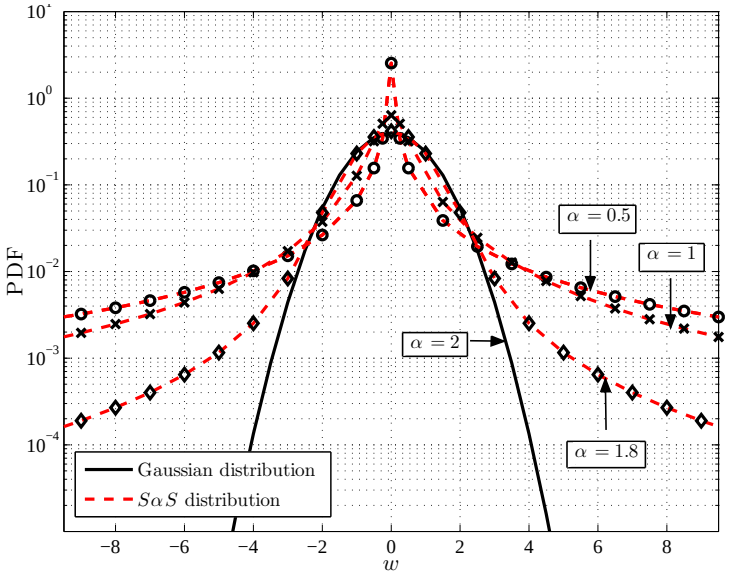

Figure 1.2: PDF of $S\alpha S$ noise with different values of α.

characteristic exponents are highly impulsive. There are two important special cases of $S\alpha S$ distributions. When $\alpha = 1$, the distribution reduces to a Cauchy distribution with parameters γ and υ. When $\alpha = 2$, the distribution reduces to a Gaussian distribution with mean υ and variance 2γ.

The $S\alpha S$ distributions, except for the Gaussian case, possess unrealistic assumptions regarding the infinite variance of interference. Since in practice the variances are always bounded, the $S\alpha S$ seems to be unrealistic for communication systems. However, the $S\alpha S$ model can potentially be used to approximate the Middleton Class-B model in the absence of Gaussian noise. The co-channel interference for spatially Poisson-distributed interferers reduces to the $S\alpha S$ distribution [3,7]. The same seems to be true in a multiple access system and for back-scattered echos in radar systems [24].

1.1.3 The ε-Mixture Model

The ε-mixture model is a commonly used empirical model for impulse noise. This model can be written as a weighted sum of two or more Gaussian distributions. A large number of Gaussian terms yields a non-tractable model. However, two terms are being sufficient

in most problems [25, 26]. The ε-mixture density of two Gaussian terms is given as [27]

$$p_w(w) = \frac{1-\varepsilon}{\sqrt{2\pi\sigma_0^2}} \mathrm{e}^{-\frac{w^2}{2\sigma_0^2}} + \frac{\varepsilon}{\sqrt{2\pi\sigma_1^2}} \mathrm{e}^{-\frac{w^2}{2\sigma_1^2}} , \tag{1.6}$$

where $0 < \varepsilon < 1$ represents the probability of having impulses. The ratio σ_1^2/σ_0^2 should be chosen high enough to broaden the tails of the mixture density. The ε-mixture can approximate a wide variety of symmetric zero-mean random variables, such as the Laplacian distribution [28] and the $S\alpha S$ distribution [26]. In contrast to the MCA model, the second term of (1.6) is thought to approximate the impulsive terms $m \geq 1$ of the MCA density. The relations between both models can be given as [16]

$$\frac{\sigma_1^2}{\sigma_0^2} = 1 + \frac{1}{A\Upsilon} , \tag{1.7}$$

and

$$\varepsilon = 1 - \mathrm{e}^{-A} . \tag{1.8}$$

In the general description of ε-mixture model, the second term can be any symmetric PDF, e.g., Cauchy or Laplacian, instead of Gaussian [29].

1.1.4 Generalized Gaussian Distributions

A generalized Gaussian distribution has been considered as an alternative to the $S\alpha S$ model [30]. The generalized Gaussian model is used to model multiple access interference in spread spectrum communications [31]. Furthermore, the asymmetric generalized Gaussian distribution provides an accurate modeling for underwater acoustic data transmission [32]. The tails of the generalized Gaussian distribution decline exponentially, meaning that it is not as heavy-tailed as the $S\alpha S$ distribution. The generalized Gaussian distribution can be expressed as

$$p_w(w) = \frac{\kappa}{2\sigma^2\Gamma(1/\kappa)} \mathrm{e}^{-\frac{|w-\mu|^\kappa}{\sigma^2}} . \tag{1.9}$$

where $\Gamma(\cdot)$ is the gamma function. The above distribution has three parameters μ, κ, and σ^2. The parameters κ and $\sigma^2 > 0$ denote the shape and variance, respectively. The distribution goes to Gaussian when $\kappa = 2$, and it reduces to Laplacian when $\kappa = 1$. The generalized Gaussian distribution with $\mu = 0$ and $\kappa = 1/5$ reduces to an HK (Henkel/Kessler) model [33, 34]. The HK model was investigated empirically to model

impulse noise on twisted pairs. This model has been found to be a good fit for all measured impulse noise collected in the networks of Deutsche Telekom and British Telecom.

1.2 Signal Detection in Impulse Noise

The detection problems of binary signals corrupted by impulse noise are considered in many works [14,16,17,26,27]. In general, the optimum receiver in the presence of impulse noise requires a high computational complexity. In [35], the decision region analysis is introduced as a new approach to depict the typical nonlinearity of the optimum detector in $S\alpha S$ noise. Moreover, this approach has been investigated to clarify the behavior of suboptimum detectors, such as a linear detector, a clipping detector, and a blanking detector. However, the optimum nonlinearity has hitherto not been known for binary signals corrupted by MCA noise. Herewith, we consider a classical detection problem of binary signals in MCA noise. Similar to prior works, we assume that the observation space consists of several observations (N samples) of the same transmitted signals corrupted by statistically independent noise observations. The hypothesis S_1 corresponds to a transmitted signal $+B$, and the hypothesis S_0 corresponds to a transmitted signal $-B$. Under both hypotheses, we have

$$\begin{matrix} S_1 : y_k = +B + w_k \\ S_0 : y_k = -B + w_k \end{matrix}, \quad k = 1, \cdots, N \,, \tag{1.10}$$

where $B = \sqrt{\frac{E_b}{N}}$. Thus, the noise observations, w_k, are samples of a real-valued MCA noise process with average variance σ^2. For equiprobable transmitted signals $+B$ and $-B$, the maximum-likelihood (ML) detector computes the log-likelihood ratio (LLR) as

$$\Lambda_{ML} = \log\left(\frac{\prod_{k=1}^{N} p_w(y_k - B)}{\prod_{k=1}^{N} p_w(y_k + B)}\right) \underset{S_0}{\overset{S_1}{\gtrless}} 0 \,, \tag{1.11}$$

where

$$p_w(w_k) = \sum_{m=0}^{\infty} \frac{\alpha_m}{\sqrt{2\pi\sigma_m^2}} \mathrm{e}^{-\frac{w_k^2}{2\sigma_m^2}} \,, \tag{1.12}$$

is the MCA density of received noise. In the following subsections, we consider two types of detection schemes. One is based on the ML detection criterion, which is optimum from a theoretical perspective. A second type is suboptimum, such as a conventional detector, a locally optimum detector (LOD), and a clipping detector.

1.2.1 Optimum Detector

The performance of the optimum detector is quantitatively studied in [14]. The optimum decision rule (1.11) can be rewritten as

$$\Lambda_{ML} = \sum_{k=1}^{N} g(y_k) \underset{S_0}{\overset{S_1}{\gtrless}} 0 \ , \tag{1.13}$$

where

$$g(y_k) = \log\left(p_w(y_k - B)\right) - \log\left(p_w(y_k + B)\right) \ , \tag{1.14}$$

denotes the optimum nonlinearity. The previous expression indicates that the optimum detector comprises of a set of nonlinear operations, $g(y_k)$, followed by a linear decision rule as illustrated in Fig. 1.3. From (1.14) and (1.12), we observe that the optimum

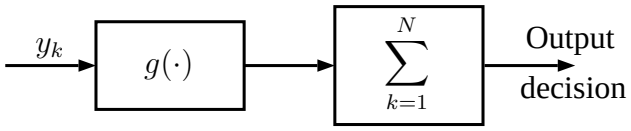

Figure 1.3: A nonlinear structure of the optimum detector

nonlinearity, $g(y_k)$, requires a high computational complexity because of the sum of many exponential terms. To reduce the complexity, the MCA density can be approximated by the maximum value of the first few terms [17, 36]. Accordingly, the natural logarithm of the likelihood functions, $p_w(y_k \pm B)$, can be approximated as

$$\begin{aligned} \log\left(p_w(y_k \pm B)\right) &\approx \max_{m=0,1,2} \left\{ \log\left(\frac{\alpha_m}{\sqrt{2\pi\sigma_m^2}} \mathrm{e}^{-\frac{(y_k \pm B)^2}{2\sigma_m^2}} \right) \right\} \ , \\ &\approx \max_{m=0,1,2} \left\{ -\frac{(y_k \pm B)^2}{2\sigma_m^2} + \log\left(\frac{\alpha_m}{\sqrt{2\pi\sigma_m^2}} \right) \right\} \ . \end{aligned} \tag{1.15}$$

This approximation offers a practical realization of the optimum nonlinearity. However, it does not explain how the optimum nonlinearity treats the effects of impulse noise.

1.2.2 Suboptimum Detectors

In (1.14), we observe that the natural logarithm of $p_w(y_k - B)$ and $p_w(y_k + B)$ could not simplify further the optimum nonlinearity, $g(y_k)$. However, approximating the likelihood functions $p_w(y_k - B)$ and $p_w(y_k + B)$ leads to several suboptimum solutions.

Linear detector: This scheme assumes that the noise is Gaussian, and hence, it ignores all impulsive terms of the MCA model, i.e., $\alpha_m = 0$, $m \geq 1$. Thus, the likelihood functions $p_w(y_k - B)$ and $p_w(y_k + B)$ are Gaussian, which leads to

$$\begin{aligned} g_{LD}(y_k) &= \log\left(\frac{1}{\sqrt{2\pi\sigma_0^2}}\mathrm{e}^{-\frac{(y_k-B)^2}{2\sigma_0^2}}\right) - \log\left(\frac{1}{\sqrt{2\pi\sigma_0^2}}\mathrm{e}^{-\frac{(y_k+B)^2}{2\sigma_0^2}}\right) , \\ &= \frac{2B}{\sigma_0^2}y_k , \quad k = 1 , \cdots , N . \end{aligned} \tag{1.16}$$

Thus, the linear detector $\sum_{k=1}^{N} g_{LD}(y_k)$ possesses a single linear operation, which has an inferior performance in impulse noise [14].

Locally optimum detector: The LOD provides a closed-form approximation of the optimum nonlinearity for small signal levels B. This detector uses a Taylor series expansion of $\log\left(p_w(y_k \pm B)\right)$ around $B \approx 0$, which yields

$$\log\left(p_w(y_k \pm B)\right) = \log\left(p_w(y_k)\right) \pm B\frac{d}{1!dy_k}\log\left(p_w(y_k)\right) + B^2\frac{d^2}{2!dy_k^2}\log\left(p_w(y_k)\right) \pm \cdots . \tag{1.17}$$

Inserting (1.17) into (1.14), ignoring all signal terms of order 2 and higher, we obtain

$$g_{LO}(y_k) = -2B\frac{d}{dy_k}\log\left(p_w(y_k)\right) , \quad k = 1 , \cdots , N . \tag{1.18}$$

The performance of the LOD is almost optimum for small signals, but it becomes suboptimum at high signal levels [14].

Clipping detector: A clipping nonlinearity was proposed to remove the dependence of the LOD on the MCA density [15]. The clipping nonlinearity limits the received signal amplitudes (containing noise) to a certain value γ_c. The clipping detector is simple since it adds almost no complexity to the linear detector. The clipping nonlinearity can be given as

$$g_{CD}(y_k) = \begin{cases} y_k , & |y_k| < \gamma_c , \\ \gamma_c \mathrm{e}^{j\arg(y_k)} , & \text{elsewhere} . \end{cases} \tag{1.19}$$

From (1.19), we observe that the operations of the clipping detector are strongly depending on the choice of the threshold γ_c. A too high γ_c leads to a linear detector, whereas an extremely low one may distort the received signal. There are two methods for finding the optimum level of γ_c. One method is to evaluate the threshold which maximizes the signal-to-noise ratio (SNR) at the output of the clipping operation. This method does not guarantee a closed-form expression for γ_c [37] even for the simple Gaussian mixture

model. The second method optimizes the threshold, which clips the received observations that affected by impulse noise [38, 39]. For an MCA model with 2 terms $m = 0$ and $m = 1$, the probability that the received observation, due to the impulsive term, exceeds a threshold γ can be given as [39]

$$P(|y_k| \geq \gamma | m = 1) = 2 \int_{\gamma}^{\infty} \frac{1}{\sqrt{2\pi\sigma_1^2}} \mathrm{e}^{-\frac{(y_k - B)^2}{2\sigma_1^2}} dy_k = \mathrm{erfc}\left(\frac{\gamma - B}{\sqrt{2\sigma_1^2}}\right) , \tag{1.20}$$

where $\mathrm{erfc}(\cdot)$ is the complementary error function. However, when the samples are corrupted by a Gaussian term, the probability that y_k exceeding γ can be given as

$$P(|y_k| \geq \gamma | m = 0) = 2 \int_{\gamma}^{\infty} \frac{1}{\sqrt{2\pi\sigma_0^2}} \mathrm{e}^{-\frac{(y_k - B)^2}{2\sigma_0^2}} dy_k = \mathrm{erfc}\left(\frac{\gamma - B}{\sqrt{2\sigma_0^2}}\right) . \tag{1.21}$$

In [39], the optimum γ is selected to maximize the combination of (1.20) and (1.21) as follows:

$$\gamma_c = \arg\max_{\gamma > B} \left\{ \alpha_1 P(|y_k| \geq \gamma | m = 1) - \alpha_0 P(|y_k| \geq \gamma | m = 0) \right\} , \tag{1.22}$$

where α_m is the probability of a noise state m. This yields

$$\gamma_c = B + \sqrt{\frac{2\sigma_0^2 \sigma_1^2}{\sigma_1^2 - \sigma_0^2} \log\left(\frac{\alpha_0 \sigma_1}{\alpha_1 \sigma_0}\right)} . \tag{1.23}$$

Therefore, this method shows that the threshold γ_c depends on a signal level B and noise parameters. However, the clipping nonlinearity has no additional advantages over a linear detector when the signal level B goes to high values [14, 15].

1.3 Impulse Noise Mitigation Across Time, Space, and Frequency

Diversity is one of the most attractive techniques to combat the detrimental effects of fading in wireless channels. Diversity schemes use the available dimensions, such as time, space, and frequency, to supply the receiver with several replicas of the same transmit signal. In this section, we present prior works for mitigating the effects of fading and impulse noise through these dimensions. We begin with the time diversity approach of binary signals in fading channels with impulse noise [19]. Then, for space diversity, we look into both transmit and receive diversity schemes in both fading and impulse noise [18, 19, 40]. However, when it comes to frequency, we investigate the mitigation

schemes for impulse noise in OFDM systems [37, 41, 42]. Some recent studies show that the null-subcarriers of the OFDM systems can be used for impulse noise estimation [43,44]. Therefore, we further discuss this approach for OFDM signals corrupted by MCA noise.

1.3.1 Time Diversity

Time diversity utilizes several time slots to supply the receiver with replicas of the same transmit signal. Figure 1.4 illustrates a digital communication system with time diversity. We restrict this model to a binary signal set. However, the extension to an M-ary signal set is straight forward. At a time slot t_{n_D}, $n_D = 1, \cdots, N_D$, the transmitter uses rectangular

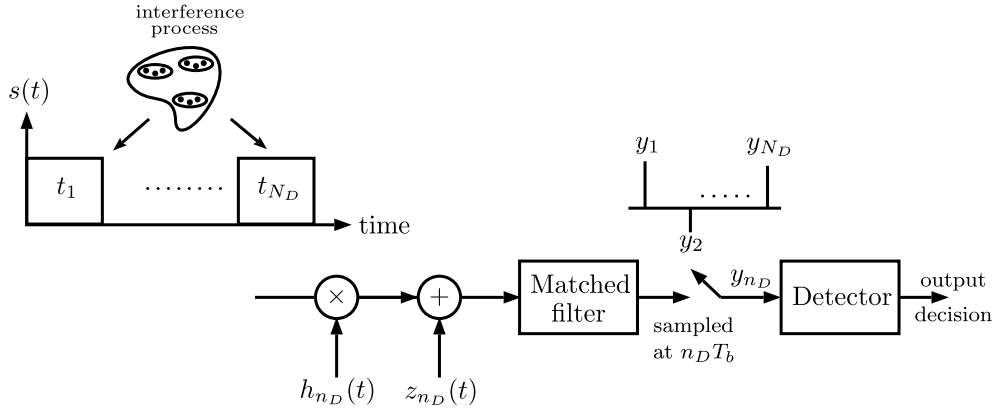

Figure 1.4: A baseband model for binary signal transmission over fading channels with impulse noise

pulses, $s(t) = \frac{1}{\sqrt{T_b}}\text{rect}\left(\frac{t-t_{n_D}}{T_b}\right)$, to transmit binary antipodal signals $+s(t)$ and $-s(t)$ over a signaling interval, T_b. The transmitted signals are assumed to undergo frequency non-selective slowly fading channels. This means that the coefficients of the fading channels remain constant during the signaling interval T_b. Thus, the received signals for the N_D time slots can be given as

$$y_{n_D}(t) = \pm\sqrt{\frac{E_b}{N_D}}h_{n_D}s(t) + z_{n_D}(t)\ , \quad n_D = 1, 2, \cdots, N_D\ , \tag{1.24}$$

where h_{n_D} represents the fading coefficient of a complex Gaussian channel for the n_D^{th} time slot. To guarantee independent fading coefficient between different time slots, the separation between two consecutive time slots should be greater than the coherence time of the channel [45]. $z_{n_D}(t)$ is a complex-valued MCA noise process in the n_D^{th} signaling interval. Since the received signals, $y_{n_D}(t)$, is passed through a matched filter followed by

a sampler. The received signal observations can be given as

$$y_{n_D} = \pm\sqrt{\frac{E_b}{N_D}}h_{n_D} + z_{n_D} \ , \quad n_D = 1, 2, \cdots, N_D \ , \tag{1.25}$$

where z_{n_D}, $n_D = 1, \cdots, N_D$, represent the samples of a complex-valued MCA process at the output of matched-filtering for the N_D time slots. Under the assumption that the duration of impulsive waveforms comprising $z_{n_D}(t)$ is less than or equal to T_b, the noise samples, z_{n_D}, at different time slots can be assumed statistically independent[1]. The complex-valued MCA process is given as [18, 19]

$$p_z(z_{n_D}) = \sum_{m=0}^{\infty} \frac{\alpha_m}{2\pi\sigma_m^2} \mathrm{e}^{-\frac{|z_{n_D}|^2}{2\sigma_m^2}} \ , \tag{1.26}$$

where $z_{n_D} = z_{\mathrm{I}n_D} + jz_{\mathrm{Q}_{n_D}}$. In this case, the average power of the baseband MCA noise process is $\mathrm{E}\{|z_k|^2\} = 2\sigma^2$. There are several combining methods, which treat the effects of impulse noise and fading [19]. In the following, we briefly discuss those schemes for binary signals in fading channels with complex-valued MCA noise.

Conventional schemes: The conventional combining schemes, such as maximum ratio combining (MRC), selection combining, and equal gain combining are well-known schemes for combating the effects of fading in AWGN. These schemes possess simple realizations. However, they provide a limited performance in fading channels with impulse noise [19]. The MRC scheme is simply

$$\Lambda_{MRC} = \sum_{n_D=1}^{N_D} h_{n_D}^* y_{n_D} \underset{S_0}{\overset{S_1}{\gtrless}} 0 \ . \tag{1.27}$$

From (1.27), we note that MRC weights the signal observations according to the gain of fading, which is a suboptimum method for treating the effects of MCA noise.

Optimum combining: The optimum detector of binary signals in fading channels and

[1]When the transmitted signals are separated enough over time, we can assume independent channels for both fading and interference processes.

MCA noise computes

$$\begin{aligned}\Lambda_{ML} &= \log\left(\frac{\prod_{n_D=1}^{N_D} p_z\left(y_{n_D}-\sqrt{\frac{E_b}{N_D}}h_{n_D}\right)}{\prod_{n_D=1}^{N_D} p_z\left(y_{n_D}+\sqrt{\frac{E_b}{N_D}}h_{n_D}\right)}\right) \underset{S_0}{\overset{S_1}{\gtrless}} 0\ , \\ &= \sum_{n_D=1}^{N_D} g(y_{n_D},h_{n_D}) \underset{S_0}{\overset{S_1}{\gtrless}} 0\ ,\end{aligned} \tag{1.28}$$

where

$$g(y_{n_D},h_{n_D}) = \log\left(p_z\left(y_{n_D}-\sqrt{\tfrac{E_b}{N_D}}h_{n_D}\right)\right) - \log\left(p_z\left(y_{n_D}+\sqrt{\tfrac{E_b}{N_D}}h_{n_D}\right)\right)\ , \tag{1.29}$$

denotes the nonlinearity of the optimum combining scheme. We observe that the above nonlinearities possess a complex representation of the MCA noise density. Therefore, the LOD and the clipping detector can easily be developed as a suboptimum solution for binary signals in fading channels and impulse noise.

1.3.2 Spatial Diversity

Antenna diversity uses spatial dimensions by employing multiple transmit and/or receive antennas to supply the receiver with several replicas of the same transmit signal. Since the antennas are often spaced far enough, the fading gains between different antenna pairs can be assumed statistically independent. This assumption may not hold true for impulse noise at different receive antennas. Since the receive antennas are victims to the same physical interference process, the statistical-physical modeling of MCA noise proved that the noise observations for 2-receive antennas are dependent and may be correlated [46]. The algebraic extension of this model leads to a multivariate Class-A distribution, which can be used for an arbitrary number of receive antennas [18]. In this section, we consider a receiver design for spatial diversity using multiple receive antennas, and transmit/receive diversity using multiple-input multiple-output (MIMO) channels in the presence of MCA noise.

1.3.2.1 Receive Diversity

We consider a communication system equipped with a single transmit antenna and N_R receive antennas (see Fig. 1.5). The received signal at the N_R receive antennas can be

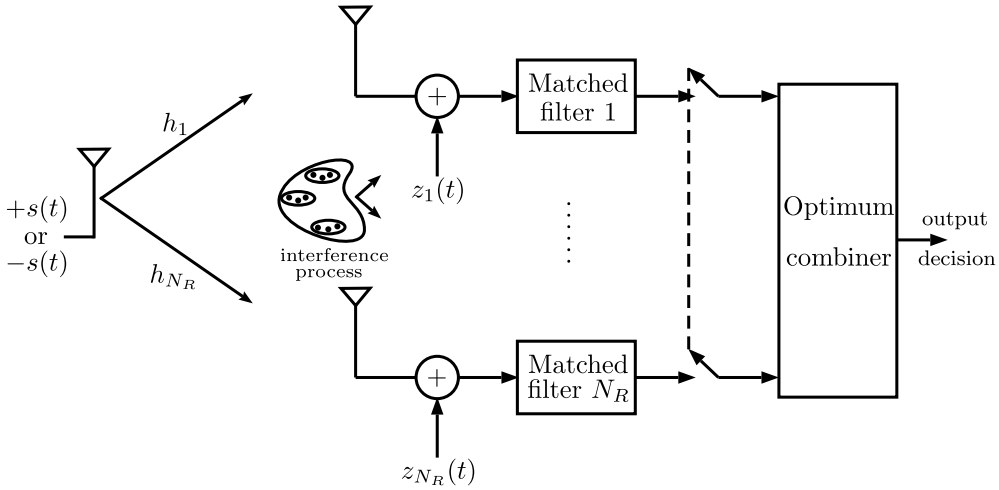

Figure 1.5: A baseband model for binary signal transmission with space diversity

expressed as

$$y_{n_R}(t) = \pm\sqrt{E_b}h_{n_R}s(t) + z_{n_R}(t)\ , \quad n_R = 1, 2, \cdots, N_R\ , \tag{1.30}$$

where $+s(t)$ and $-s(t)$ are the transmit antipodal signals. h_{n_R}, $n_R = 1, \cdots, N_R$, are complex-valued fading coefficients for the N_R channels. $z_{n_R}(t)$ represents the interference process as seen by the n_R^{th} receive antenna. After matched-filtering, the received observations, y_{n_R}, can be given as

$$y_{n_R} = \pm\sqrt{E_b}h_{n_R} + z_{n_R}\ , \quad n_R = 1, 2, \cdots, N_R\ , \tag{1.31}$$

where z_{n_R} denotes a complex baseband impulse noise sample. Since the noise observations, z_{n_R}, $n_R = 1, \cdots, N_R$, comprise of impulse noise of the same physical sources, the noise samples for different receive antennas are jointly dependent. For 2-receive antennas, a bivariate MCA distribution is derived as the statistical-physical model for the received noise vector, $\mathbf{z} = [z_1,\, z_2]^T$, as [46]

$$p_{\mathbf{z}}(\mathbf{z}) = \frac{\mathrm{e}^{-A}}{(2\pi)^2|\mathbf{\Sigma}_0|}\mathrm{e}^{-\frac{1}{2}\mathbf{z}^H{\mathbf{\Sigma}_0}^{-1}\mathbf{z}} + \frac{1-\mathrm{e}^{-A}}{(2\pi)^2|\mathbf{\Sigma}_1|}\mathrm{e}^{-\frac{1}{2}\mathbf{z}^H{\mathbf{\Sigma}_1}^{-1}\mathbf{z}}\,, \tag{1.32}$$

where $|\cdot|$ denotes a determinant, and $(\cdot)^H$ represents the conjugate transpose. $\mathbf{\Sigma}_0$ and $\mathbf{\Sigma}_1$ are the covariance matrices of the Gaussian and impulse terms, respectively. Hence, $\mathbf{\Sigma}_m$, $m = 0,\, 1$, are given as

$$\mathbf{\Sigma}_m = \begin{pmatrix} \sigma_{m,1}^2 & \rho_m\sigma_{m,1}\sigma_{m,2} \\ \rho_m\sigma_{m,2}\sigma_{m,1} & \sigma_{m,2}^2 \end{pmatrix}\,, \tag{1.33}$$

where

$$\sigma^2_{m,n_R} = \sigma^2_{n_R} \frac{m/A + \Upsilon_{n_R}}{1 + \Upsilon_{n_R}}, \quad n_R = 1, 2, \tag{1.34}$$

and ρ_m is the correlation coefficient of noise observations z_1 and z_2. Since $\sigma^2_{n_R} = \sigma^2_G + \sigma^2_I$, and $\sigma^2_I = \sigma^2_G/\Upsilon_{n_R}$, the above model implies that the received interference, $z_{n_R}(t)$, $\forall n_R$, are possessing unequal Gaussian factors Υ_{n_R} at the 2-receive antennas. For an arbitrary number of receive antennas, N_R, a multivariate MCA distribution [18, 19] can be used as

$$p_{\mathbf{z}}(\mathbf{z}) = \sum_{m=0}^{\infty} \frac{\alpha_m}{(2\pi)^{N_R}|\mathbf{\Sigma}_m|} \mathrm{e}^{-\frac{1}{2}\mathbf{z}^H {\mathbf{\Sigma}_m}^{-1} \mathbf{z}}, \tag{1.35}$$

where $\mathbf{\Sigma}_m$ is given as

$$\mathbf{\Sigma}_m = \begin{pmatrix} \sigma^2_{m,1} & \cdots & 0 \\ \vdots & \ddots & \vdots \\ 0 & \cdots & \sigma^2_{m,N_R} \end{pmatrix}. \tag{1.36}$$

From (1.36), it is obvious that the noise observations, z_{n_R}, $n_R = 1, \cdots, N_R$, are dependent but uncorrelated. When $\Upsilon_{n_R} = \Upsilon$, $\forall n_R$, the model in (1.35) reduces to a balanced multivariate MCA distribution [19]. The optimum combining scheme of receive diversity computes the following statistics

$$\Lambda_{ML} = \log \left(\frac{p_{\mathbf{z}}(\mathbf{y} - \sqrt{E_b}\mathbf{h})}{p_{\mathbf{z}}(\mathbf{y} + \sqrt{E_b}\mathbf{h})} \right) \underset{S_0}{\overset{S_1}{\gtrless}} 0, \tag{1.37}$$

where $\mathbf{h} = [h_1, \cdots, h_{N_R}]^T$ is the channel vector. The prior works show that MRC approximates the optimum combining scheme for balanced multivariate MCA noise [19]. However, it is not obvious how the optimum scheme should behave in correlated and unbalanced MCA noise.

1.3.2.2 Transmit/Receive Diversity

MIMO refers to the transmission over radio links formed by multiple transmit and receive antennas. Figure 1.6 depicts a MIMO system equipped with N_T transmit and N_R receive antennas. One of the key advantages of the MIMO system lies in the ability of achieving transmit diversity. Herewith, we consider an orthogonal ST coding scheme, which provides a full diversity gain in Rayleigh fading with AWGN channels. The ST coding uses N_D time slots to encode a block of $N_B \leq N_T$ information symbols, s_{n_B}, $n_B = 1, \cdots N_B$, into

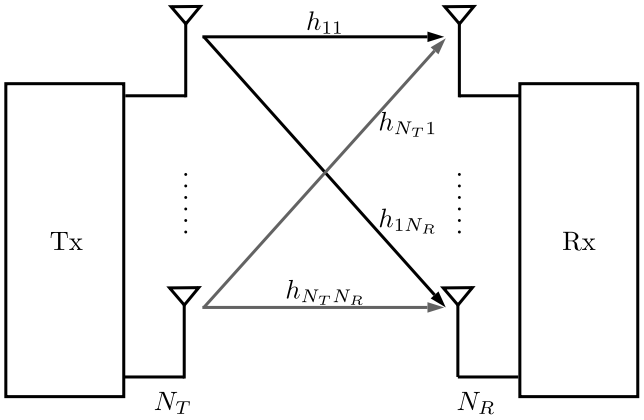

Figure 1.6: MIMO Systems

a ST code matrix, $\mathbf{C} \in \mathbb{C}^{N_T \times N_D}$, as

$$\mathbf{C} = \begin{pmatrix} c_{1,1} & c_{1,2} & \cdots & c_{1,N_D} \\ c_{2,1} & c_{2,2} & \cdots & c_{2,N_D} \\ \vdots & \vdots & \ddots & \vdots \\ c_{N_T,1} & c_{N_T,2} & \cdots & c_{N_T,N_D} \end{pmatrix} , \tag{1.38}$$

where the entries c_{n_T,n_D} denote the coded symbols transmitted from the n_T^{th} transmit antenna during the n_D^{th} time slot. The Alamouti's ST transmission scheme is one of the most famous orthogonal ST block codes. The Alamouti's ST code matrix can be given as [47]

$$\mathbf{C}_2 = \begin{pmatrix} s_1 & -s_2^* \\ s_2 & s_1^* \end{pmatrix} , \tag{1.39}$$

where the information symbols s_1 and s_2 are taken from a complex signal set such as PSK or QAM. The Alamouti scheme achieves full transmit diversity for two transmit antennas. The orthogonal ST block codes for three and four transmit antennas can be given as [48]

$$\mathbf{C}_3 = \begin{pmatrix} s_1 & -s_2^* & -s_3^* & 0 \\ s_2 & s_1^* & 0 & -s_3^* \\ s_3 & 0 & s_1^* & s_2^* \end{pmatrix} , \tag{1.40}$$

and

$$\mathbf{C}_4 = \begin{pmatrix} s_1 & -s_2^* & -s_3^* & 0 \\ s_2 & s_1^* & 0 & -s_3^* \\ s_3 & 0 & s_1^* & s_2^* \\ 0 & s_3 & -s_2 & s_1 \end{pmatrix} , \tag{1.41}$$

respectively. The received signal vectors $\mathbf{y}_{n_D}$, $n_D = 1, \cdots, N_D$, can be expressed as

$$\mathbf{y}_{n_D} = \sqrt{\tfrac{E_b}{N_T}}\mathbf{H}\mathbf{c}_{n_D} + \mathbf{z}_{n_D} \ , \quad n_D = 1, \ \cdots, \ N_D \ , \tag{1.42}$$

where $\mathbf{H} \in \mathbb{C}^{N_R \times N_T}$ is a MIMO channel matrix with complex-valued Gaussian distributed random entries. $\mathbf{c}_{n_D} \in \mathbb{C}^{N_T \times 1}$ is the n_D^{th} column vector of the transmit ST code matrix, $\mathbf{C}$. E_b is the transmitted energy per symbol. $\mathbf{z}_{n_D} \in \mathbb{C}^{N_R \times 1}$ is a noise vector of complex-valued MCA observations for different receive antennas. To specify the MCA model over the time dimension, we assume that the noise vectors $\mathbf{z}_{n_D}$, for different time slots, are statistically independent. It follows that the joint distribution of the received noise vectors, $\mathbf{z}_{n_D}$, $n_D = 1, \cdots, N_D$, can be given as

$$\begin{aligned} p(\mathbf{z}_1, \cdots, \mathbf{z}_{N_D}) &= \prod_{n_D=1}^{N_D} p_{\mathbf{z}}(\mathbf{z}_{n_D}) \ , \\ &= \prod_{n_D=1}^{N_D} \sum_{m_{n_D}=0}^{\infty} \frac{\alpha_{m_{n_D}}}{(2\pi)^{N_R}|\mathbf{\Sigma}_{m_{n_D}}|} \mathrm{e}^{-\frac{1}{2}\mathbf{z}_{n_D}^H \mathbf{\Sigma}_{m_{n_D}}{}^{-1}\mathbf{z}_{n_D}} \ . \end{aligned} \tag{1.43}$$

The optimum decoder of the orthogonal ST block codes in the presence of MCA noise is considered in [18, 40]. For a multivariate MCA model given in (1.35), the optimum decoding metric can be given as [18]

$$\hat{\mathbf{C}}_{\text{ML}} = \arg\max_{\mathbf{C}} \prod_{n_D=1}^{N_D} p_{\mathbf{z}}\left(\mathbf{y}_{n_D} - \sqrt{\tfrac{E_b}{N_T}}\mathbf{H}\mathbf{c}_{n_D}\right) \ . \tag{1.44}$$

From (1.44), we observe that the optimum decoder performs an exhaustive searching process to compute the metrics for all possible transmit ST coded matrices. The performance evaluation of MIMO systems in uncorrelated MCA noise shows a loss in the performances of the optimum ST decoding in impulse noise over those in AWGN [18]. However, it is not clear how the ST coding behaves in the case of correlated MCA noise. Hence, there is a need to investigate the performance evaluation of the optimum ST decoding that utilizes noise correlations to improve the performance.

1.3.3 OFDM Signals

OFDM is essentially a discrete form of multicarrier modulation, which transmits serial data streams on a set of parallel subcarriers. Under ideal channel conditions, the parallel subcarriers are orthogonal. The number of subcarriers is chosen such that the bandwidth

of each subcarrier is much less than the coherence bandwidth of the fading channel. Thus, each subcarrier undergoes flat fading. Figure 1.7 illustrates a discrete-time model of a

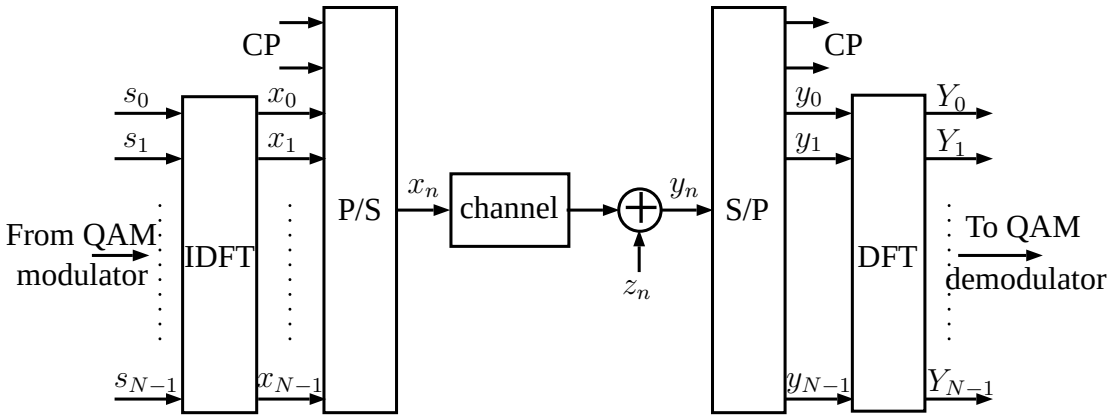

Figure 1.7: A discrete-time model of a conventional OFDM system

conventional OFDM system with N subcarriers. In this figure, the incoming information bits are mapped into N complex symbols, s_k, $k = 0, \cdots, N-1$, according to the used modulation scheme, such as PSK or QAM. The discrete-time samples of the OFDM signal is generated using the inverse discrete-Fourier transform (IDFT) as follows:

$$x_n = \frac{1}{\sqrt{N}} \sum_{k=0}^{N-1} s_k \mathrm{e}^{-j\frac{2\pi}{N}kn} , \quad n = 0, \cdots, N-1 . \tag{1.45}$$

The OFDM symbol $\mathbf{x} = [x_0, \cdots, x_{N-1}]^T$ can be expressed in matrix notation as follows

$$\mathbf{x} = \mathbf{W}_N^H \mathbf{s} , \tag{1.46}$$

where $\mathbf{W}_N^H$ is the IDFT matrix. We consider that the OFDM symbol, $\mathbf{x}$, passes through a multipath fading channel. The discrete-time model of the multipath channel can be given as [45]

$$h(n;\nu) = \sum_{l=0}^{L-1} h_l[n]\delta(n-\nu_l) , \tag{1.47}$$

where L is the number of paths and $h_l[n]$ is the channel gain of the l^{th} path. The path gains, $h_l[n]$, $\forall l$, are characterized as a complex-valued Gaussian random variable with time index n and statistically independent for any l. ν_l is the channel delay (in sample) associated with the l^{th} path. Without loss of generality, we assume that $0 \leq \nu_0 \leq \nu_1 \leq \cdots \leq \nu_{L-1} < N$. To suppress intersymbol interference, the cyclic prefix (CP) is perpended to the OFDM symbol by copying the last μ_{cp} samples to the beginning of the current OFDM symbol. Then, x_n, $n = N-\mu_{cp}, \cdots, N-1, 0, \cdots, N-1$, represents the

transmitted OFDM sequence. For slowly fading channels, one can further assume that the path gains remain constant during the duration of the OFDM symbol, i.e., $h_l[n] \approx h_l$. The received OFDM sequence can be given as

$$y_n = \sqrt{E_b}\sum_{l=0}^{L-1} h_l x_{n-\nu_l} + z_n \ , \quad n = -\mu_{cp}, \cdots, -1, 0, \cdots, N-1 \ . \tag{1.48}$$

where z_n denotes the additive complex noise sequence. The received sequences $y_{-\mu_{cp}}, \cdots, y_{-1}$ are affected by ISI, so we discard them. In matrix notation, given that $\nu_{L-1} \leq \mu_{cp}$, the received OFDM symbol after the CP removal is given by

$$\mathbf{y} = \sqrt{E_b}\bar{\mathbf{H}}\mathbf{x} + \mathbf{z} \ , \tag{1.49}$$

where $\bar{\mathbf{H}} \in \mathbb{C}^{N\times N}$ is a circulant convolution channel matrix of i.i.d. complex Gaussian entries. $\bar{\mathbf{H}}$ is fully specified by one vector $\mathbf{h} = [h_0, \cdots, h_{L-1}, \mathbf{0}_{1\times N-\nu_{L-1}}]^T$, which is the first column of $\bar{\mathbf{H}}$. The remaining columns of are cyclic permutations of $\mathbf{h}$ with offset equal to the column index. The conventional OFDM system applies a discrete-Fourier transform (DFT) operation to compute the following decision variables

$$\begin{aligned} \mathbf{Y} &= \sqrt{E_b}\mathbf{W}_N\bar{\mathbf{H}}\mathbf{x} + \mathbf{W}_N\mathbf{z} \ , \\ &= \sqrt{E_b}\mathrm{diag}(\mathbf{\Lambda})\mathbf{s} + \mathbf{Z} \ , \end{aligned} \tag{1.50}$$

where $\mathbf{W}_N$ is the DFT matrix and the elements of $\mathbf{\Lambda}$ are the eigenvalues of $\bar{\mathbf{H}}$. The DFT pairs convert the frequency-selective fading into a set of parallel flat-fading channels. Since $\mathbf{W}_N$ is unitary, when $\mathbf{z}$ is Gaussian, it follows that $\mathbf{W}_N\mathbf{z}$ is still Gaussian with unchanged average noise power. The DFT receiver is the optimum in the case of Gaussian noise. In impulse noise, due to the spreading effect of the DFT matrix, the conventional DFT operation averages the effects of impulse noise over all used subcarriers. This justifies why the conventional OFDM system is more robust to impulse noise than single carrier systems. There are two main approaches to mitigate the effects of impulse noise for OFDM systems. Those approaches are classified as a time-domain approach and a frequency-domain approach. The time-domain approach cancels the effects of impulses before the DFT operation such as a clipping and a blanking nonlinearity [37,39,41]. In the frequency-domain approach, a set of unused subcarriers can be used to estimate the presence of impulse noise in the received OFDM symbol [49]. Sparse Bayesian learning (SBL) [43,44] is one of the most effective approaches to mitigate the effects of impulse noise using a set of null-subcarriers. This method assumes that the received noise vector has two components: a Gaussian component $\mathbf{z}_G$ and impulsive component $\mathbf{z}_I$. Since the impulsive component

$\mathbf{z}_I$ is sparse in time, the SBL approach provides an efficient estimate of $\mathbf{z}_I$ by allocating a set of null subcarriers. Subtracting the reconstructed interference, $\hat{\mathbf{z}}_I$, from the OFDM symbol achieves up to 5 dB gain in an SNR [49]. Adapting the SBL algorithm to jointly estimate the transmitted sequence along with the sparse impulse noise vector from all subcarriers provides up to 10 dB gain over a conventional OFDM receiver [49].

1.4 Outline of the Thesis

In this thesis, we introduce modern detection schemes of digital signals in the presence of MCA noise. We treat the effects of impulse noise utilizing temporal, spatial, and spectral information at the receiver. The rest of the thesis is divided into five chapters as follows:

Chapter 2 considers an empirical verification of the MCA model for 2.4 GHz wireless interference. We begin with the statistical properties of a white MCA noise process. We also present the band-limitation effects of filtering on the temporal correlation of noise samples. For spatial dimensions, we introduce a correlated multivariate MCA model as an analytical model for spatially coupled impulse noise. Using our own measurement setup, we verify the multivariate MCA model for wireless interference in the 2.4 GHz band. The measurement setup can handle up to four interfering signals using 4-receive antennas.

In **Chapter 3**, we consider the classical detection problem of binary signals in MCA noise. We introduce an approximate representation of the MCA model, where we further simplify the two-term model to a single term. Such an approximation leads to a closed-form representation of the optimum nonlinearity. In addition, we introduce a decision boundary analysis to justify the performance of the optimum detector in different MCA noise environments. Additionally, we use the approximate nonlinearity to justify and analyze the behavior of suboptimum detectors such as an LOD, and a clipping detector. For further simplification, we propose a piecewise linear approximation of the optimum nonlinearity, which reduces the complexity of the optimum detector.

Chapter 4 deals with the optimum schemes for mitigating the effects of fading and impulse noise. We derive an asymptotic upper performance bound of the optimum combining schemes for time and space diversity. We analyze and justify the performance of each scheme in different conditions of impulse noise. We further show how the approximate MCA model can be used to simplify the optimum combining schemes in closed form. For ST coding, we derive an upper bound of the pairwise error probability (PEP) of the

optimum ST decoding in the presence of spatially correlated MCA noise. In addition, we introduce an approximate metric of the optimum ST decoding in MCA noise similar to a minimum distance (MD) metric of the optimum decoding in Gaussian noise.

Chapter 5 considers the detection problems of OFDM signals over fading channels with MCA noise. First, we discuss the different detection schemes of OFDM signals in MCA noise, such as the optimum OFDM receiver, a zero-forcing (ZF) detector, and nonlinear detectors. We show that the blanking nonlinearities are related to the minimum mean-square error (MMSE) detector for mitigating the effects of MCA noise. Second, we derive an upper performance bound of the optimum OFDM detector in MCA noise. Since the optimum receiver requires perfect knowledge of noise states, we adopt the SBL approach to estimate the state of MCA noise using nulling subcarries. Finally, we introduce a first step towards the realization of the optimum OFDM detector in impulse noise.

In **Chapter 6**, we conclude this thesis and provide future research directions.

Chapter 2

Impulse Noise Measurements

The 2.4 GHz industrial, scientific, and medical (ISM) band is originally reserved for the use of radio frequency emissions of ISM equipments such as microwave ovens, medical equipment, car ignition, and hairdryers. Since this band is licensed-free, it is already shared by communication systems such as Bluetooth, cordless phones, and a wireless local area network (LAN). Thus, the coexistence of ISM appliances can severely interfere with the operations of communication systems at the 2.4 GHz band. Interference measurements at the 2.4 GHz ISM-band show that the interference exhibits the impulsive nature of the MCA distribution [6]. As we showed in Chapter 1, the MCA model describes only the amplitude distributions, which already come with question marks, almost no correlation (spectral) properties, neither in time nor space, except for rudimentary 2-antenna systems in [46]. In addition, the algebraic extension of the MCA model for multiple-antenna systems is not well explained and verified.

In this chapter, we employ impulse noise measurements to verify the MCA model for multiple-antenna systems. First, we investigate the statistical properties of the MCA noise process. Then, we introduce a correlated multivariate MCA model as an algebraic extension of the MCA model for an arbitrary number of receive antennas. To validate this extension, we used a measurement setup with 4-receive antennas to measure 4 interference processes in parallel.

2.1 Statistical Properties of MCA Interference

The analytical model of MCA interference [1] provides the amplitude distributions of the received passband noise at the output of the intermediate frequency (IF) stage of the

receiver. The passband MCA noise, $w(t)$, can be expressed as

$$w(t) = \mathrm{Re}\{z(t)\mathrm{e}^{j2\pi f_c t}\} \,, \tag{2.1}$$

where $z(t) = z_{\mathrm{I}}(t) + jz_{\mathrm{Q}}(t)$ is the equivalent lowpass noise process and f_c is the carrier frequency. In fact, Middleton assumed that the bandpass filter (BPF) of the receiver stages has a negligible effect on the amplitude distribution of the received interference. This implies that the impulse response of the bandpass filter is extremely short compared to the duration of the impulse noise. Thus, Class-A noise is regarded as the interference process whose spectrum is equal to or less than the receiver bandwidth. The MCA density of the passband noise samples of $w(t)$ is given as

$$p_w(w) = \sum_{m=0}^{\infty} \frac{\alpha_m}{\sqrt{2\pi\sigma_m^2}} \mathrm{e}^{-w^2/2\sigma_m^2} \,, \tag{2.2}$$

where

$$\alpha_m = \frac{A^m \mathrm{e}^{-A}}{m!} \,, \tag{2.3}$$

and

$$\sigma_m^2 = \sigma^2 \frac{m/A + \Upsilon}{1+\Upsilon} \,. \tag{2.4}$$

The parameters A and Υ were designated as the impulsive index and the Gaussian factor of the MCA model, respectively. The above model assumes that the received passband interference, $w(t)$, consists of two independent noise components: Gaussian background noise $w_G(t)$ and impulsive noise $w_I(t)$. The variances of these components are related to Υ as

$$\sigma_G^2 = \sigma^2 \frac{\Upsilon}{1+\Upsilon} \,, \tag{2.5}$$

and

$$\sigma_I^2 = \sigma^2 \frac{1}{1+\Upsilon} \,, \tag{2.6}$$

where $\sigma^2 = \mathrm{E}\{w^2\}$ is the average power of the passband noise process. From the above equations, it is clear that the ratio σ_G^2/σ_I^2 defines the Gaussian factor Υ. The average power of the MCA noise process, σ^2, is related to σ_G^2 and σ_I^2 as follows:

$$\begin{aligned} \sigma^2 &= \sigma_G^2 + \sigma_I^2 \,, \\ &= \sigma_G^2 + \frac{\sigma_G^2}{\Upsilon} \,. \end{aligned} \tag{2.7}$$

From (2.4)-(2.6), we relate σ_m^2 to σ_G^2 as

$$\begin{aligned}\sigma_m^2 &= \sigma_G^2 + \frac{m}{A}\sigma_I^2 \,, \\ &= \sigma_G^2\left(1 + \frac{m}{A\Upsilon}\right) \,. \end{aligned} \tag{2.8}$$

The above equation implies that $\sigma_0^2 = \sigma_G^2 < \sigma_1^2 < \cdots < \sigma_\infty^2$. The first term of (2.2) represents the scaled distribution of the Gaussian noise, w_G. The remaining terms, $m = 1, \cdots, \infty$, are thought to model the presence of impulse noise w_I. Accordingly, the parameter m can be designated as the noise state of $w(t)$, i.e., $m = 0$ refers to a Gaussian state and $m = 1, 2, \cdots, \infty$ refer to impulsive states[1]. Therefore, the impulsive component, w_I, is comprised of a single event summarizing all possible impulsive states, where the probability of being in each state is given by α_m. Numerically, the impulsive index, A, can take on any real positive values. However, Middleton defined A over a specific range, $A \in [10^{-6}, 1]$, as follows

$$A = \frac{A_I}{T}\bar{T}_I \,, \tag{2.9}$$

where A_I denotes the average number of impulsive emissions in the observation period T. $\bar{T}_I$ denotes the mean duration of the impulsive emissions. The definition of A may not hold true for $A > 1$. To enhance the understanding, we provide some details of the MCA density for different values of A.

For $A < 1$, the probability α_m tends to zero rather rapidly as m increases. Therefore, the first two terms of (2.2) are sufficient to approximate the MCA density. The samples of MCA noise $w(t)$ can be seen as the emissions of either a Gaussian state, $m = 0$, or an impulsive state, $m = 1$. Since $T = N\bar{T}_I$, the impulsive index, $A = \frac{A_I}{N}$, expresses the probability of being in the impulsive state. This explains why the value of A is upper bounded by 1. Figure 2.1 depicts a pictorial view of noise observations for $A = 0.1$ and $N = 10$. Since $\sigma_1^2/\sigma_0^2 = 1 + \frac{1}{A\Upsilon}$, the term $A\Upsilon$ controls the variance of the impulse

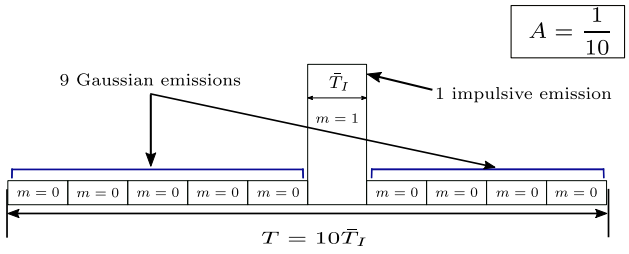

Figure 2.1: A pictorial view of MCA noise observations for $A = 0.1$ and $N = 10$

[1]Impulsive states represent the presence of impulse noise with Gaussian noise.

noise (the impulsiveness of noise). For $A > 1$, the probability α_m does not as rapidly decrease with m. Hence, the first two term will not be sufficient to approximate the MCA density. Since α_m follows a Poisson distribution of the noise state m, A can be seen as the expectation of m in the observation time $T = N\bar{T}_I$. Thus, we have

$$A = \frac{\sum_{k=1}^{N} m_k}{N} \ , \tag{2.10}$$

where m_k represents the noise state of the k^{th} observation. The parameter A_I, for $A > 1$, can be seen as the sum of noise states for the impulsive samples rather than the average number of impulsive emissions. Figure 2.2 depicts a pictorial view of the noise states for $A = 1.6$ and $N = 10$. In Fig. 2.2, we show that 5 noise states are required to model

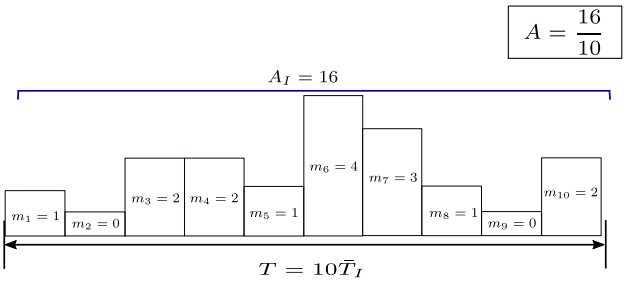

Figure 2.2: A pictorial view of MCA noise observations for $A = 1.6$ and $N = 10$

the MCA noise for $A = 1.6$. Moreover, we note that the events are not dominated by a single noise state, and hence, the statistics of the MCA samples approach a Gaussian distribution with variance $\sum_{m=0}^{\infty} \alpha_m \sigma_m^2 = \sigma^2$.

To investigate the tail behavior of the MCA distribution with respect to A, we evaluate the complementary cumulative distribution function (CCDF) of the received noise amplitude, $|w|$, as follows:

$$\begin{aligned} P(|w| > \gamma) &= 2\int_{\gamma}^{\infty} p_w(w)dw \ , \\ &= \sum_{m=0}^{\infty} \alpha_m \text{erfc}\left(\frac{\gamma}{\sqrt{2}\sigma_m}\right) \ . \end{aligned} \tag{2.11}$$

In Fig. 2.3, we illustrate the CCDF curves of the MCA density for different A. We observe that the CCDF has a plateau shape [21]. For $A < 1$ and $A\Upsilon < 1$, the width and the height of the plateau curve are dominated by $\sigma_1^2/\sigma_G^2 \approx 1/A\Upsilon$ and A, respectively. This suggests a 2-term approximation of the MCA model in the form of

$$p_w(w) \approx \frac{1-A}{\sqrt{2\pi\sigma_0^2}} \text{e}^{-w^2/2\sigma_0^2} + \frac{A}{\sqrt{2\pi\sigma_1^2}} \text{e}^{-w^2/2\sigma_1^2} \ , \tag{2.12}$$

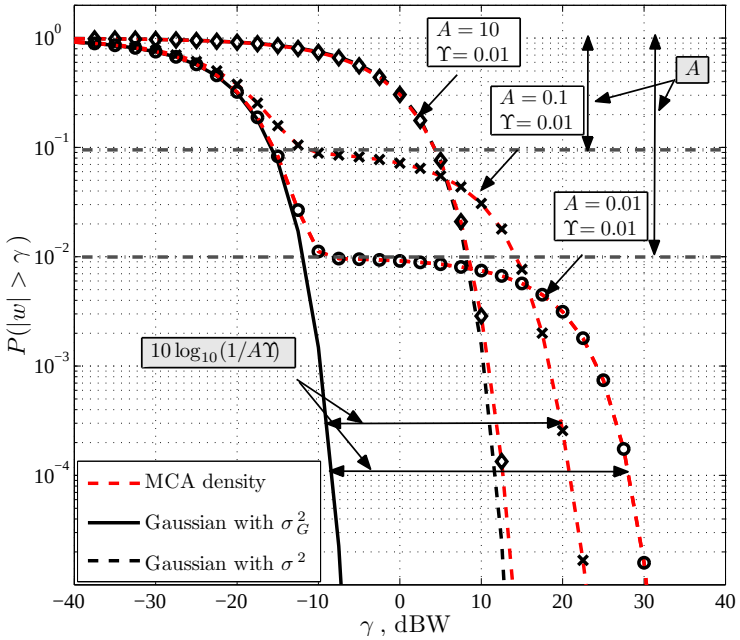

Figure 2.3: CCDF of MCA noise with different values of A. Note that the noise variance, σ^2, is unity

where the second term of (2.12) is sufficient to approximate the impulsive terms of the MCA model. In addition, we note that when $A > 1$, the CCDF of the MCA model approaches a Gaussian distribution with variance σ^2.

To investigate the distribution of the equivalent lowpass noise $z(t)$, the passband MCA noise $w(t)$ can be expressed in terms of quadrature components $z_{\mathrm{I}}(t)$ and $z_{\mathrm{Q}}(t)$ as follows:

$$\begin{aligned} w(t) &= \mathrm{Re}\{(z_{\mathrm{I}}(t) + jz_{\mathrm{Q}}(t))\mathrm{e}^{j2\pi f_c t}\} \ , \\ &= z_{\mathrm{I}}(t)\cos(2\pi f_c t) - z_{\mathrm{Q}}(t)\sin(2\pi f_c t) \ . \end{aligned} \tag{2.13}$$

Since the MCA model assumes that the spectrum of the receiver filter, B_T, is greater than the spectrum of impulse noise, the quadrature components of $w(t)$ can be seen as lowpass MCA noise processes. This justifies the complex extension of the MCA distribution [18], which represents the joint density of baseband noise, $z(t) = z_{\mathrm{I}}(t) + jz_{\mathrm{Q}}(t)$, as

$$p_z(z) = \sum_{m=0}^{\infty} \frac{\alpha_m}{2\pi\sigma_m^2} \mathrm{e}^{-|z|^2/2\sigma_m^2} \ , \tag{2.14}$$

where $|z|^2 = z_{\mathrm{I}}^2 + z_{\mathrm{Q}}^2$.

2.1.1 Temporal Dependence and Correlation

We assume that the MCA noise process $w(t)$ is sampled uniformly at times kT_s, $k = 1, 2, \cdots, N$, where T_s is the sample spacing. Since the MCA model ignores the time dependence between samples of $w(t)$, the MCA noise sample at the k^{th} sampling instant can be represented as

$$w(kT_s) = w_{m_k}\delta(t - kT_s) \ , \tag{2.15}$$

where $\delta(t)$ is a Dirac delta function and m_k denotes the state of noise observations (Gaussian for $m_k = 0$ or impulsive for $m_k \geq 1$) at the k^{th} sampling instant. The MCA noise samples, w_{m_k}, $\forall k$, are Gaussian random variables with zero mean and variances $\sigma^2_{m_k}$. To investigate the effects of the BPF on the statistical properties of $w(kT_s)$, we assume an ideal BPF with a spectrally flat response to all frequencies in the range $|f - f_c| \leq \frac{1}{2}B_T$. The normalized impulse response of the ideal BPF can be given as

$$h_{BPF}(t) = \frac{1}{B_T}\frac{\sin(\pi B_T t)}{\pi t} \ , \tag{2.16}$$

Figure 2.4 shows a typical impulse response of the ideal BPF filter. At the input of the

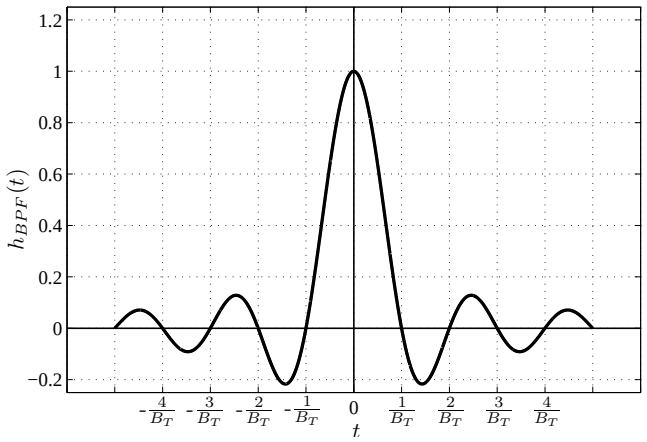

Figure 2.4: The impulse response of an ideal BPF

filter, the MCA noise samples, $w(kT_s)$, $\forall k$, can be seen as a series of ideal mathematical impulses whose weights are Gaussian random variables of variances $\sigma^2_{m_k}$. Thus, each impulse at the output of the filter is shaped and stretched in time according to $h_{BPF}(t)$. Therefore, the temporal correlation of impulse noise is determined by the impulse response of the filter. Similar to bandpass white Gaussian noise [45], sampling the filtered noise with a sampling rate B_T can guarantee independent noise observations in time dimension. This means that the receiver can be supplied with up to N independent noise observations within a signaling interval, $T_b = N/B_T$. This approach justifies the assumption of inde-

pendent noise observations considered in the classical detection problem of narrowband signals corrupted by MCA noise in [15].

2.1.2 Spatial Dependence and Correlation

The statistical-physical modeling [46] showed that the impulse noise, $w_{n_R}(t)$, at two receive antennas, is correlated and may have unequal Gaussian factors, $\Upsilon_{n_R} = \sigma_G^2/\sigma_{I,n_R}^2$. Since this modeling was limited to two-antenna systems, we adopt the algebraic extension for an arbitrary number of receive antennas. Similar to [46], we assume that the received interference at the $n_R{}^{\text{th}}$ receive antenna consists of two components as follows:

$$w_{n_R}(t) = w_{G,n_R}(t) + w_{I,n_R}(t) \; . \tag{2.17}$$

We also assume that $\mathrm{E}\{|w_{G,n_R}|^2\} = \sigma_G^2$ and $\sigma_{I,n_R}^2 = \sigma_G^2/\Upsilon_{n_R}$, $\forall n_R = 1, \cdots, N_R$. Thus, the average variance of passband MCA noise, $\sigma_{n_R}^2$, for the $n_R{}^{\text{th}}$ channel can be expressed as

$$\sigma_{n_R}^2 = \sigma_G^2 + \frac{\sigma_G^2}{\Upsilon_{n_R}} \quad \forall n_R = 1, \cdots, N_R \; . \tag{2.18}$$

This means that $\sigma_{n_R}^2$, $\forall n_R = 1, \cdots, N_R$, are not necessarily identical. Similar to (2.8), σ_{m,n_R}^2, $\forall n_R$, can be given as

$$\sigma_{m,n_R}^2 = \sigma_G^2 \left(1 + \frac{m}{A\Upsilon_{n_R}}\right) \quad \forall n_R = 1, \cdots, N_R \; . \tag{2.19}$$

When the received noise observations are spatially dependent and correlated, the algebraic extension of (2.2) leads to a correlated multivariate MCA model as

$$p_{\mathbf{w}}(\mathbf{w}) = \sum_{m=0}^{\infty} \frac{\alpha_m}{(2\pi)^{N_R}|\mathbf{\Sigma}_m|} \mathrm{e}^{-\frac{1}{2}\mathbf{w}^T\mathbf{\Sigma}_m^{-1}\mathbf{w}} \; , \tag{2.20}$$

where $\mathbf{w} = [w_1, \cdots, w_{N_R}]^T$ is the received noise vector at the N_R receive antennas. $\mathbf{\Sigma}_m$ is the noise covariance matrix, which is given by

$$\mathbf{\Sigma}_m = \begin{pmatrix} \sigma_{m,1}^2 & \cdots & \rho_{m,1N_R}\sigma_{m,1}\sigma_{m,N_R} \\ \vdots & \ddots & \vdots \\ \rho_{m,N_R1}\sigma_{m,N_R}\sigma_{m,1} & \cdots & \sigma_{m,N_R}^2 \end{pmatrix} \; , \tag{2.21}$$

where $\rho_{m,n_R\grave{n}_R}$ denotes the correlation coefficient of noise observations at the n_R^{th} and $\grave{n}_R^{\text{th}}$ receive antennas for the m^{th} term of (2.20). We may further assume that the impulsive

components, $m \geq 1$, possess identical correlation coefficients, $\rho_{m,n_R\grave{n}_R} = \rho_{I_{n_R\grave{n}_R}}$, $\forall m = 1, 2 \cdots, \infty$, that differs from those of Gaussian components, $\rho_{0,n_R\grave{n}_R} = \rho_{G_{n_R\grave{n}_R}}$. In the following, we describe a measurement campaign that be conducted to verify the algebraic extension of the MCA model for wireless interference at 2.4 GHz.

2.2 Measurement Campaign and Setup

In this section, we describe a measurement receiver for impulse noise in the 2.4 GHz band. The measuring receiver employs 4-antenna elements to collect impulse noise form different receive antennas.

2.2.1 Measurement Receiver

The measurement setup consists of an RF receiver, a digital oscilloscope, a network analyzer, and a laptop. Figure 2.5 illustrates the RF receiver for measuring impulse noise. The receiver consists of 4-antenna elements, a bank of bandpass filters (centered at $f_c = 2.435$ GHz), and downconversion mixers. The antenna array is mounted on a conducting steel sheet with adjustable antenna spacing[2]. The antenna elements are quarter-wave monopole antennas designed for the center frequency of the bandpass filters. The bandpass filters pass the signals within a wireless LAN range, i.e., the range of 2.340-2.530 GHz. The 6 dB RF bandwidth of the BPF is 190 MHz, which determines the bandwidth of the noise measurement, B_T. The signals from the filters are mixed down

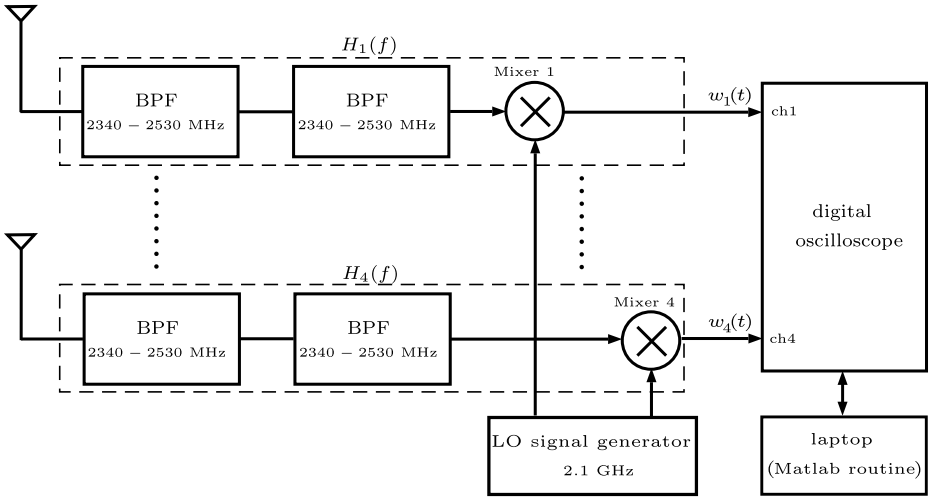

Figure 2.5: Impulse noise measurement setup

[2]The distance between the adjacent elements is approximately equal to $\lambda/4$.

with a carrier from a local oscillator (LO). The frequency of the LO signal is selected such that the intermediate frequencies, f_{IF}, of the output signals are within the frequency range of the oscilloscope, i.e., we chose the LO carrier to be $f_{LO} = 2.1$ GHz for a digital oscilloscope with a 400 MHz bandwidth. We use a Matlab program to acquire and transfer the measurement data from the oscilloscope to a controlling laptop. The measurements are originally sampled by the oscilloscope with a sampling rate of 5 GHz. However, the stored data are further downsampled (by a factor of 4) to decrease the size of measured data. Thus, the sampling interval is given by $T_s = 0.8\,ns$. The measured waveforms are stored in segments of duration $0.2\,\mu$s (250 samples per the segment[3]). The program only stores segments with impulse noise since the oscilloscope is triggered to capture the impulsive events. In each acquisition, we acquire a block of 1000 segments and the triggering time of each segment. Figure 2.6 depicts measured impulse noise. We note that each segment

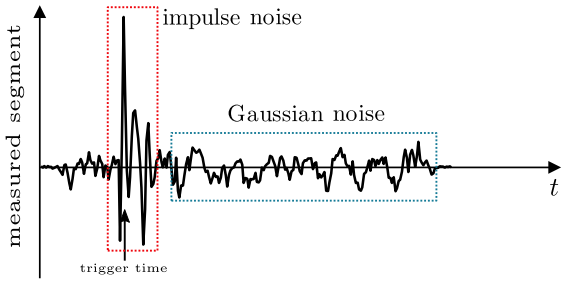

Figure 2.6: A typical measured segment with impulse noise

contains two noise components (Gaussian and impulsive). Those components are used to compute the statistical distributions of the measured impulse noise. The measurements are repeated to collect sufficient data (we collected 100 blocks for each measurement) to analyze the statistical characteristics of impulse noise.

2.2.2 Measurement Results

We measured impulse noise from several sources. In preliminary measurements, we looked into the noise of ISM sources such as car ignition and an electrical drill. The last one only leads to visible impulse noise in the near field. For more elaborate results, we took additional measurements in different factories, which verifies the presence of impulsive interference in industrial environments. In Fig. 2.7, we show a snapshot of measured noise segments form the 4 receive antennas caused by car ignition. Figures 2.8 and 2.9 illustrate two snapshots of impulse noise segments measured in two factories caused by a shoe manufacturing machine and an assembly machine for automotive components,

[3]Parameters can be modified and had to be adjusted depending on the local impulse noise conditions.

receptively. Figures 2.7, 2.8, and 2.9 indicate two interesting features of impulse noise at the 2.4 GHz band. First, we observe that the impulsive segments (time samples) consist of very short impulses which are similar to the pulse train of the MCA process [1]. Second, we note that impulsive events at different antennas (space observations) appeared jointly, which is consistent with the spatial dependency of the multivariate MCA model.

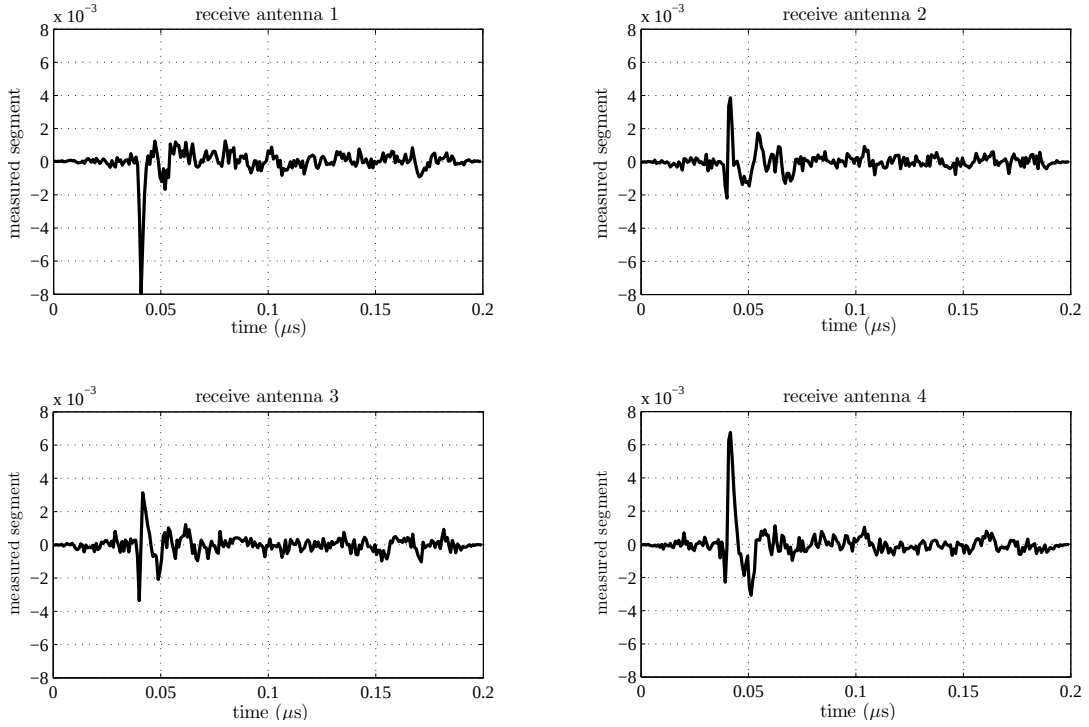

Figure 2.7: Impulse noise segments at the receive antenna array (with $\lambda/4$ antenna spacing) caused by car ignition

2.3 Model Verification

In this section, we use the measured impulse noise to validate the temporal and space properties of the MCA model. First, we involve the measured impulse noise of the IF-stage to analyze the statistical characteristics of the passband MCA process. Then, we further use the equivalent quadrature components of the measured data to investigate the distributions of the baseband MCA process. Finally, we verify the multivariate MCA distribution for modeling the measured interference from different receive antennas.

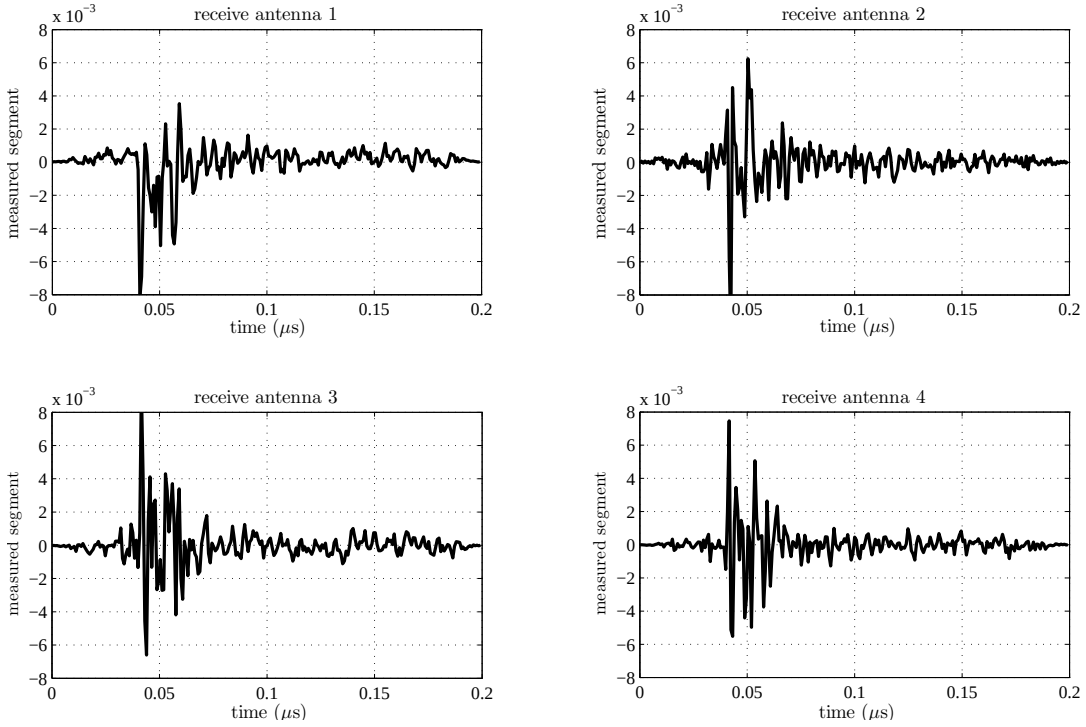

Figure 2.8: Impulse noise at the receive antenna array (with $\lambda/4$ antenna spacing) caused by a shoe making machine

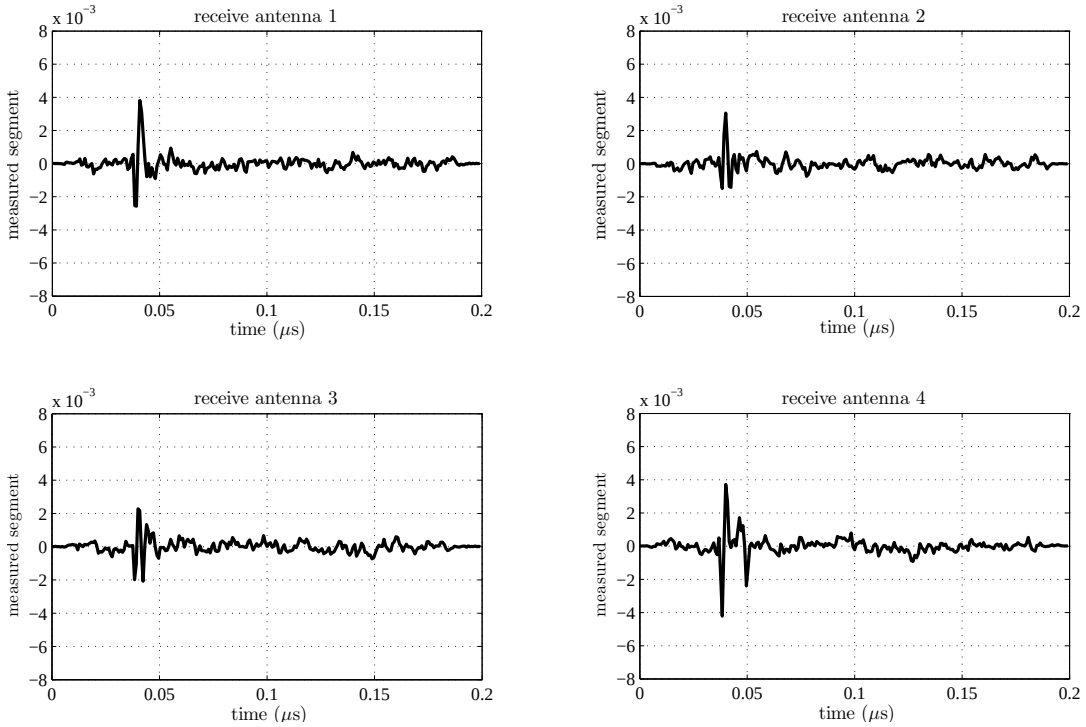

Figure 2.9: Impulse noise at an antenna array (with $\lambda/4$ antenna spacing) caused by assembly machines of an automotive supplier

2.3.1 MCA Model for Measured Interference

The IF stage of the measurement receiver downconverts the measured spectrum in the range 2.340-2.530 GHz to frequencies between 240 MHz and 430 MHz. We start the analysis with the temporal characteristics of the measured interference at the IF stage. Since impulse noise at the different receive antennas has the same temporal properties, we limit the analysis to the measured interference of the first receive antenna. We compute the autocorrelation function of the measured data as

$$\phi_{n_R}(\tau) = \mathrm{E}\{w_{n_R}(t) w_{n_R}(t+\tau)\} \; . \tag{2.22}$$

We take the waveforms of each passband measured segment, $w_{n_R}(t)$, and correlate it with $w_{n_R}(t+\tau)$. We then average over the results of all measured segments. In Fig. 2.10, we depict the autocorrelation functions of the impulse noise caused by car ignition, automotive manufacturing, and the shoe production machine. We observe that the

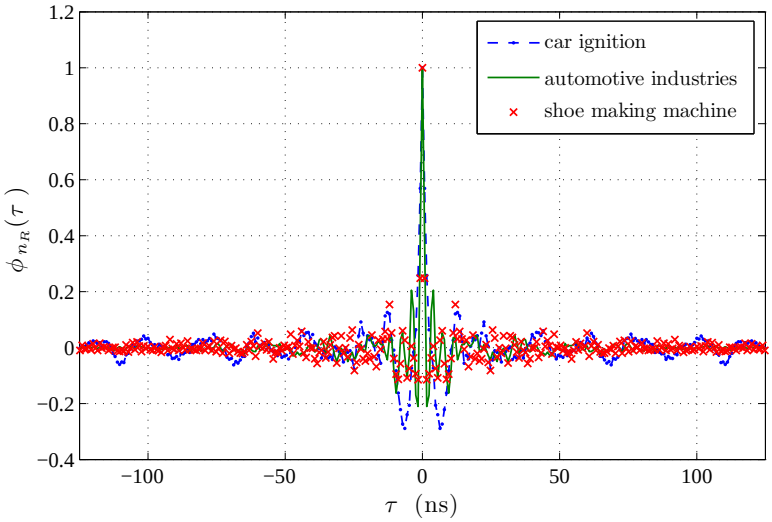

Figure 2.10: Autocorrelation functions

autocorrelation function of measurements at the IF-stage has a Sinc-shaped function, which agrees with the impulse response of the analog BPF of the IF-stage. However, since the filter has a bandwidth of 190 MHz, we note that the noise samples are partially correlated (a few samples around $\tau = 0$).

In the statistical analysis, we are interested to model the effects of interference on a wireless LAN spectrum. Thus, the measured segments are further filtered using a BPF to select the noise components inside the wireless LAN range at the IF-stage. Furthermore, to eliminate the amplitude attenuation and phase shifts due to the mixers, cabling, etc., for the four channels, the frequency components of the measured segments are calibrated according

to the measured frequency response, $H_{n_R}(f)$[4]. Figure 2.11 depicts the calibration and the baseband processing of the measurements. After passband filtering and calibration,

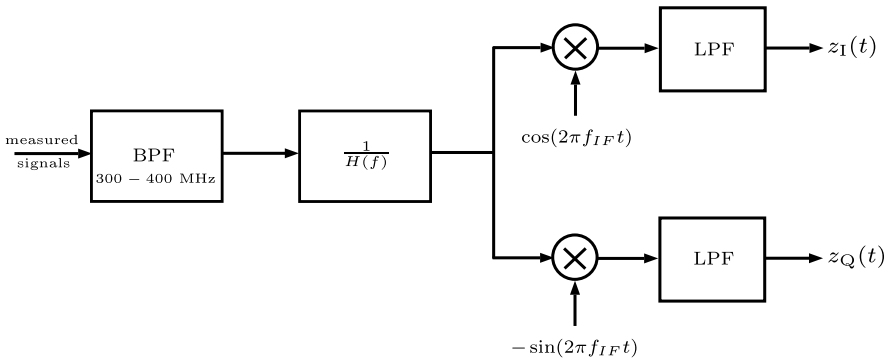

Figure 2.11: Measurements processing from passband to baseband

we computed the voltage histograms of the measurement data. We used the impulsive component of measured segments (recall Fig. 2.6) to compute the tails distribution of the voltage histogram. Since we measured only the segments of impulse noise, we further scaled down the tail distribution according to a rate of impulsive segments. We used the triggering time of measured segments to compute the rate of segments that are affected by impulses. The rate of impulsive segments caused by car ignition, the shoe machine, and the automotive supplier were obtained as 16.6 segments/s, 3.78 segments/s, and 2.1 segments/s, respectively. Figure 2.12 depicts the voltage histograms of measured impulse noise caused by car ignition, automotive manufacturing, and the shoe production machine. To confirm the MCA density for modeling the passband measurements, we computed the CCDF from the voltage histogram. We used a curve fitting approach to approximate the CCDF of the measured data with the MCA model. Figure 2.3 illustrates the CCDF curves of the measured interference along with those of the MCA model. This figure indicates several interesting points regarding the ISM interference in wireless LAN channels. First, we note that the terms $A\Upsilon$ for all measurements are less than unity, which reflects the impulsive nature of ISM interference in the 2.4 GHz band. Second, we observe that the impulsive indexes, A, for all measurements are less than the specified values, $A \in [1,\ 10^{-6}]$, of the MCA model. This complies with the experienced number of impulsive segments per second for each campaign, which reveals a small probability for impulsive components of the ISM sources in wireless channels. Third, we note that the first few terms of the MCA model are sufficient to approximate the measured densities. Thus, for car ignition and automotive industries, we only need two terms to approximate the plateau shapes of the measured CCDF. However, we note that the plateau shape

[4]In an additional setup, we used a vector network analyzer to measure the transfer functions, $H_{n_R}(f)$, $n_R = 1, \cdots, 4$.

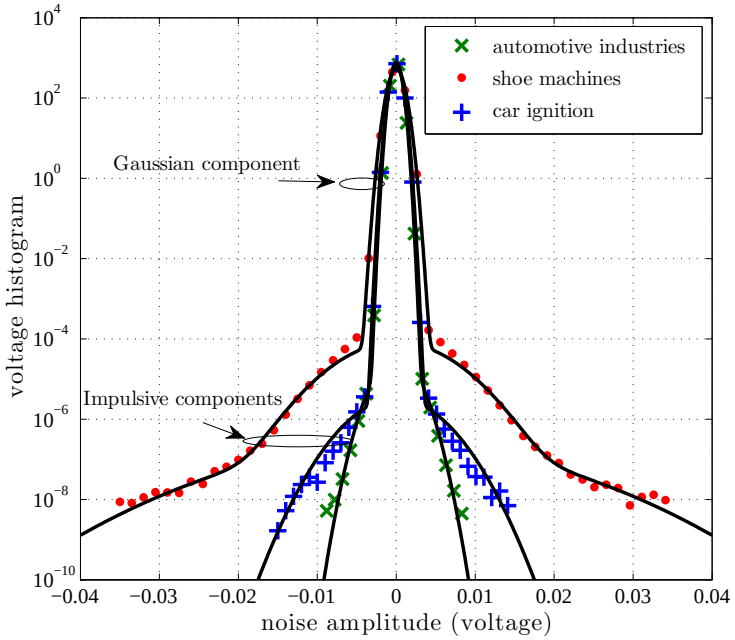

Figure 2.12: The voltage PDF of the measured interference caused by different ISM sources at 2.4 GHz

of shoe machine interference requires three terms of the MCA density. This result is in agreement with the impulsiveness of shoe machine interference, which is more dispersive and stronger than those of car ignition and automotive assembly machines (see Fig. 2.8).

To validate a complex extension of the MCA model given in (2.14), we convert the

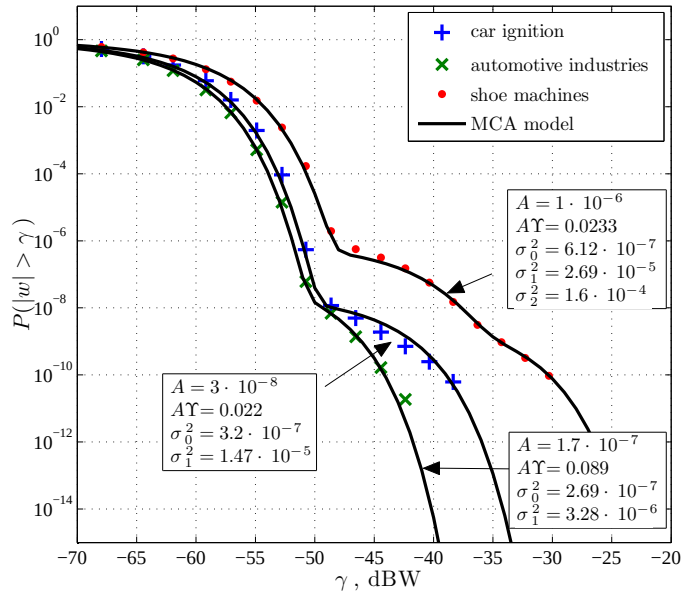

Figure 2.13: CCDF of measured interference caused by different ISM sources at 2.4 GHz

passband measurements into the equivalent lowpass signals (quadrature components). Figure 2.14 depicts the MCA fitting of the voltage histograms for the quadrature noise

components. We observe that the PDFs of the quadrature components follow the MCA

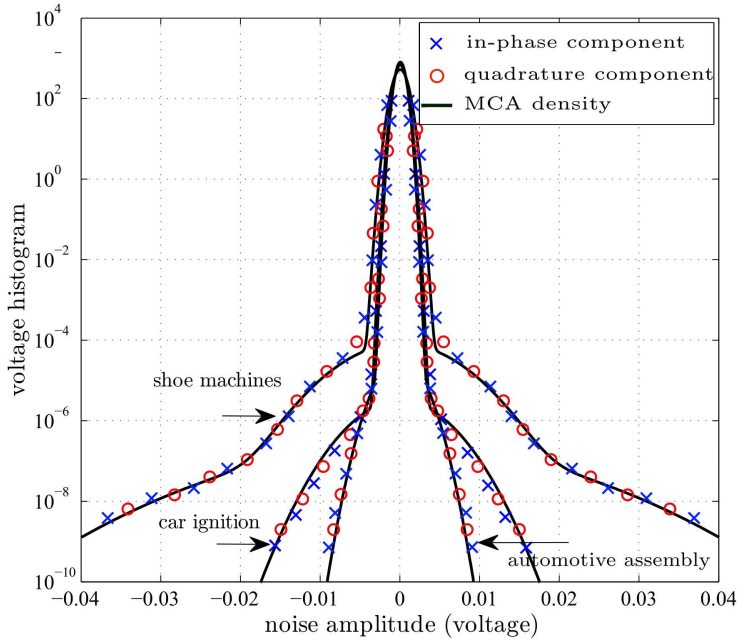

Figure 2.14: The MCA density and the voltage histograms of the quadrature components for baseband measurements

density of the passband measurements. This means that the lowpass noise process can be defined with the same parameters A and Υ of the passband noise process. Therefore, the results of Fig. 2.14 approve the complex MCA model in representing the baseband impulse noise.

2.3.2 Model Extension for Multi-antenna Systems

In this subsection, we verified the multivariate MCA model given in (2.20) to model the received interference from the different receive antennas. Thus, for each campaign, we computed the CCDF plots of the measured interference from the multiple receive antennas. Then, we investigated the spatial correlations of Gaussian components and impulsive components at the different receive antennas.

In Fig. 2.15 and 2.16, we depict the CCDF of the four measured data sets for impulse noise caused by car ignition and the automotive assembly machine, respectively. From both figures, we observe two interesting aspects. First, the MCA processes at the four receive antennas are possessing unequal average variances $\mathrm{E}\{w_{n_R}^2\}$, $n_R = 1, \cdots, 4$. Second, we note that the Gaussian factors, Υ_{n_R}, $\forall n_R$, are not necessarily identical, which leads to unequal variances σ_G^2 and σ_I^2 for the noise processes at the different receive antennas.

Regarding the multivariate MCA model given in (2.20), we note that the spatial correlation coefficients of the different MCA noise components are not identical. Thus, we compute the correlation coefficients of the measured segments from the first two antennas to prove this assumption. Table 2.1 summarizes the spatial correlations of the measured impulse noise. We observe that the correlation coefficient of the Gaussian

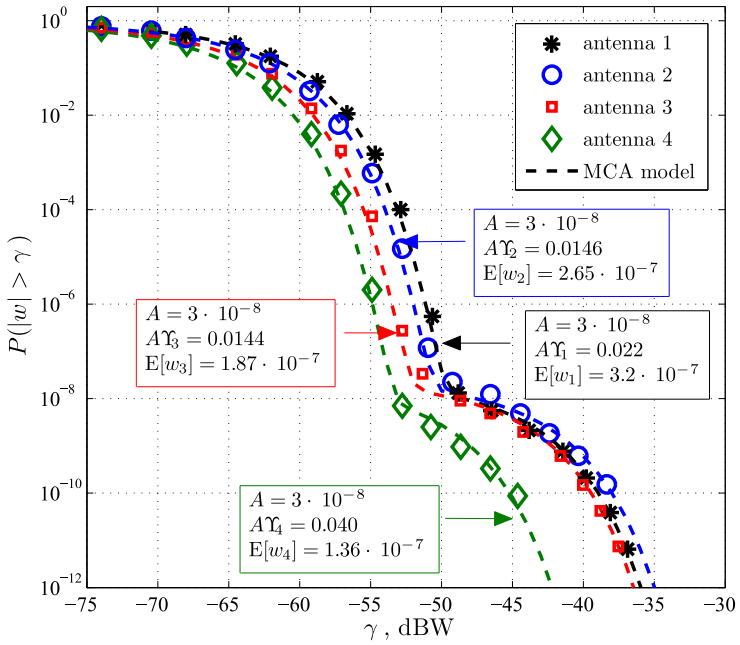

Figure 2.15: The multivariate MCA model and the measured CCDFs of impulse noise at an antenna array with $\lambda/4$ spacing caused by car ignition

component, $\rho_{G,12}$, is less than the correlation coefficient of the impulse component, $\rho_{I,12}$, for all measurements. This proves that the MCA noise components come with different levels of correlation.

Table 2.1: Spatial correlation coefficients of impulse noise

correlation coefficients	ignition	shoe machine	automotive assembly machine
$\rho_{G,12}$	0.35	0.18	0.0043
$\rho_{I,12}$	0.42	0.59	0.043

2.4 Conclusion

In this chapter, we summarized results from a measurement campaign to verify the statistical proprieties of the MCA model for ISM interference at 2.4 GHz. Analytically,

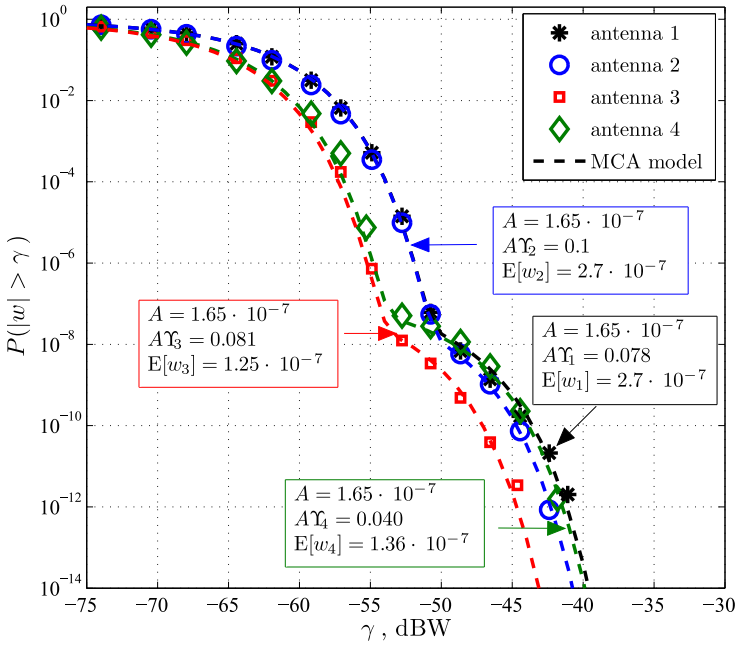

Figure 2.16: The multivariate MCA model and the measured CCDFs of impulse noise at an antenna array with $\lambda/4$ spacing caused by an automotive assembly machine

we evaluated the time and spatial properties of MCA interference. Using measurements, we verified the MCA model for the 2.4 GHz band wireless interference. We showed that the MCA distribution fits well to the voltage histograms of the measured data. In particular, we noted that two or three scaled Gaussian densities (with different variances) are sufficient to capture the impulsive behavior of 2.4 GHz wireless interference. We noted that the impulsive indexes, A, for different measurements are having small values, which reflect the small impulsive rate of interference at the 2.4 GHz band. For multiple antenna systems, we verified a correlated multivariate MCA distribution to model the spatial coupling and dependency of impulse noise between the receive antennas. The measurements showed that the interference of multiple receive antennas are having different variances for the Gaussian and impulsive components, which agrees with the assumption of unequal Gaussian factors in the multivariate MCA model. In addition, we showed that spatial correlations of the Gaussian component and the impulse component are not the same. The measured correlations are in agreement with the spatial coupling of a rudimentary MCA statistical-physical modeling for two-antenna systems in [46].

Chapter 3

Signal Detection in MCA Noise

In a detection problem of binary signals in MCA noise, we showed in Chapter 1 that the optimum detector consists of a set of nonlinear operations followed by a linear decision rule. The complex structure of these nonlinearities limits the literature into investigating the behaviors of the optimum detector in impulse noise.

In this chapter, we introduce a simple PDF representation of the MCA model, which leads to a closed-form approximation of the optimum nonlinearities. Then, we analyze the behaviors of the optimum detector in different impulse noise environments. In addition, we show for the first time how the decision boundaries of the optimum detector should look in the presence of MCA noise. Furthermore, we use the approximate nonlinearity to explain the operations of suboptimum nonlinearities such as a locally optimum nonlinearity and a clipping nonlinearity. Then, we further approximate the optimum nonlinearity to introduce new suboptimum detectors such as a piecewise linear detector and a clipping-like detector. We conclude with a performance evaluation and simulation results of the optimum and suboptimum detectors for different impulse noise scenarios.

3.1 Approximate Optimum Nonlinearity

In Section 1.2, we show that the optimum decision rule for binary signals corrupted by MCA noise can be given as

$$\Lambda_{ML} = \sum_{k=1}^{N} g(y_k) \underset{S_0}{\overset{S_1}{\gtrless}} 0 \ , \tag{3.1}$$

where

$$g(y_k) = \log\left(p_w(y_k - B)\right) - \log\left(p_w(y_k + B)\right) \ , \quad k = 1, \cdots, N \ , \tag{3.2}$$

and

$$p_w(w_k) = \sum_{m=0}^{\infty} \frac{\alpha_m}{\sqrt{2\pi\sigma_m^2}} \mathrm{e}^{-\frac{w_k^2}{2\sigma_m^2}} \,, \tag{3.3}$$

denotes the optimum nonlinearities and the MCA distribution, respectively. The main topic of this section is to reduce the optimum nonlinearities to closed-form approximations. In the following subsections, we introduce a simple representation of the MCA model, and hence, we derive closed-form approximations of the optimum nonlinearities.

3.1.1 A Simplified Model of MCA Noise

The 2-term approximation of the MCA density has already been applied in practical realization of the optimum nonlinearities [16]. For $A\Upsilon < 1$, the MCA model can be approximated as

$$p_w(w_k) \approx \overbrace{\frac{\alpha_0}{\sqrt{2\pi\sigma_0^2}} \mathrm{e}^{-\frac{w_k^2}{2\sigma_0^2}}}^{\text{Gaussian term}} + \overbrace{\frac{\alpha_1}{\sqrt{2\pi\sigma_1^2}} \mathrm{e}^{-\frac{w_k^2}{2\sigma_1^2}}}^{\text{Impulsive term}} \,, \tag{3.4}$$

where $\sigma_0^2 = \sigma^2 \frac{\Upsilon}{1+\Upsilon}$ and $\sigma_1^2 = \sigma_G^2(1+\frac{1}{A\Upsilon})$. Compared to (3.3), the first term of (3.4) models the Gaussian background noise (σ_G^2) while the second term approximates the densities of impulsive events $m > 1$. For $A\Upsilon < 1$, the MCA model often fulfills $\sigma_1^2 >> \sigma_0^2$. Then, we note that the MCA density can be approximated as follows:

$$p_w(w_k) \approx \begin{cases} \frac{\alpha_0}{\sqrt{2\pi\sigma_0^2}} \mathrm{e}^{-\frac{w_k^2}{2\sigma_0^2}} & \text{if } |w_k| < d_0 \,, \\ \frac{\alpha_1}{\sqrt{2\pi\sigma_1^2}} \mathrm{e}^{-\frac{w_k^2}{2\sigma_1^2}} & \text{otherwise} \,, \end{cases} \tag{3.5}$$

where d_0 denotes a threshold for discriminating impulse-free samples and affected samples by impulse noise. The threshold can be evaluated as

$$\frac{\alpha_0}{\sqrt{2\pi\sigma_0^2}} \mathrm{e}^{-\frac{w_k^2}{2\sigma_0^2}} = \frac{\alpha_1}{\sqrt{2\pi\sigma_1^2}} \mathrm{e}^{-\frac{w_k^2}{2\sigma_1^2}} \,, \tag{3.6}$$

leading to

$$\begin{aligned} w_k &= \pm\sqrt{\frac{2\sigma_0^2\sigma_1^2}{\sigma_1^2 - \sigma_0^2} \log\left(\frac{\sigma_1\alpha_0}{\sigma_0\alpha_1}\right)} \,, \\ &=: \pm d_0 \,. \end{aligned} \tag{3.7}$$

Figure 3.1 confirms the idea behind the approximate MCA model. In this figure, we depict

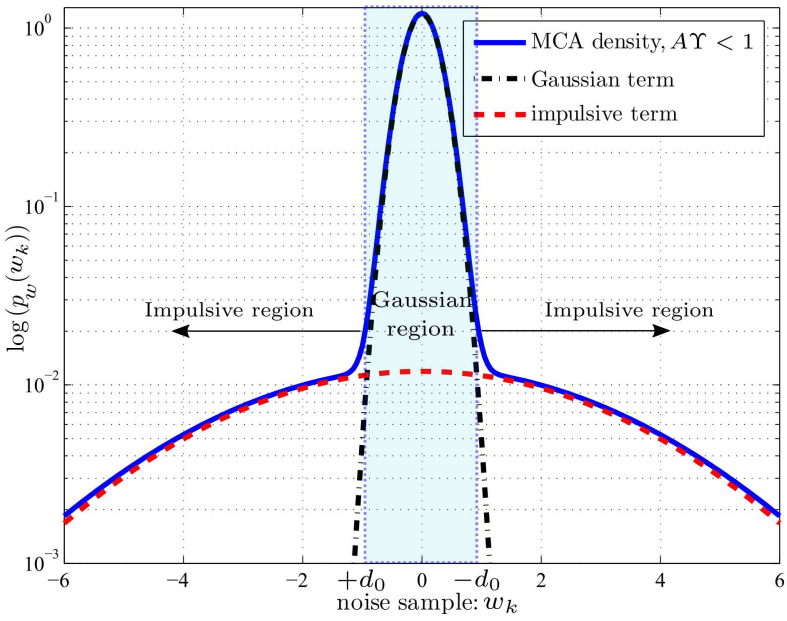

Figure 3.1: The plots of the MCA distribution compared with the approximate model

the MCA distribution, the Gaussian term, and the impulsive term of (3.4). We note that the thresholds $w_k = \pm d_0$ divide the MCA distribution into three separate regions. In the region $-d_0 < w_k < d_0$, we observe that the Gaussian term dominates the MCA density. However, in regions $w_k > d_0$ and $w_k < -d_0$, we note that the impulsive term is sufficient to approximate the tails of the MCA density.

3.1.2 Near Optimum Nonlinearities

For binary signaling $+B$ and $-B$, the received observation y_k form a one-dimensional space. Hence, the conditional PDFs of the received observation under hypotheses S_1 and S_0 can be depicted as shown in Fig. 3.2. From (3.5), the likelihood functions $p_w(y_k - B)$

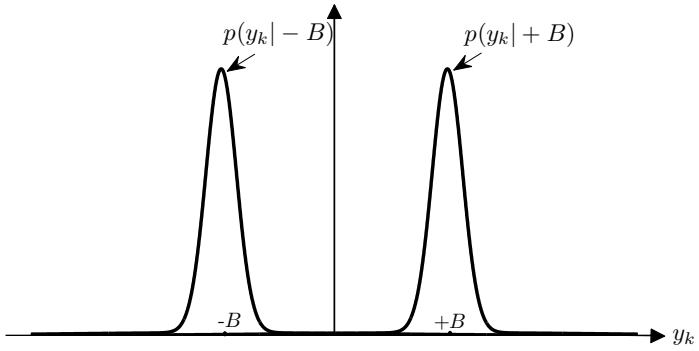

Figure 3.2: Conditional PDFs of binary signals in MCA noise

and $p_w(y_k + B)$ can be rewritten as

$$p_w(y_k - B) \approx \begin{cases} \frac{\alpha_0}{\sqrt{2\pi\sigma_0^2}} e^{-\frac{(y_k-B)^2}{2\sigma_0^2}} & \text{if } |y_k - B| < d_0 \ , \\ \frac{\alpha_1}{\sqrt{2\pi\sigma_1^2}} e^{-\frac{(y_k-B)^2}{2\sigma_1^2}} & \text{otherwise} \ , \end{cases} \tag{3.8}$$

and

$$p_w(y_k + B) \approx \begin{cases} \frac{\alpha_0}{\sqrt{2\pi\sigma_0^2}} e^{-\frac{(y_k+B)^2}{2\sigma_0^2}} & \text{if } |y_k + B| < d_0 \ , \\ \frac{\alpha_1}{\sqrt{2\pi\sigma_1^2}} e^{-\frac{(y_k+B)^2}{2\sigma_1^2}} & \text{otherwise} \ , \end{cases} \tag{3.9}$$

respectively. The above approximations divide the processing regions of optimum nonlinearities (3.2) into five regions R_0, R_1, R_2, R_3, and R_4 as illustrated in Fig. (3.3). In

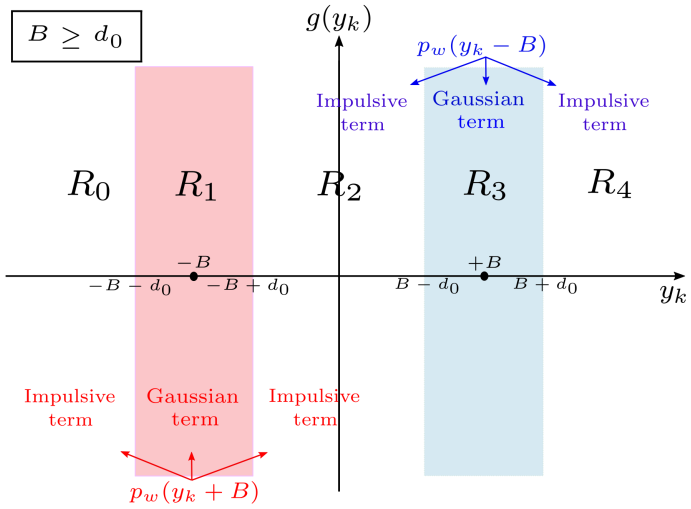

Figure 3.3: Processing regions of the nonlinearity operation

regions R_0, R_2, and R_4, we have

$$\begin{aligned} p_w(y_k - B) &\approx \frac{\alpha_1}{\sqrt{2\pi\sigma_1^2}} e^{-\frac{(y_k-B)^2}{2\sigma_1^2}} \ , \\ p_w(y_k + B) &\approx \frac{\alpha_1}{\sqrt{2\pi\sigma_1^2}} e^{-\frac{(y_k+B)^2}{2\sigma_1^2}} \ . \end{aligned} \tag{3.10}$$

Now substituting (3.10) into (3.2), the optimum nonlinearity reduces to

$$g(y_k \in R_{0,2,4}) \approx \frac{2B}{\sigma_1^2} y_k \ . \tag{3.11}$$

In the region R_1, the likelihood functions are simply

$$\begin{aligned} p_w(y_k - B) &\approx \frac{\alpha_1}{\sqrt{2\pi\sigma_1^2}} \mathrm{e}^{-\frac{(y_k-B)^2}{2\sigma_1^2}} \ , \\ p_w(y_k + B) &\approx \frac{\alpha_0}{\sqrt{2\pi\sigma_0^2}} \mathrm{e}^{-\frac{(y_k+B)^2}{2\sigma_0^2}} \ . \end{aligned} \tag{3.12}$$

Then, (3.2) reduces to

$$g(y_k \in R_1) \approx -\frac{\sigma_1^2 - \sigma_0^2}{2\sigma_1^2\sigma_0^2} \left(d_0^2 - \left(y_k^2 + 2B\frac{\sigma_1^2 + \sigma_0^2}{\sigma_1^2 - \sigma_0^2} y_k + B^2 \right) \right) \ . \tag{3.13}$$

Using similar mathematical steps, the nonlinearity of the region R_3 is given as

$$g(y_k \in R_3) \approx \frac{\sigma_1^2 - \sigma_0^2}{2\sigma_1^2\sigma_0^2} \left(d_0^2 - \left(y_k^2 - 2B\frac{\sigma_1^2 + \sigma_0^2}{\sigma_1^2 - \sigma_0^2} y_k + B^2 \right) \right) \ . \tag{3.14}$$

In Fig. 3.4, we depict the exact nonlinearities compared with the approximate ones for Class-A noise with parameters $A = 0.1$ and $\Upsilon = 0.1$ for $B \geq d_0$. This figure illustrates the behaviors of the approximate and the optimum nonlinearities for canceling the effects of MCA noise. We observe that the regions R_1 and R_3 stand for the received signals

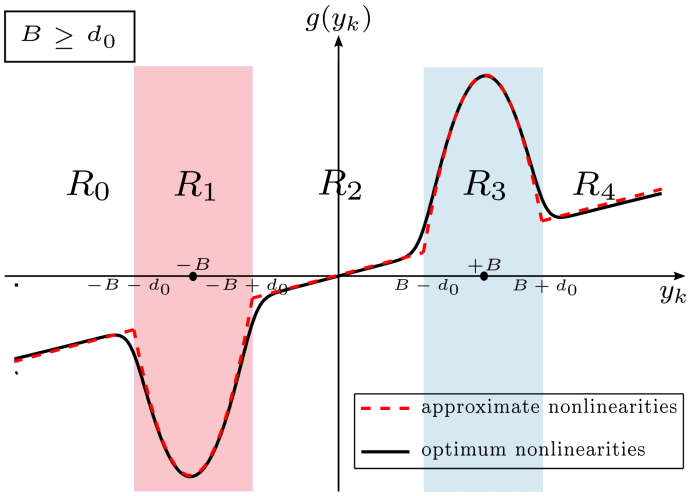

Figure 3.4: The optimum and the approximate nonlinearities for $B \geq d_0$

corrupted by Gaussian noise for hypotheses S_0 and S_1, respectively. Thus, these regions can be seen as regions of reliable observations relative to impulsive regions R_0, R_2, and R_4. From (3.13) and (3.14), we note that the optimum nonlinearities in Gaussian regions R_1 and R_3 use a parabola function, which increases the weight of the reliable observations. However, in impulsive regions R_0, R_2, and R_4, we observe that the received signal is scaled down by a factor that is inversely proportional to the variance σ_1^2. Thus, the

reliable signals in Gaussian regions carry a larger weight than those of impulsive regions, which illustrates how the optimum nonlinearity treats the effects of impulse noise.
The above analysis is well-suited for high signal levels, i.e., when $B \geq d_0$. However, when $B < d_0$, the region R_2 should overlap the Gaussian regions R_1 and R_3. Then, the optimum nonlinearity becomes

$$g(y_k \in R_2) \approx \frac{2B}{\sigma_0^2} y_k \ . \tag{3.15}$$

Figure 3.5 depicts the behaviors of the approximate and optimum nonlinearities for small signal levels. We observe that the approximate nonlinearity in the region R_2 weights the

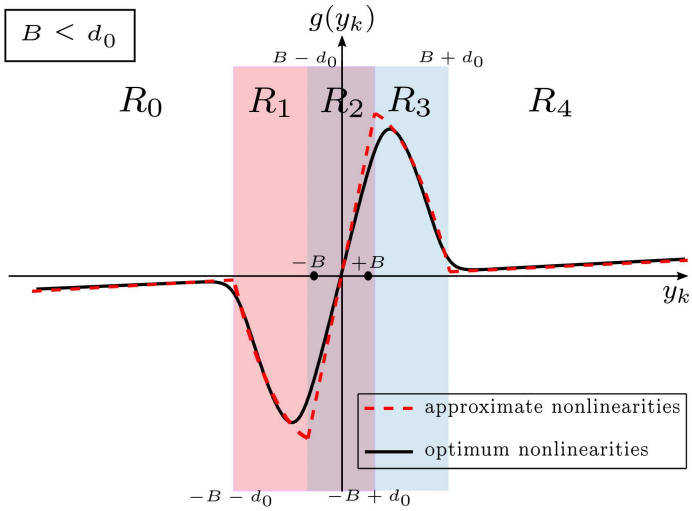

Figure 3.5: The optimum and approximate nonlinearities for $B < d_0$

signals by a factor that is inversely proportional to the variance σ_0^2, which depicts how the optimum detector behaves at low signal levels.

3.2 Decision Regions in MCA Noise

In this Section, we investigate the decision regions of the optimum detector in the presence of MCA noise. We show how the decision regions should look like for different impulse noise environments.

3.2.1 Decision Boundary Evaluation

In this analysis, we consider a two-dimensional decision space of two received samples, i.e., $\mathbf{y} = [y_1 \ y_2]$. Figure 3.6 illustrates the decision space of binary signals for the two

received observations. We observe that the received observations are centered at signal points $(+B, +B)$ and $(-B, -B)$ for hypotheses S_1 and S_0, respectively. From (1.13), the optimum decision boundary is given as

$$\sum_{k=1}^{2} \log\left(p_w(y_k - B)\right) = \sum_{k=1}^{2} \log\left(p_w(y_k + B)\right) . \tag{3.16}$$

We again use the approximate likelihood functions given in (3.8) and (3.9) to derive the optimum decision boundary in a closed-form expression. In Fig. 3.6, we depict the regions

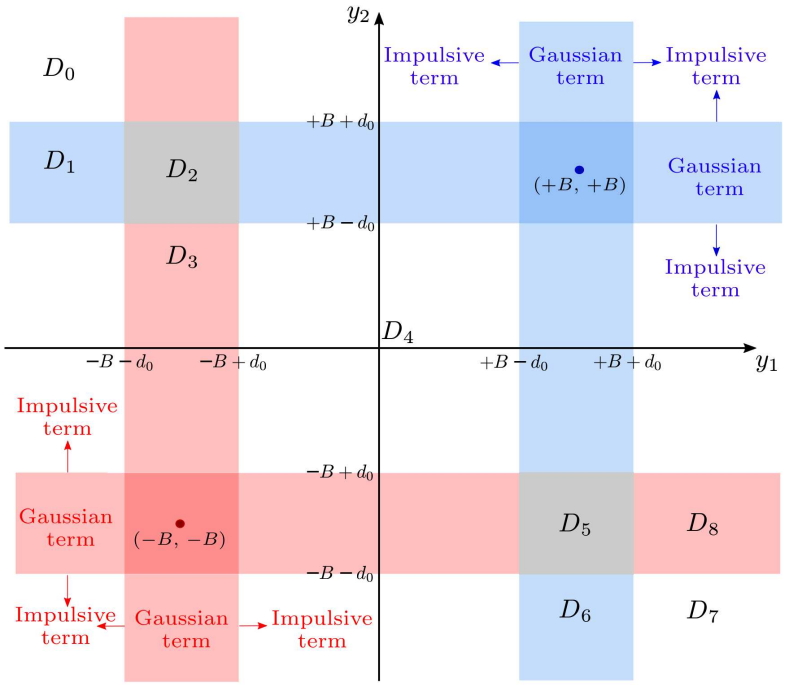

Figure 3.6: The decision regions of binary signals in MCA noise

of the decision space for hypotheses S_1 and S_0. We observe that the decision space has nine regions to be distinguished. Since the regions for the second and fourth quadrants are identical, we restrict the analytical derivation for the regions of the second quadrant. From Fig. 3.6, in regions D_0 and D_4, the impulsive terms are the dominant terms for $p_w(y_{1,2} - B)$ and $p_w(y_{1,2} + B)$. Then, the decision boundary can be expressed as

$$\sum_{k=1}^{2} \log\left(\frac{\alpha_1}{\sqrt{2\pi\sigma_1^2}} \mathrm{e}^{-\frac{(y_k - B)^2}{2\sigma_1^2}}\right) = \sum_{k=1}^{2} \log\left(\frac{\alpha_1}{\sqrt{2\pi\sigma_1^2}} \mathrm{e}^{-\frac{(y_k + B)^2}{2\sigma_1^2}}\right) , \tag{3.17}$$

which can be solved as

$$y_2 = -y_1 . \tag{3.18}$$

The above solution is the exact linear decision boundary of the optimum detector in AWGN [45]. In D_1, the likelihood functions $p_w(y_1 - B)$, $p_w(y_1 + B)$, and $p_w(y_2 + B)$ can be approximated by the impulsive terms, whereas $p_w(y_2 - B)$ is given by the Gaussian term. Then, the decision boundary is solved as

$$y_1 = \frac{\sigma_0^2 - \sigma_1^2}{4B\sigma_0^2} \left(d_0^2 - (y_2^2 - 2B\frac{\sigma_1^2 + \sigma_0^2}{\sigma_1^2 - \sigma_0^2} y_2 + B^2) \right) . \tag{3.19}$$

Similarly, in D_2, we obtain

$$y_2 = -y_1 , \tag{3.20}$$

$$y_2 = y_1 + \frac{\sigma_1^2 + \sigma_0^2}{\sigma_1^2 - \sigma_0^2} , \tag{3.21}$$

and finally, in D_3, we have

$$y_2 = \frac{\sigma_1^2 - \sigma_0^2}{4B\sigma_0^2} \left(d_0^2 - (y_1^2 - 2B\frac{\sigma_1^2 + \sigma_0^2}{\sigma_0^2 - \sigma_1^2} y_1 + B^2) \right) . \tag{3.22}$$

In order to compare the decision boundaries of the above analysis with the exact boundaries of the optimum detector, we used a numerical method for solving (3.16). Figure 3.7 depicts the approximate and optimum decision boundaries for the optimum detector in MCA noise with parameters $A = 0.1$ and $\Upsilon = 0.1$. In this figure, we observe that the approximate boundaries offer a tractable solution for the optimum decision boundaries. We note that the decision boundaries of both solutions possess disjoint nonlinear areas. From figures 3.7 and 3.4, it is interesting to note that the nonlinear decision areas for hypotheses S_1 and S_0 provide the same treatments of the optimum nonlinearities in nonlinear regions R_3 and R_1, respectively. However, the above figure depicts how the nonlinearity operations modify the decision boundary of the optimum detector for the two received observations. In addition, the figure justifies why the linear detector, which ignores the nonlinear decision areas, provides a suboptimum performance in impulse noise.

3.2.2 Decision Boundary Analysis

We use the decision boundary to investigate the performance of the optimum detector in different impulse noise environments. First, we examine the decision boundary plots for different signal levels. Then, we investigate the decision boundaries in impulse noise with different impulsive index, A. Figure 3.8 depicts the nonlinear decision boundaries at different values of $E_b/2\sigma^2$. Since $\sigma^2 = \sigma_G^2 + \sigma_I^2$, the ratio $E_b/2\sigma^2$ can be seen as the

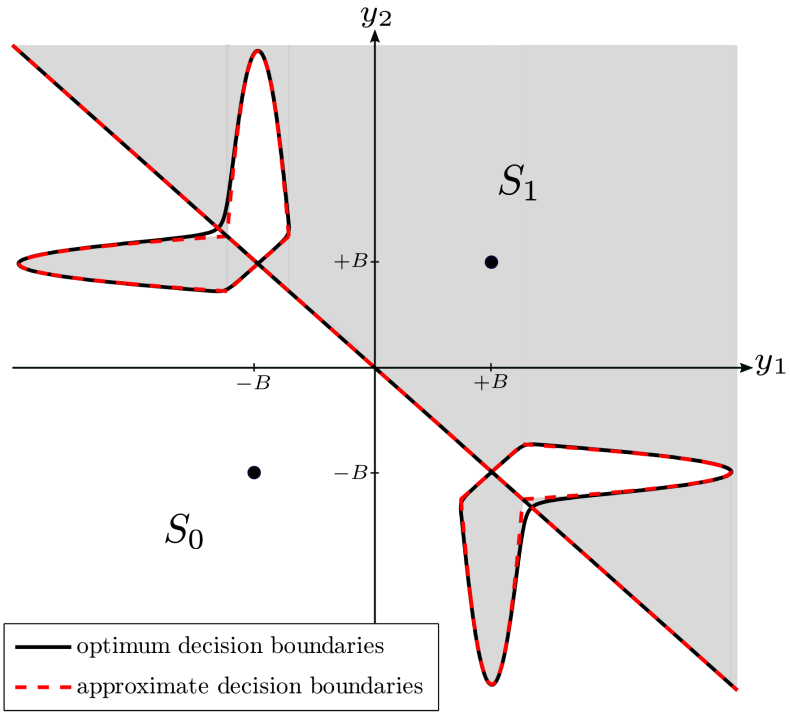

Figure 3.7: The optimum and approximate decision regions in MCA noise with $A = 0.1$, $\Upsilon = 0.1$ for $B \geq d_0$. Shaded area: decide for S_1, white area: decide for S_0

Signal-to-interference-plus-noise ratio (SINR). We note that, at high SINR, the decision boundaries possess small nonlinear regions. This justifies why the performance of the optimum detector recede to the performance of the linear detector at high SINRs [14]. In Fig. 3.9, we depict the decision boundaries for different values of A at SINR=10 dB. We observe that as A increases, the nonlinear regions approach the linear boundary. Hence, the decision boundaries reduce to a single linear boundary, which is optimum for Gaussian interference. This is true, since the MCA density goes to the Gaussian distribution (with variance σ^2) when A goes to 1.

3.3 Suboptimum Detectors in MCA Noise

In this section, we use the approximate nonlinearities of the optimum detector to evaluate the nonlinearity operations of a locally optimum detector and a clipping detector for MCA noise. Hence, we introduce a piecewise linear detector, which replaces the optimum nonlinearity with linear segments. Accordingly, we modify the clipping nonlinearity to fit the optimum nonlinearity more than a conventional clipping operation.

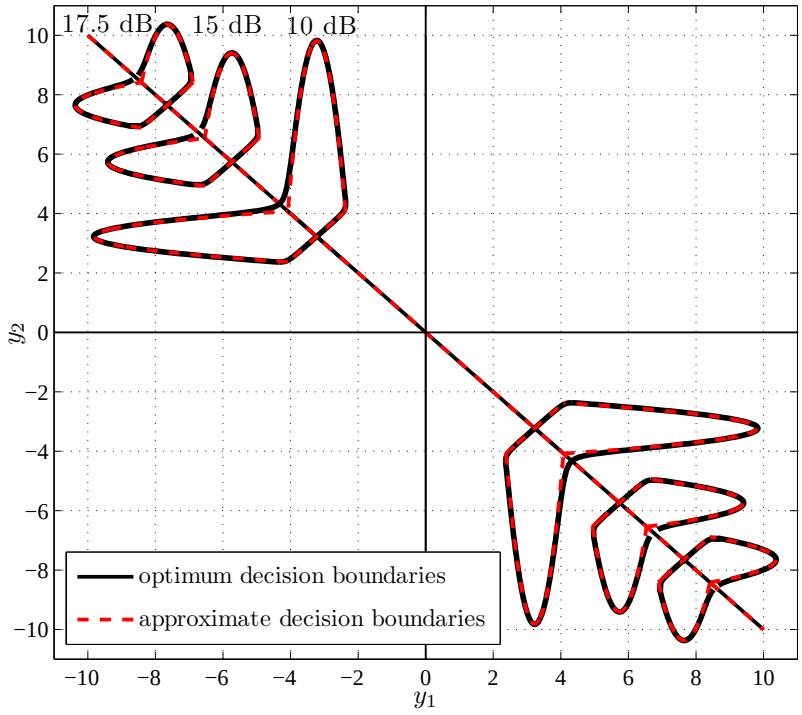

Figure 3.8: Decision regions at different SINRs for $A = 0.1$ and $\Upsilon = 0.1$

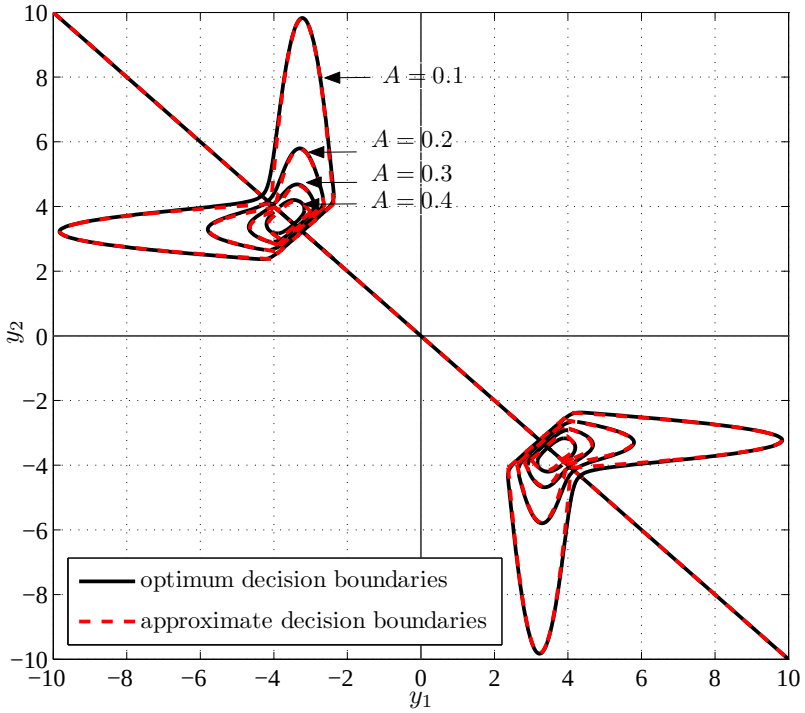

Figure 3.9: Decision regions for different A with $\Upsilon = 0.1$ at SINR = 10 dB

3.3.1 Nonlinearities of Suboptimum Detectors

Recall from Section 1.2 that the nonlinearities of the LOD and the clipping detector can be given as

$$g_{LO}(y_k) = -2B\frac{d}{dy_k}\log\left(p(y_k)\right) \ , \tag{3.23}$$

and

$$g_{CD}(y_k) = \begin{cases} y_k \ , & |y_k| < \gamma_c \ , \\ \gamma_c e^{j\arg(y_k)} \ , & |y_k| \geq \gamma_c \ , \end{cases} \tag{3.24}$$

where γ_c is the clipping threshold given in (1.23). In figures 3.10 and 3.11, we depict the locally optimum and clipping nonlinearities compared with those of the optimum detector for small and high signal levels, respectively. From Fig. 3.10, we observe that the

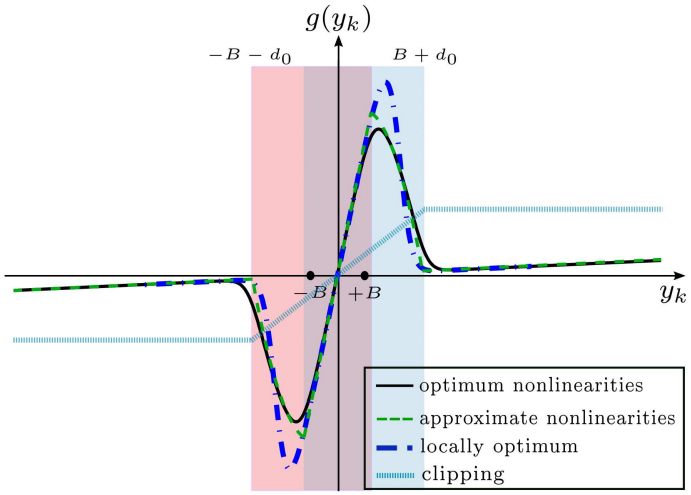

Figure 3.10: Suboptimum nonlinearities for $B < d_0$

locally optimum nonlinearities, for $B < d_0$, provide close operations to the optimum ones. However, when the signal level $B \geq d_0$, we observe that the LOD provides different nonlinearities than those of the optimum detector. This justifies the performance degradation of the LOD at high signal levels. Into these figures, we also included a clipping nonlinearity. We observe that the nonlinearity of a conventional clipping detector does not provide a good approximation to the optimum one.

3.3.2 Piecewise Linear Detector

Since the optimum detector for impulse noise requires more complexity than the conventional linear detector, this moves the attention to investigate suboptimum detectors. The

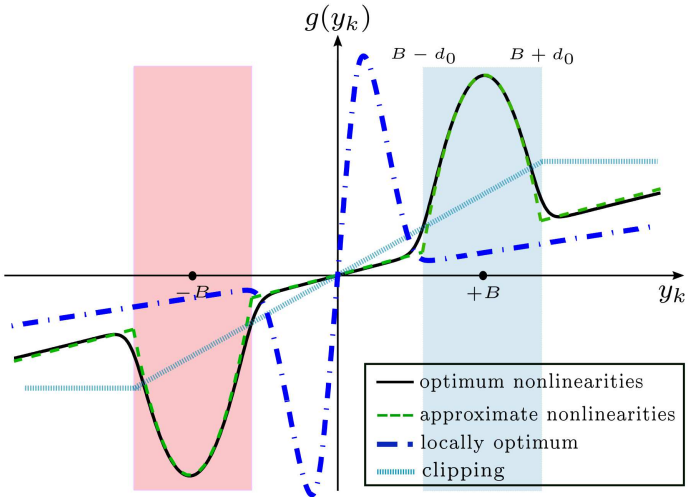

Figure 3.11: Suboptimum nonlinearities for $B \geq d_0$

piecewise linear detector replaces the nonlinearity of the optimum detector by piecewise linear segments. In (3.13) and (3.14), it is obvious that the approximate nonlinearities are quadratic functions in regions R_1 and R_3, respectively. Since those functions are symmetric, we only present the analysis of the region R_3. The quadratic function of R_3 can be written as

$$q(y_k) = y_k^2 - 2B\frac{\sigma_1^2 + \sigma_0^2}{\sigma_1^2 - \sigma_0^2}y_k + B^2 \ , \quad y_k \in [u_0,\, u_K] \ , \tag{3.25}$$

where u_0 and u_K are the limits of the region R_3. From figures 3.4 and 3.5, we observe that the limits u_0 and u_K can be given as follow:

$$u_0 = \begin{cases} -B + d_0 & \text{if } B < d_0 \ , \\ B - d_0 & \text{if } B \geq d_0 \ , \end{cases} \tag{3.26}$$

and

$$u_K = B + d_0 \ . \tag{3.27}$$

Since we intend to approximate $q(y_k)$ using simple piecewise linear segments, we divide the interval $[u_0,\, u_K]$ into K subintervals as illustrated in Fig. 3.12. The objective is to determine the fitting parameters a_i and b_i of a linear segment $q_i(y_k) = a_i y_k + b_i$, which approximates $q(y_k)$ inside the i^{th} subinterval $[u_{i-1},\, u_i]$, $i = 1, \cdots, K$. Herewith, we choose a_i and b_i to minimize the mean squared error

$$\varepsilon_i = \int_{u_{i-1}}^{u_i} |q(y_k) - q_i(y_k)|^2 dy_k \ . \tag{3.28}$$

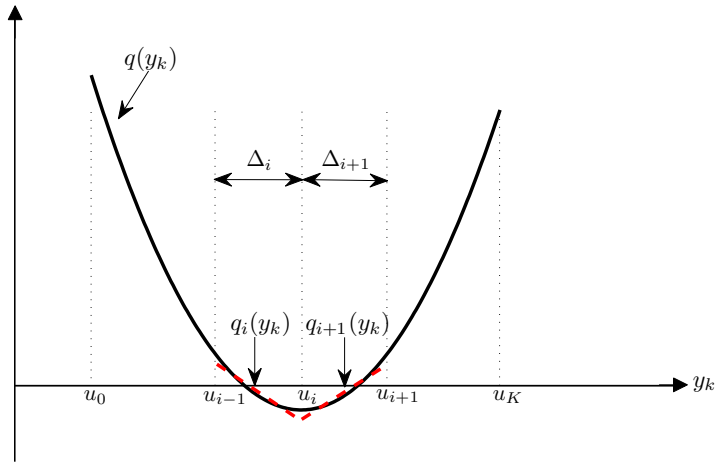

Figure 3.12: Piecewise linear approximation of the function $q(y_k)$

This function can easily be minimized with respect to the coefficients a_i and b_i to yield the following solutions

$$a_i = u_{i-1} + u_i - 2B\frac{\sigma_1^2 + \sigma_0^2}{\sigma_1^2 - \sigma_0^2} \,, \tag{3.29}$$

and

$$b_i = B^2 - \frac{u_{i-1}^2 + u_i^2 + 4u_{i-1}u_i}{6} \,. \tag{3.30}$$

To compute the segment spacing Δ_i, solving $q_i(u_i) = q_{i+1}(u_i)$ yields

$$\Delta_i = \frac{u_{i+1} - u_{i-1}}{2} \,, \tag{3.31}$$

which results in equally-spaced subintervals, i.e., $\Delta_{i+1} = \Delta_i = \Delta$. Notice that when $q(y_k)$ is not quadratic the solution will not necessarily lead to equally-spaced subintervals.

Two-piece Linear Approximation: This detector uses two linear segments, $K = 2$, to approximate the function $q(y_k)$ in subintervals $[u_0, u_1]$ and $[u_1, u_K]$. From (3.31) and (3.26), we define u_1 as

$$\begin{aligned} u_1 &= u_0 + \Delta \,, \\ &= \begin{cases} d_0 & \text{if } B < d_0 \,, \\ B & \text{if } B \geq d_0 \,. \end{cases} \end{aligned} \tag{3.32}$$

The two-piece functions $q_1(y_k)$ and $q_2(y_k)$ are then given as

$$\begin{aligned} q_1(y_k) &= a_1 y_k + b_1 \,, \quad y_k \in [u_0,\, u_1] \,, \\ q_2(y_k) &= a_2 y_k + b_2 \,, \quad y_k \in [u_1,\, u_K] \,, \end{aligned} \tag{3.33}$$

where the coefficients (a_1, b_1) and (a_2, b_2) can be obtained analytically by substituting (3.26), (3.27), and (3.32) into (3.29) and (3.30).

Clipping-like Detector: Using the approximate optimum nonlinearities, the clipping characteristic can accordingly be modified to provide a more efficient treatment of MCA noise. The clipping-like detector uses the same linear operation of the approximate nonlinearity in the region R_2. However, it limits the received signals in the nonlinear regions to a certain threshold, b_0. This is equivalent to replacing the nonlinear functions in (3.25) with an adaptive limiter $q_0(y_k) = b_0$. Again, we choose b_0 to minimize the mean squared error as follows:

$$\varepsilon = \int_{u_0}^{u_K} |q(y_k) - b_0|^2 dy_k \,, \tag{3.34}$$

which leads to

$$b_0 = B^2 - B\frac{\sigma_1^2 + \sigma_0^2}{\sigma_1^2 - \sigma_0^2}(u_0 + u_K) + \frac{1}{3}(u_0^2 + u_K^2) + \frac{1}{3}u_0 u_K \,. \tag{3.35}$$

Hence, the clipping threshold for the region R_3 can be given as

$$\gamma_0 = \frac{\sigma_1^2 - \sigma_0^2}{\sigma_1^2 \sigma_0^2}\left(d_0^2 - b_0\right) \,. \tag{3.36}$$

From (3.36) and (3.35), we observe that the clipping threshold for R_3 is adapted according to the value of u_0. However, in the impulsive region R_4, we replace the linear operation $\frac{2B}{\sigma_1^2} y_k$ by a fixed threshold $\frac{2B}{\sigma_1^2} u_K$. Thus, the clipping-like nonlinearity performs two clipping operations as

$$g_{CLD}(y_k) = \begin{cases} \frac{2B}{\sigma_m^2} y_k \,, & |y_k| < u_0 \,, \\ \gamma_0 \mathrm{e}^{j \arg(y_k)} \,, & u_0 < |y_k| < u_K \,, \\ \frac{2B}{\sigma_1^2} u_K \mathrm{e}^{j \arg(y_k)} \,, & |y_k| \geq u_K \,, \end{cases} \tag{3.37}$$

where the index $m = 0$ for $u_0 = -B + d_0$ and $m = 1$ for $u_0 = B - d_0$. Figures (3.13) and (3.14) show the operations of a clipping-like and a two-piecewise nonlinearity for small and high signal levels, respectively. Although the two-piece linear approximation can easily be extended to an arbitrary number of linear segments, we observe from these figures that the two segments seem sufficient to fit the optimum nonlinearities. We also observe that

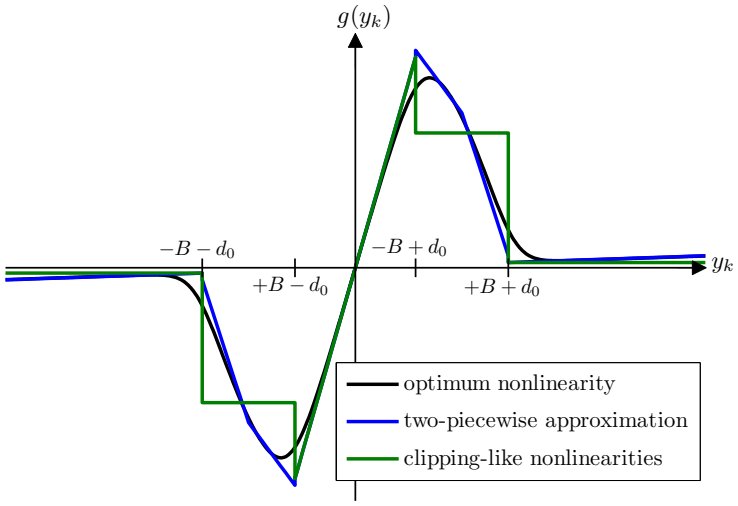

Figure 3.13: Piecewise nonlinearities for $B < d_0$

the clipping-like nonlinearities with the adaptive clipping thresholds can provide a better approximation than those of the conventional clipping detector.

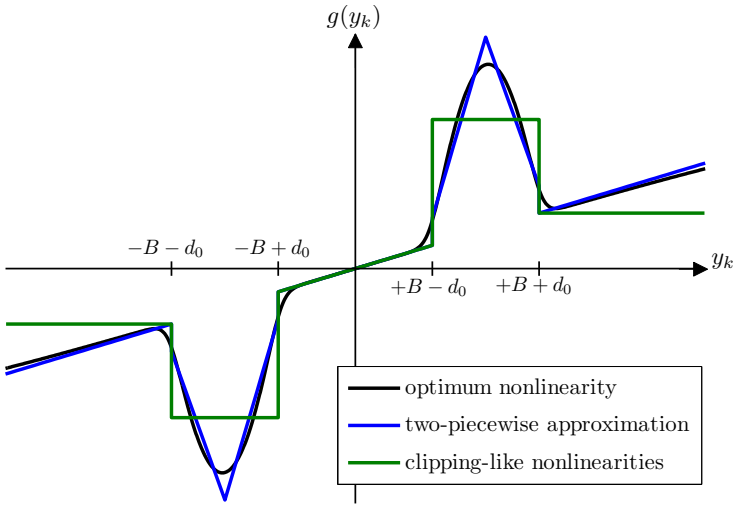

Figure 3.14: Piecewise nonlinearities for $B \geq d_0$

3.4 Performance Evaluation and Simulation Results

This section presents simulation results to assess the bit-error ratio (BER) of the approximate nonlinearities compared with those of the optimum detector.

3.4.1 The Performance of the Optimum Detector

We first evaluate the BER performance of the optimum detector in different impulse noise environments. Figure 3.15 depicts the BER performances the optimum and the approximate nonlinearities in impulse noise with $A = 1$; 0.1; 0.01 and $\Upsilon = 0.01$ for $N = 4$. We observe that the approximate nonlinearities provide performances close to those of

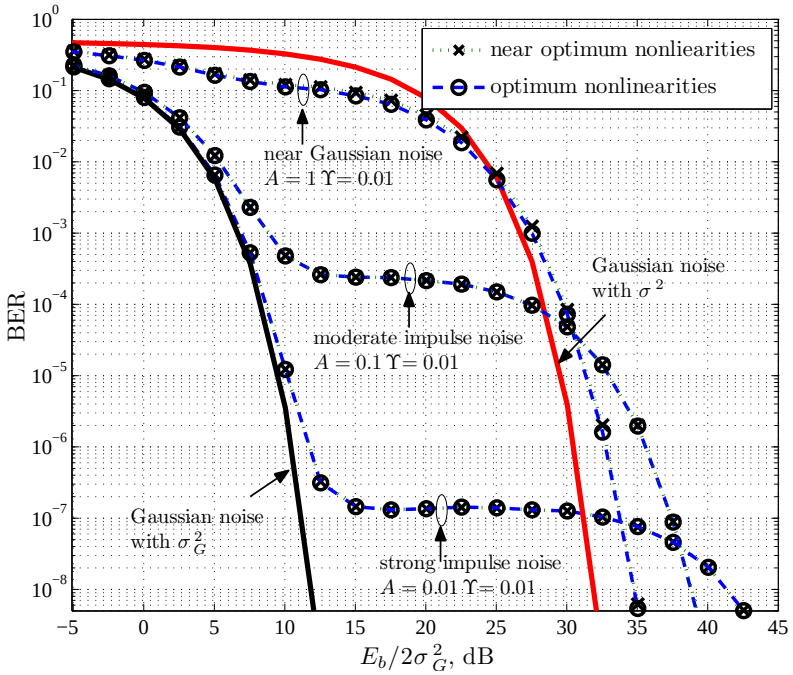

Figure 3.15: Performance comparison in different impulse noise environments for $N = 4$

the optimum one. Furthermore, we note that as A increases, the BER performance of the optimum detector approaches the one for Gaussian noise with variance σ^2. This agrees with the PDF of MCA noise, which goes to a Gaussian distribution with σ^2 for $A \geq 1$. Now, we examine the performance improvement of the optimum detector when increasing the number of received observations, N. In Fig. 3.16, we depict the BER performances versus the signal-to-noise ratio (SNR), $E_b/2\sigma_G^2$, of the optimum and the approximate nonlinearities in impulse noise with $A = 0.1$ and $\Upsilon = 0.01$ for $N = 1$, 4, and 8, respectively. We observe that the approximate nonlinearities yield performances close to those of the optimum one for different N. The shown figure allows for some interesting statements about the performance variations of the optimum detector. We observe that the BER curve of the optimum detector, for different N, has a plateau shape with respect to $E_b/2\sigma_G^2$. At low SNRs, the optimum nonlinearities provide a BER performance near to the one for Gaussian noise with variance σ_G^2 (impulse-free limit). At moderate values of the SNR, the BER curve shows an error floor. At high SNRs, the gap (the width of a plateau curve) between the BER curve of the impulse-free limit and impulse noise is given

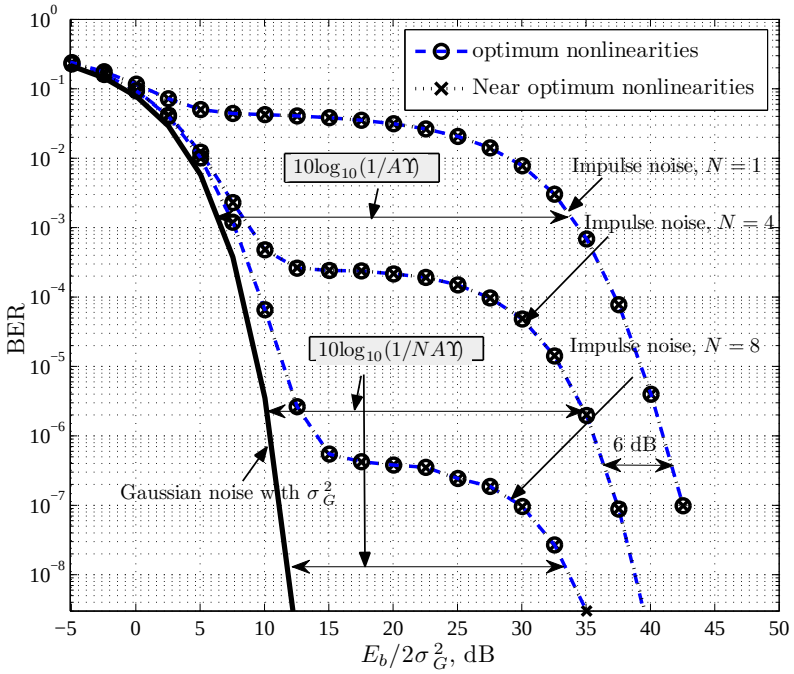

Figure 3.16: Performance comparison of the optimum and approximate detector in moderate MCA impulse noise with $A = 0.1$ and $\Upsilon = 0.01$ for different N

by $\frac{1}{NA\Upsilon}$. To deduce the performance variations of the optimum detector, we investigate the behaviors of the approximate optimum nonlinearities at different values of the SNR. Figure 3.17 illustrates two different operations of the optimum nonlinearities with respect to the value of the SNR. For small values of the SNR, we observe that the intervals of the

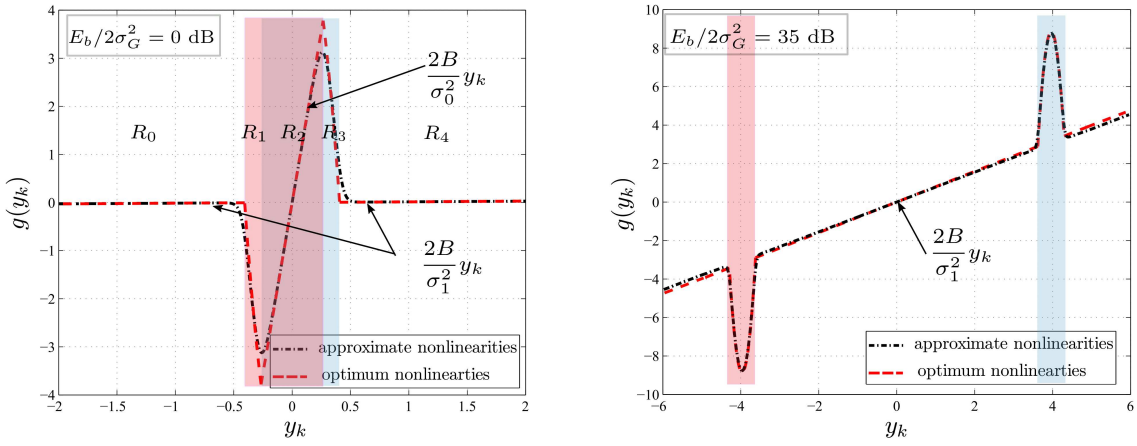

(a) Low SNR (b) High SNR

Figure 3.17: The nonlinearity operations at two different values of $E_b/2\sigma_G^2$

nonlinear regions R_1 and R_3 are very short compared with the intervals of linear regions R_0, R_2, and R_4. Hence, the operations of the optimum nonlinearities is dominated by

those of the linear regions. Thus, the optimum detector can be approximated as

$$\Lambda_{ML} \approx \sum_{k=1}^{N} \frac{2B}{\sigma_k^2} y_k \ , \tag{3.38}$$

where $\sigma_k^2 = \sigma_G^2$ for $y_k \in R_2$ and $\sigma_k^2 = \sigma_1^2$ for $y_k \in \{R_0, R_4\}$. The expression in (3.38) represents the optimum combining scheme of the received observations in Gaussian noise with unequal variances. Accordingly, as N increases, the diversity order also increases, and hence, the performance of the optimum detector improves. This justifies the performance improvements (see Fig. 3.16) of the optimum detector at low SNRs as N increases. However, at high values of the SNR, we note in Fig. 3.17b) that the optimum nonlinearities can be approximated by a single linear operation. Thus, the optimum detector reduces to a linear detector as

$$\Lambda_{ML} \approx \sum_{k=1}^{N} \frac{2B}{\sigma_1^2} y_k \ . \tag{3.39}$$

The above expression justifies the performance gaps observed in Fig. 3.16 between the performances of the optimum detectors for Gaussian noise σ_G^2 (impulse-free limit) and impulse noise at high values of the SNR.

3.4.2 Performances of the Suboptimum Detectors

In Fig. 3.18, we evaluate the performances of the proposed suboptimum detectors in moderate impulse noise with $A = 0.1$ and $\Upsilon = 0.01$ for two different number of received observations $N = 4$ and 8. The figure illustrates several aspects regarding the performance achievements of the suboptimum detectors. First, we observe that the two-piece linear segments are sufficient to approach the optimum performance for both numbers of received observations. Second, we observe that the proposed clipping-like detector provides much better performance than the conventional clipping detector. Compared to the optimum detector, we note that the clipping-like detector provides a tight upper performance bound to the optimum detector. Last, we note that the performance of the proposed suboptimum detectors improves with increasing the number of observations, N. At high SNRs, we observe that the detectors with $N = 8$ provide a 3 dB gain over those with $N = 4$. This means that the proposed suboptimum detectors maintain the same improvements of the optimum detector at high values of the SNR.

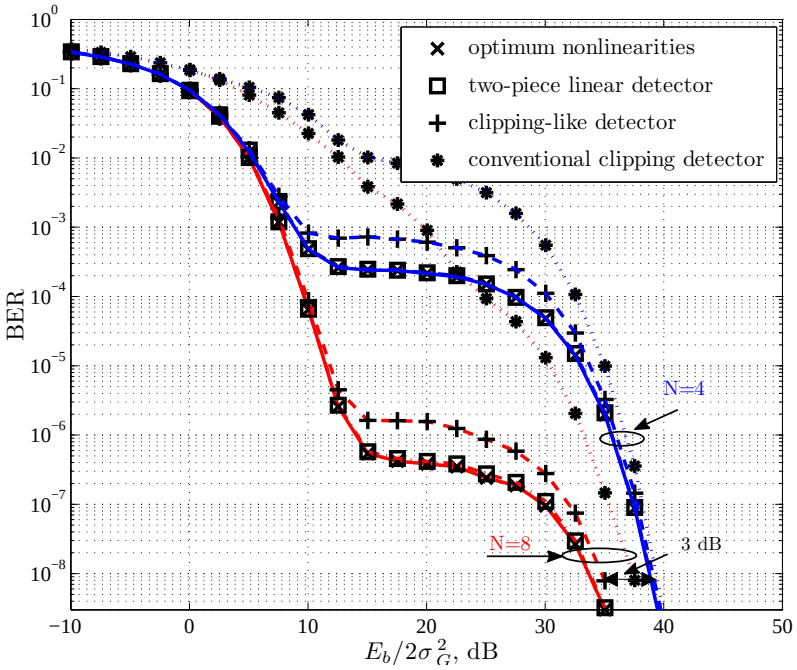

Figure 3.18: Performance comparison in moderate impulse noise for $N = 4$ and 8

3.5 Conclusion

In this chapter, we introduced a closed-form approximation of the optimum detector for binary signals in MCA noise. To derive this analysis, we further simplify the MCA model to a density of a single state (Gaussian or impulsive). Using this approximation, we derived a closed-form expression of the optimum nonlinearities, which explains how the optimum detector treats the effects of impulse noise with respect to different signal levels. We additionally showed that this analysis leads to an accurate approximation of the optimum decision regions for different noise environments. For the suboptimum detector, we explained the behaviors of a locally optimum preprocessor and clipping nonlinearities in canceling the effects of MCA noise. Hence, we proposed a linear approximation of the optimum nonlinearities, which leads to a piecewise linear detector and a clipping-like detector. The simulation results showed that the optimum detector for impulse noise provides significant improvements with increasing the number of received observations, N. To justify these improvements, we investigated the nonlinearity operations of the optimum detector at different values of the SNR. At low SNRs, we showed that the optimum detector reduces to a weighted linear combiner, and hence, the performance approaches the impulse-free limit as N increases. At high SNRs, we assessed the linear operations the optimum detector in impulse noise, which limit the performance improvements to those of a linear detector.

Chapter 4

Diversity Schemes for Impulse Noise Mitigation

In this chapter, we focus on time and space diversity schemes to mitigate the effects of impulse noise in Rayleigh fading channels. First, we consider the optimum combining schemes for time and receive diversity. We assume perfect knowledge of noise states [18], which reduces the optimum detector to a tractable form. Thus, we introduce an upper performance bound of the optimum detectors for time and space diversity techniques. For MIMO systems, we derive an upper bound expression for the pairwise error probability (PEP) of orthogonal space-time block coding (OSTBC) in the presence of spatially dependent impulse noise. To realize the optimum combining schemes, we make use of a threshold detection for estimating noise states of MCA noise. Then, we derive a closed-form approximation of the optimum detectors for different diversity techniques.

4.1 Time-Diversity Scheme

We recall the baseband model (see Fig. 1.4) for time diversity in impulse noise. Since there are N_D time slots, carrying the same transmit signal, the received signal observations are

$$y_{n_D} = \sqrt{\frac{E_b}{N_D}} h_{n_D} s + z_{n_D} \ , \quad n_D = 1, 2, \cdots, N_D \ , \tag{4.1}$$

where $s \in \pm 1$ and h_{n_D} denotes a complex-valued fading coefficient for the n_D^{th} time slot. The fading processes for the N_D channels are assumed to be statistically independent complex-valued Gaussian random processes. In (4.1), we assume that z_{n_D}, $\forall n_D$, represent baseband samples of a complex-valued MCA interference process. The complex-valued

MCA density can be given as

$$p_z(z_{n_D}) = \sum_{m_{n_D}=0}^{\infty} \frac{\alpha_{m_{n_D}}}{2\pi\sigma^2_{m_{n_D}}} \mathrm{e}^{-|z_{n_D}|^2/2\sigma^2_{m_{n_D}}} \ , \tag{4.2}$$

where $\sigma^2_m = \sigma^2_G + \frac{m}{A}\sigma^2_I$. Since $|z_{n_D}|^2 = z^2_{\mathrm{I}n_D} + z^2_{\mathrm{Q}n_D}$, the average variance of a baseband MCA process, $\mathrm{E}\{|z_{n_D}|^2\}$, can be given as

$$\begin{aligned} \mathrm{E}\{|z_{n_D}|^2\} &= 2\sum_{m_{n_D}=0}^{\infty} \alpha_{m_{n_D}} \sigma^2_{m_{n_D}} \ , \\ &= 2\sigma^2 \ , \end{aligned} \tag{4.3}$$

where $\sigma^2 = \sigma^2_G + \sigma^2_I$ denotes the mean variance of the passband MCA process. For statistically independent noise observations, the optimum decision rule is given by

$$\Lambda_{ML} = \log\left(\frac{\prod_{n_D=1}^{N_D} p_z\left(y_{n_D} - \sqrt{\frac{E_b}{N_D}}h_{n_D}\right)}{\prod_{n_D=1}^{N_D} p_z\left(y_{n_D} + \sqrt{\frac{E_b}{N_D}}h_{n_D}\right)}\right) \underset{S_0}{\overset{S_1}{\gtrless}} 0 \ . \tag{4.4}$$

The performance evaluation of (4.4) is mathematically intractable. However, when the noise states $m_{n_D}, \forall n_D$, are known at the receiver, the noise observations, z_{n_D}, can be seen as conditional Gaussian random variables with different variances, $\sigma^2_{m_{n_D}}$. Thus, we have

$$p_z(z_{n_D}|m_{n_D}) = \frac{1}{2\pi\sigma^2_{m_{n_D}}} \mathrm{e}^{-|z_{n_D}|^2/2\sigma^2_{m_{n_D}}} \ . \tag{4.5}$$

Therefore, by substituting (4.5) in (4.4) the optimum detector reduces to a weighted maximum ratio combining as

$$\sum_{n_D=1}^{N_D} \frac{\mathrm{Re}\{h^*_{n_D} y_{n_D}\}}{\sigma^2_{m_{n_D}}} \underset{S_0}{\overset{S_1}{\gtrless}} 0 \ . \tag{4.6}$$

With the above expression assuming perfect knowledge of noise states, it leads to a tractable upper performance bound for the optimum detector in (4.4).

4.1.1 Asymptotic Upper Performance Bound

In this subsection, we use (4.6) to evaluate the performance of the optimum detector. Suppose that the signal $s = +1$ was transmitted, the optimum decision variable, χ_D, can

be expressed as

$$\chi_D = \sqrt{\frac{E_b}{N_D}} \sum_{n_D=1}^{N_D} \frac{|h_{n_D}|^2}{\sigma^2_{m_{n_D}}} + \sum_{n_D=1}^{N_D} \frac{\mathrm{Re}\{h^*_{n_D} z_{n_D}\}}{\sigma^2_{m_{n_D}}} \,. \tag{4.7}$$

For fixed sets of h_{n_D} and m_{n_D}, the decision variable χ_D is Gaussian with mean

$$\mu_{\chi_D} = \sqrt{\frac{E_b}{N_D}} \sum_{n_D=1}^{N_D} \frac{|h_{n_D}|^2}{\sigma^2_{m_{n_D}}} \,, \tag{4.8}$$

and variance

$$\sigma^2_{\chi_D} = \sum_{n_D=1}^{N_D} \frac{|h_{n_D}|^2}{\sigma^2_{m_{n_D}}} \,. \tag{4.9}$$

For binary antipodal signaling, the probability of error is simply the probability that χ_D is less than zero. Hence, the conditional error probability can be computed as

$$\begin{aligned} P_{e|h_{n_D},m_{n_D}} &= \mathrm{Q}\left(\frac{\mu_{\chi_D}}{\sigma_{\chi_D}}\right) \,, \\ &= \mathrm{Q}\left(\sqrt{\frac{E_b}{N_D} \sum_{n_D=1}^{N_D} \frac{|h_{n_D}|^2}{\sigma^2_{m_{n_D}}}}\right) \,, \end{aligned} \tag{4.10}$$

where $\mathrm{Q}(x) = \frac{1}{2}\mathrm{erfc}(\frac{x}{\sqrt{2}})$. Using Chernoff's bound, $\mathrm{Q}(x) \leq \frac{1}{2}\mathrm{e}^{-\frac{x^2}{2}}$, the conditional error probability is upper-bounded as

$$\begin{aligned} P_{e|h_{n_D},m_{n_D}} &\leq \frac{1}{2}\mathrm{e}^{-\frac{E_b}{2N_D}\sum_{n_D=1}^{N_D}\frac{|h_{n_D}|^2}{\sigma^2_{m_{n_D}}}} \,, \\ &\leq \frac{1}{2}\prod_{n_D=1}^{N_D} \mathrm{e}^{-\frac{E_b}{2N_D\sigma^2_{m_{n_D}}}|h_{n_D}|^2} \,. \end{aligned} \tag{4.11}$$

Since the fading envelopes, $|h_{n_D}|$, are i.i.d. Rayleigh distributed random variables, $|h_{n_D}|^2$ has a chi-square distribution with two degrees of freedom as

$$p(|h_{n_D}|^2) = \frac{1}{\bar{h}_{n_D}} \exp\left(-\frac{|h_{n_D}|^2}{\bar{h}_{n_D}}\right) \,, \quad |h_{n_D}|^2 \geq 0 \,, \tag{4.12}$$

where $\bar{h}_{n_D} = \mathrm{E}\{|h_{n_D}|^2\}$ denotes the average power of the channel for the n_D^{th} time slot. By averaging (4.11) over the fading channel statistics, we obtain

$$\begin{aligned} P_{e|m_{n_D}} &= \int_0^\infty P_{e|h_{n_D},m_{n_D}} p\left(|h_{n_D}|^2\right) d|h_{n_D}|^2 \,, \\ &\leq \frac{1}{2} \prod_{n_D=1}^{N_D} \frac{1}{1+\frac{E_b}{2N_D\sigma^2_{m_{n_D}}}} \,. \end{aligned} \tag{4.13}$$

The final step in this derivation is to average $P_{e|m_{n_D}}$ over the noise state probabilities $\alpha_{m_{n_D}}$. Thus, we have

$$P_e \leq \frac{1}{2} \sum_{m_1=0}^{\infty} \alpha_{m_1} \cdots \sum_{m_{N_D}=0}^{\infty} \alpha_{m_{N_D}} \prod_{n_D=1}^{N_D} \frac{1}{1+\frac{E_b}{2N_D\sigma^2_{m_{n_D}}}} \,. \tag{4.14}$$

Since the noise states m_{n_D} are statistically independent over the different time slots, it implies that the upper bound of the error probability can be rewritten as

$$P_e \leq \frac{1}{2} \prod_{n_D=1}^{N_D} \sum_{m_{n_D}=0}^{\infty} \alpha_{m_{n_D}} \frac{1}{1+\frac{E_b}{2N_D\sigma^2_{m_{n_D}}}} \,. \tag{4.15}$$

For high E_b/σ_m^2, the right-hand side of (4.15) can be approximated as

$$P_e < \frac{1}{2} \left(\frac{E_b}{N_D}\right)^{-N_D} \overbrace{\prod_{n_D=1}^{N_D} \sum_{m_{n_D}=0}^{\infty} 2\alpha_{m_{n_D}} \sigma^2_{m_{n_D}}}^{G_D} \,. \tag{4.16}$$

By substituting (4.3) in (4.16), the upper performance bound can be expressed as

$$P_e < \frac{1}{2} \left(\frac{E_b}{2N_D\sigma^2}\right)^{-N_D} \,. \tag{4.17}$$

Since $\sigma^2 = \sigma_G^2 + \sigma_I^2$ and $\sigma_I^2 = \sigma_G^2/\Upsilon$, (4.17) can be written in terms of σ_G^2 as follows:

$$P_e < \frac{1}{2} \left(\frac{E_b}{2N_D\sigma_G^2}\right)^{-N_D} \left(1+\frac{1}{\Upsilon}\right)^{N_D} \,, \tag{4.18}$$

From (4.17) and (4.18), we can indicate two interesting observations regarding the upper performance bound of the optimum detector in fading with impulse noise. First, the performance of the optimum scheme is upper-bounded by those of the optimum detector in Gaussian channels with variance σ^2. Second, at high SNRs, the gap in the SNRs

between the performances of impulse-free channels (Gaussian noise with σ_G^2) and impulse noise channels is given by $\left(1+\frac{1}{\Upsilon}\right)$. We note that the performance gap depends only on Υ. Thus, the optimum detectors in impulse noise with different A and equal Υ yield similar performances at high SNRs.

To confirm these points, we simulated the performances of the optimum detectors with and without noise state information (NSI) for $N_D = 2$ in different MCA environments. First, we illustrate in Fig. 4.1 the performances for impulse noise with different impulsiveness, A. Second, in Fig. 4.2, we simulate the performances for impulse noise with different Gaussian factors, Υ. From these figures, we observe that the optimum detectors, with

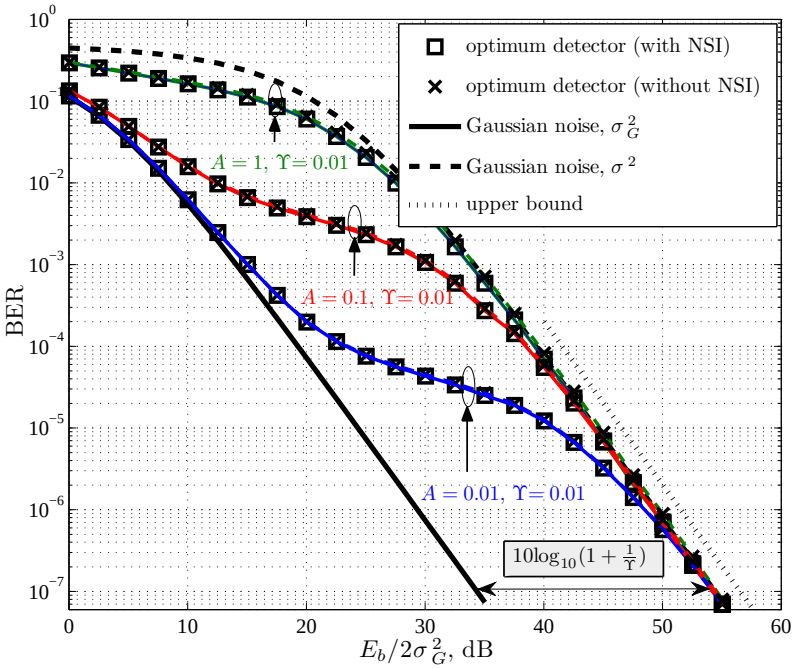

Figure 4.1: BER performances of the optimum detectors for $N_D = 2$ in impulse noise with $\Upsilon = 0.01$ and different A

and without NSI, provide almost the same performances. Thus, the upper performance bound in (4.18) confines the performances of both detectors. In Fig. 4.1, we observe that the performances for impulse noise with $\Upsilon = 0.01$ and different A approach the same upper bound. Hence, at high SNRs, the performances of the optimum detectors approach those of Gaussian noise with variance σ^2, which agrees with (4.17). However, at low values of the SNR, we observe that the performance of the optimum detector approaches those of impulse-free channels (Gaussian noise with σ_G^2) as A decreases. In Fig. 4.2, we confirm the different upper performance bounds of the optimum detector in impulse noise environments with unequal Υ. We observe that the gap in the SNR between the BER performances for impulse-free noise and impulse noise with different Υ is given by $10\log_{10}(1+\frac{1}{\Upsilon})$ dB, which is in agreement with (4.18).

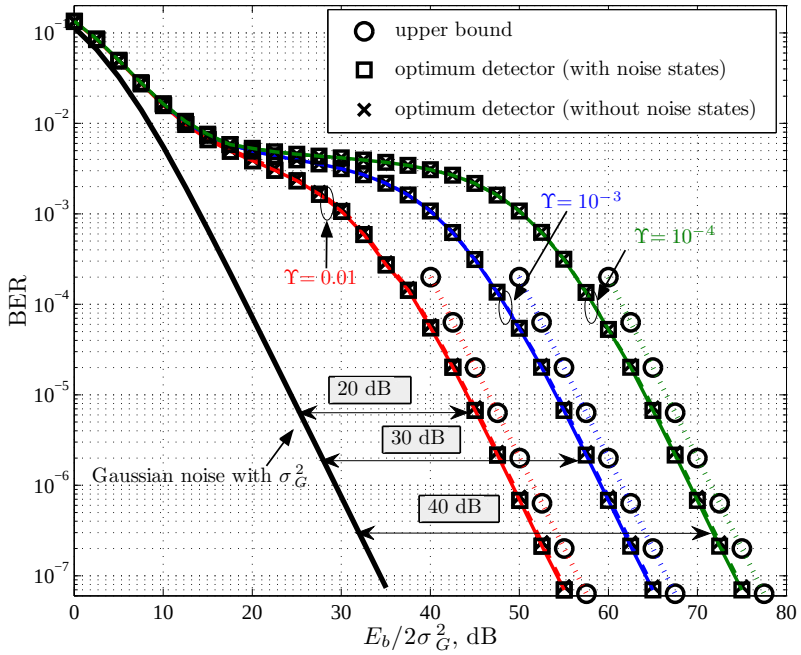

Figure 4.2: BER performances of the optimum detectors for $N_D = 2$ in impulse noise with $A = 0.1$ and different Υ

4.1.2 Nonlinear Diversity Combining

The optimum detector in (4.4) possesses a complex ML decision rule. Although the assumption of perfect noise states reduces the complexity of the optimum detector, it appears to be unrealistic for a practical realization. In the following, we utilize a threshold detection scheme to simplify a nonlinear combining rule. We observe in (3.5) that the threshold d_0, which discriminates Gaussian noise and impulse noise, is equivalent to the ML estimate of the noise state m. Similarly, the estimate of noise states, m_{n_D}, $n_D = 1, \cdots, N_D$ for the complex-value MCA model can be given as

$$\tilde{m}_{n_D} = \begin{cases} 0 & \text{if } |z_{n_D}|^2 \leq d_1^2\,, \\ 1 & \text{otherwise}\,, \end{cases} \tag{4.19}$$

where $d_1 = \sqrt{\frac{2\sigma_0^2\sigma_1^2}{\sigma_1^2-\sigma_0^2}\log\frac{\alpha_0\sigma_1^2}{\alpha_1\sigma_0^2}}$ denotes the threshold, which inspects the state of complex-valued MCA noise. The threshold equation, $|z_{n_D}|^2 = d_1^2$, in the complex plane, can be seen as a circle of radius d_1. The inner and outer regions of this circle (see Fig. 4.3) are corresponding to the Gaussian and impulsive states, respectively. Consequently, the

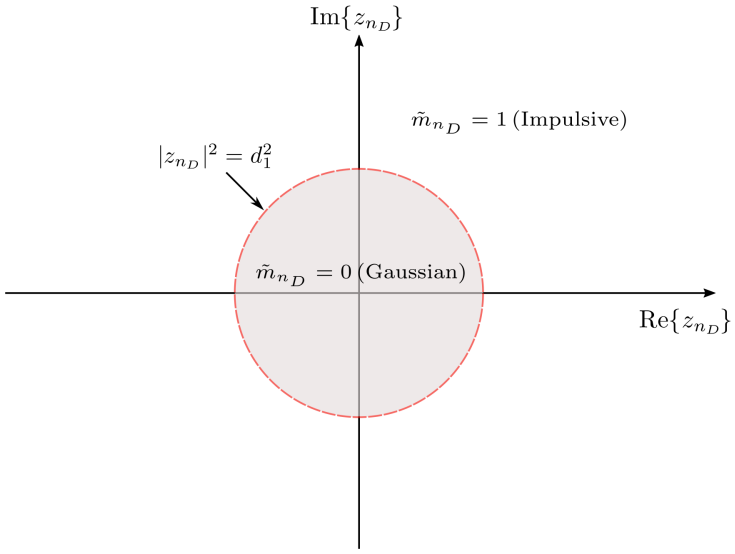

Figure 4.3: The noise state estimation in the complex plane

complex-valued MCA density can be reduced to

$$p_z(z_{n_D}) \approx \begin{cases} \frac{\alpha_0}{2\pi\sigma_0^2} e^{-\frac{|z_{n_D}|^2}{2\sigma_0^2}} & \text{if } |z_{n_D}|^2 \leq d_1^2 \ , \\ \frac{\alpha_1}{2\pi\sigma_1^2} e^{-\frac{|z_{n_D}|^2}{2\sigma_1^2}} & \text{otherwise} \ . \end{cases} \tag{4.20}$$

Under the hypotheses S_1 and S_0, the likelihood functions $p_z(y_{n_D} - \sqrt{\frac{E_b}{N_D}} h_{n_D} s)$ can be represented as

$$p_z(y_{n_D} - \sqrt{\tfrac{E_b}{N_D}} h_{n_D} s) \approx \begin{cases} \frac{\alpha_0}{2\pi\sigma_0^2} e^{-\frac{\left|y_{n_D} - \sqrt{\frac{E_b}{N_D}} h_{n_D} s\right|^2}{2\sigma_0^2}} & \text{if } \left|y_{n_D} - \sqrt{\tfrac{E_b}{N_D}} h_{n_D} s\right|^2 \leq d_1^2 \ , \\ \frac{\alpha_1}{2\pi\sigma_1^2} e^{-\frac{\left|y_{n_D} - \sqrt{\frac{E_b}{N_D}} h_{n_D} s\right|^2}{2\sigma_1^2}} & \text{otherwise} \ . \end{cases} \tag{4.21}$$

The above representation classifies the complex plane of the received signal observation, y_{n_D}, into 3 or 4 different regions. Figure (4.4) illustrates the 4 possible regions in the complex plane. We observe that the threshold boundary equation, $\left|y_{n_D} - \sqrt{\frac{E_b}{N_D}} h_{n_D} s\right|^2 = d_1^2$, for $s \in \{+1, -1\}$, depicts a circle centered at $\left(\sqrt{\frac{E_b}{N_D}} \text{Re}\{h_{n_D}\} s, \sqrt{\frac{E_b}{N_D}} \text{Im}\{h_{n_D}\} s\right)$. Thus, we may have either 3 or 4 overlapping regions depending on the values of the signal level and fading coefficients. The shown figure depicts the 4 overlapping regions C_0, C_1, C_2, and C_3. For each region, we substitute the corresponding term of (4.21) into (4.4) to

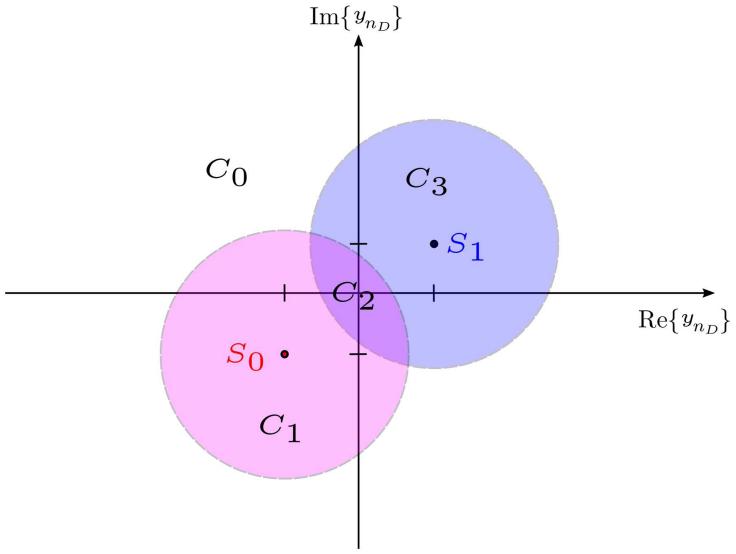

Figure 4.4: Overlapping regions of the received observation for hypotheses S_1 and S_0

approximate the optimum detector as

$$\Lambda_{ML} = \sum_{n_D=1}^{N_D} g(y_{n_D}, h_{n_D}) \underset{S_0}{\overset{S_1}{\gtrless}} 0 \ , \tag{4.22}$$

where

$$g(y_{n_D},\ h_{n_D}) \approx 2\sqrt{\tfrac{E_b}{N_D}} \frac{\mathrm{Re}\{h_{n_D}^* y_{n_D}\}}{\sigma_1^2} \ , \tag{4.23}$$

$$g(y_{n_D},\ h_{n_D}) \approx -\tfrac{\sigma_1^2-\sigma_0^2}{2\sigma_1^2\sigma_0^2} \left(d_1^2 - (|y_{n_D}|^2 + 2\sqrt{\tfrac{E_b}{N_D}} \tfrac{\sigma_1^2+\sigma_0^2}{\sigma_1^2-\sigma_0^2} \mathrm{Re}\{h_{n_D}^* y_{n_D}\} + 2\tfrac{E_b}{N_D}|h_{n_D}|^2) \right) \ , \tag{4.24}$$

$$g(y_{n_D},\ h_{n_D}) \approx 2\sqrt{\tfrac{E_b}{N_D}} \frac{\mathrm{Re}\{h_{n_D}^* y_{n_D}\}}{\sigma_0^2} \ , \tag{4.25}$$

and

$$g(y_{n_D},\ h_{n_D}) \approx \tfrac{\sigma_1^2-\sigma_0^2}{2\sigma_1^2\sigma_0^2} \left(d_1^2 - (|y_{n_D}|^2 - 2\sqrt{\tfrac{E_b}{N_D}} \tfrac{\sigma_1^2+\sigma_0^2}{\sigma_1^2-\sigma_0^2} \mathrm{Re}\{h_{n_D}^* y_{n_D}\} + 2\tfrac{E_b}{N_D}|h_{n_D}|^2) \right) \ , \tag{4.26}$$

are the approximate nonlinearities of the optimum combining for the regions C_0, C_1, C_2, and C_3, respectively. In Fig. 4.5, we depict the approximate nonlinearities of all regions for a fixed value of h_{n_D}. We observe that the approximate combining nonlinearities behave similarly to those of the optimum detector considered in Section 3.1. However, we note that the approximate combining nonlinearities scale the received observations according to the fading coefficients and noise variances. To assess the performance of this approximation, we simulated the BER performances of the nonlinear combining scheme and the optimum detector utilizing different numbers of time slots, N_D. Figure 4.6

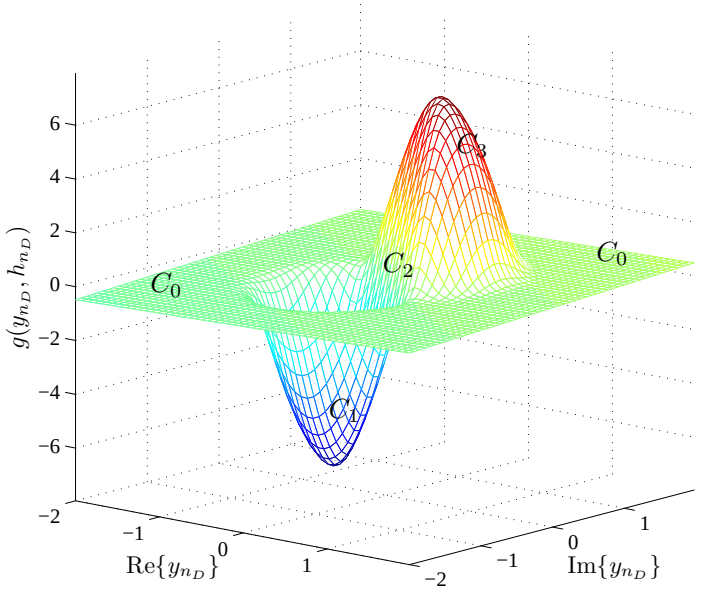

Figure 4.5: Combining nonlinearities in fading channels with complex-valued MCA noise

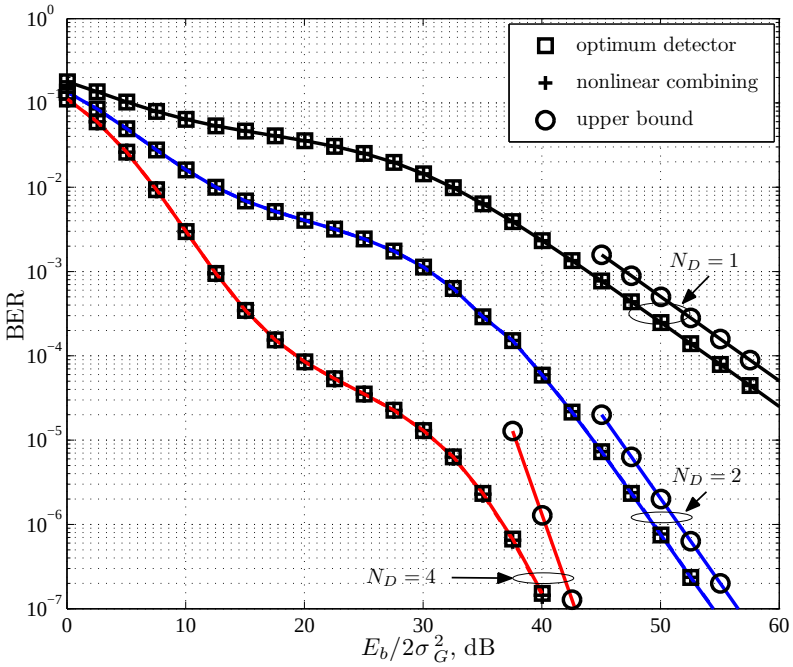

Figure 4.6: Performance comparison of the nonlinear combining scheme with the optimum detector in impulse noise with $A = 0.1$ and $\Upsilon = 0.01$

illustrates the BER performance versus the SNR for $N_D = 1,\ 2$, and 4. We observe that the performance of the nonlinear combining scheme approaches those of the optimum detector for different N_D. In addition, we note that the performances of both schemes are improved considerably when N_D increases, which complies with the upper performance bound at different numbers of diversity channels, N_D.

4.2 Spatial Diversity Reception

In this section, we consider the performance evaluation of the optimum receiver for spatial (receive) diversity in combating the effects of fading and impulse noise. Thus, we assume a communication system with N_R receive antennas operating in impulse noise environments. For binary signals, the baseband received observations for the N_R receive antennas can be given as

$$y_{n_R} = \sqrt{E_b} h_{n_R} s + z_{n_R}\ , \quad n_R = 1, 2, \cdots, N_R\ , \tag{4.27}$$

where $s \in \pm 1$ and h_{n_R}, $n_R = 1, \cdots, N_R$, are statistically independent complex-valued fading coefficients along the N_R diversity channels. The noise observations, z_{n_R}, denote spatially correlated baseband noise samples at the N_R receive antennas. Form the passband multivariate MCA model in (2.20), the baseband noise observations can be modeled as

$$p_{\mathbf{z}}(\mathbf{z}) = \sum_{m=0}^{\infty} \frac{\alpha_m}{(2\pi)^{N_R} |\mathbf{\Sigma}_m|} \mathrm{e}^{-\frac{1}{2}\mathbf{z}^H \mathbf{\Sigma}_m{}^{-1} \mathbf{z}}\ . \tag{4.28}$$

where $\mathbf{z} = [z_1, \cdots, z_{N_R}]^T$ and the covariance matrix, $\mathbf{\Sigma}_m$, is given as

$$\mathbf{\Sigma}_m = \begin{pmatrix} \sigma^2_{m,1} & \cdots & \rho_{m,1N_R}\sigma_{m,1}\sigma_{m,N_R} \\ \vdots & \ddots & \vdots \\ \rho_{m,N_R1}\sigma_{m,N_R}\sigma_{m,1} & \cdots & \sigma^2_{m,N_R} \end{pmatrix}\ , \tag{4.29}$$

where $\sigma^2_{m,n_R} = \sigma^2_G \left(1 + \frac{m}{A\Upsilon_{n_R}}\right)$, $n_R = 1, \cdots, N_R$, and $\rho_{m,n_R\grave{n}_R}$ denote the correlation coefficients of noise observations at the n_R^{th} and $\grave{n}_R^{\text{th}}$ receive antennas. Since $\Upsilon_{n_R} \neq \Upsilon$, $\forall n_R$, this implies that impulse noise for different antennas possess unequal variances $\sigma^2_{n_R} = \sigma^2_G + \frac{\sigma^2_G}{\Upsilon_{n_R}}$. Based on the received observation vector, $\mathbf{y} = [y_1, \cdots, y_{N_R}]^T$, the optimum detector computes the following LLR

$$\Lambda_{ML} = \log\left(\frac{p_{\mathbf{z}}(\mathbf{y} - \sqrt{E_b}\mathbf{h})}{p_{\mathbf{z}}(\mathbf{y} + \sqrt{E_b}\mathbf{h})}\right) \underset{S_0}{\overset{S_1}{\gtrless}} 0\ , \tag{4.30}$$

Since (4.30) does not allow a simplification, we again assume that the NSI is available at the receiver. Then, when m is known, the distribution of $\mathbf{z}$ reduces to a conditional multivariate Gaussian density as

$$p_{\mathbf{z}}(\mathbf{z}|m) = \frac{1}{(2\pi)^{N_R}|\mathbf{\Sigma}_m|} \mathrm{e}^{-\frac{1}{2}\mathbf{z}^H \mathbf{\Sigma}_m{}^{-1}\mathbf{z}} . \tag{4.31}$$

By substituting (4.31) in (4.30), the optimum detector reduces to

$$\mathrm{Re}\{\mathbf{h}^H \mathbf{\Sigma}_m^{-1}\mathbf{y}\} \underset{S_0}{\overset{S_1}{\gtrless}} 0 . \tag{4.32}$$

The above expression leads to a tractable analysis of the upper performance bound for the optimum detector in spatially correlated impulse noise.

4.2.1 Asymptotic Upper Performance Bound

From (4.32) and (4.27), supposing that the signal $s = +1$ was transmitted, the optimum decision variable, χ_R, can be expressed as

$$\chi_R = \sqrt{E_b}\mathbf{h}^H \mathbf{\Sigma}_m^{-1}\mathbf{h} + \mathrm{Re}\left\{\mathbf{h}^H \mathbf{\Sigma}_m^{-1}\mathbf{z}\right\} . \tag{4.33}$$

For fixed sets of m and $\mathbf{h}$, the decision variable χ_R is Gaussian with mean $\mu_{\chi_R} = \sqrt{E_b}\mathbf{h}^H \mathbf{\Sigma}_m^{-1}\mathbf{h}$ and variance $\sigma^2_{\chi_R} = \mathbf{h}^H \mathbf{\Sigma}_m^{-1}\mathbf{h}$. Similar to (4.10), the conditional error probability can be given as

$$P_{e|\mathbf{h},m} = \mathrm{Q}\left(\sqrt{E_b \mathbf{h}^H \mathbf{\Sigma}_m^{-1}\mathbf{h}}\right) . \tag{4.34}$$

Then, the Chernoff bound leads to

$$P_{e|\mathbf{h},m} \leq \frac{1}{2}\mathrm{e}^{-\frac{E_b}{2}\mathbf{h}^H \mathbf{\Sigma}_m^{-1}\mathbf{h}} . \tag{4.35}$$

Since $\mathbf{\Sigma}_m^{-1}$ is symmetric, we can write $\mathbf{\Sigma}_m^{-1} = \mathbf{U}\mathbf{\Lambda}_m\mathbf{U}^H$, where $\mathbf{U}$ is a unitary matrix and $\mathbf{\Lambda}_m$ is a diagonal matrix. Thus, we have

$$\begin{aligned} \mathbf{h}^H \mathbf{\Sigma}_m^{-1}\mathbf{h} &= \boldsymbol{\hbar}^H \mathbf{\Lambda}_m \boldsymbol{\hbar} , \\ &= \sum_{n_R=1}^{N_R} \zeta_{m,n_R} |\hbar_{n_R}|^2 , \end{aligned} \tag{4.36}$$

where $\boldsymbol{\hbar} = \mathbf{U}^H\mathbf{h}$ and ζ_{m,n_R}, $\forall n_R$, are the diagonal elements of $\boldsymbol{\Lambda}_m$, which stand for the eigenvalues of $\boldsymbol{\Sigma}_m^{-1}$. By substituting (4.36) into (4.35), the upper bound of the conditional error probability can be rewritten as

$$P_{e|\mathbf{h},m} \leq \frac{1}{2}\prod_{n_R=1}^{N_R} \mathrm{e}^{-\frac{E_b}{2}\zeta_{m,n_R}|\hbar_{n_R}|^2} \ . \tag{4.37}$$

The last two steps are to average $P_{e|\mathbf{h},m}$ over the statistics of $|\hbar_{n_R}|$ and m. Since $\mathbf{U}$ is a unitary matrix, $|\hbar_{n_R}|$ follows the same statistics of the channel coefficient $|h_{n_R}|$. Similar to (4.13), averaging $P_{e|\mathbf{h},m}$ over the statistics of $|\hbar_{n_R}|^2$ yields

$$P_{e|m} \leq \frac{1}{2}\prod_{n_R=1}^{N_R} \frac{1}{1+\frac{E_b}{2}\zeta_{m,n_R}} \ . \tag{4.38}$$

Therefore, the upper bound of the error probability can be given as

$$P_e \leq \frac{1}{2}\sum_{m=0}^{\infty}\alpha_m \prod_{n_R=1}^{N_R} \frac{1}{1+\frac{E_b}{2}\zeta_{m,n_R}} \ . \tag{4.39}$$

For high signal levels, the right hand side of (4.39) can be approximated as

$$P_e < \frac{1}{2}\left(\frac{E_b}{2}\right)^{-N_R} \overbrace{\sum_{m=0}^{\infty}\alpha_m \prod_{n_R=1}^{N_R} \frac{1}{\zeta_{m,n_R}}}^{G_R} \ . \tag{4.40}$$

To investigate how the optimum detector should behave in different impulse noise environments, we consider spatial diversity with two receive antennas ($N_R = 2$). Therefore, the covariance matrix $\boldsymbol{\Sigma}_m$ can be given as

$$\boldsymbol{\Sigma}_m = \begin{pmatrix} \sigma_{m,1}^2 & \rho_m\sigma_{m,1}\sigma_{m,2} \\ \rho_m\sigma_{m,2}\sigma_{m,1} & \sigma_{m,2}^2 \end{pmatrix} \ . \tag{4.41}$$

The eigenvalues of $\boldsymbol{\Sigma}_m^{-1}$ can be computed as follow:

$$\begin{aligned} \zeta_{m,1} &= \frac{\sigma_{m,1}^2 + \sigma_{m,2}^2 + \sqrt{(\sigma_{m,1}^2 - \sigma_{m,2}^2)^2 + 4\sigma_{m,1}^2\sigma_{m,2}^2{\rho_m}^2}}{2\sigma_{m,1}^2\sigma_{m,2}^2(1-{\rho_m}^2)} \ , \\ \zeta_{m,2} &= \frac{\sigma_{m,1}^2 + \sigma_{m,2}^2 - \sqrt{(\sigma_{m,1}^2 - \sigma_{m,2}^2)^2 + 4\sigma_{m,1}^2\sigma_{m,2}^2{\rho_m}^2}}{2\sigma_{m,1}^2\sigma_{m,2}^2(1-{\rho_m}^2)} \ . \end{aligned} \tag{4.42}$$

By substituting (4.42) in (4.40), the term G_R can be written as

$$\begin{aligned} G_R &= \sum_{m=0}^{\infty} \alpha_m \sigma_{m,1}^2 \sigma_{m,2}^2 (1-\rho_m^2) \ , \\ &= \mathrm{E}_m\{\sigma_{m,1}^2 \sigma_{m,2}^2 (1-\rho_m^2)\} \ , \end{aligned} \tag{4.43}$$

where $\mathrm{E}_m\{\cdot\}$ denotes the expectation with respect to the noise state m. For simplicity, we assume that $\rho_m = \rho$, $\forall m$. Since $\sigma_{m,n_R}^2 = \sigma_G \left(1 + \frac{m}{A\Upsilon_{n_R}}\right)$, $\forall n_R$, G_R can be evaluated as

$$G_R = (\sigma_G^2)^2 (1-\rho^2) \left(1 + \frac{1}{\Upsilon_1}\right) \left(1 + \frac{1}{\Upsilon_2}\right) \left(1 + \frac{1}{A(1+\Upsilon_1)(1+\Upsilon_2)}\right) \ . \tag{4.44}$$

By substituting (4.44) in (4.40), the upper performance bound of the optimum detector for 2-antenna systems can be expressed as

$$P_e < \frac{1}{2} \left(\frac{E_b}{2\sigma_G^2}\right)^{-2} (1-\rho^2) \left(1 + \frac{1}{\Upsilon_1}\right) \left(1 + \frac{1}{\Upsilon_2}\right) \left(1 + \frac{1}{A(1+\Upsilon_1)(1+\Upsilon_2)}\right) \ . \tag{4.45}$$

In (4.45), we note that the first term, $\frac{1}{2}\left(\frac{E_b}{2\sigma_G^2}\right)^{-2}$, denotes the exact upper performance bound for Gaussian noise with variance σ_G^2 (impulse-free noise). Therefore, the last four terms can determine the performance gap between the impulse-free channels and spatially correlated MCA noise. According to (4.45), we observe that the performance gap depends on the impulsive index, A, and noise correlation, ρ. The term $(1-\rho^2)$ indicates how the performance gap decreases as ρ increases. However, the term $\left(1 + \frac{1}{A(1+\Upsilon_1)(1+\Upsilon_2)}\right)$ shows how the performance gap increases as A decreases. This differs from the upper performance bound of the optimum detector for time diversity, which is independent on A.

To confirm the above expression, we simulate the performance of the optimum detectors (with and without NSI) for $N_R = 2$ in different impulse noise environments. We limit the simulation environments to impulse noise with equal Gaussian factors, $\Upsilon_{n_R} = \Upsilon$, $\forall n_R$. Thus, the expression in (4.45) can be rewritten as

$$P_e < \frac{1}{2} \left(\frac{E_b}{2\sigma_G^2}\right)^{-2} (1-\rho^2) \left(1 + \frac{1}{\Upsilon}\right)^2 \left(1 + \frac{1}{A(1+\Upsilon)^2}\right) \ , \tag{4.46}$$

which can be expressed in terms of σ^2 as

$$P_e < \frac{1}{2} \left(\frac{E_b}{2\sigma^2}\right)^{-2} (1-\rho^2) \left(1 + \frac{1}{A(1+\Upsilon)^2}\right) \ . \tag{4.47}$$

In Fig. 4.7, we depict the performances of the optimum detectors in spatially uncorrelated impulse noise with different A and $\Upsilon = 0.01$. Additionally, we depict the performances of

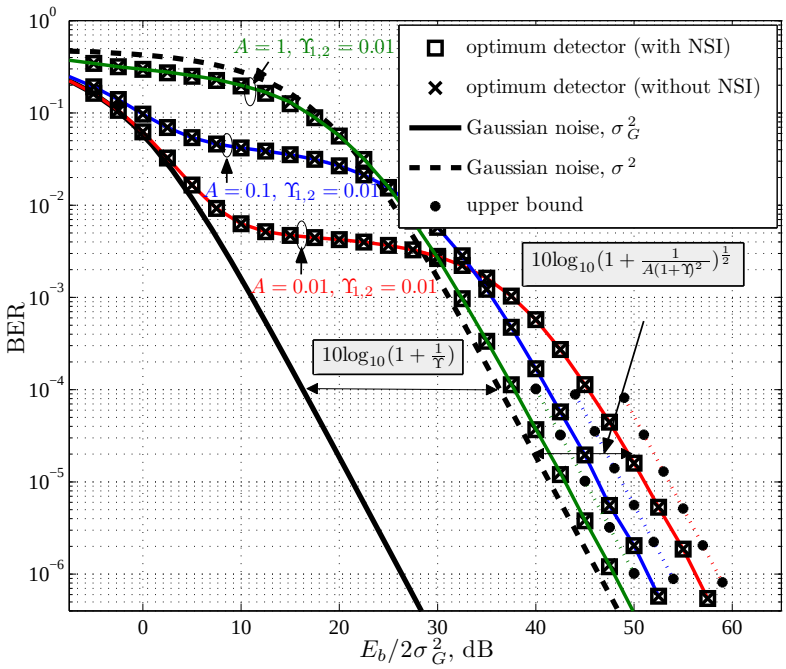

Figure 4.7: BER performances of the optimum detectors in impulse noise with $\Upsilon_{1,2} = 0.01$ and different A for $N_R = 2$

Gaussian noise with variances σ_G^2 and σ^2 as references. First, we observe that the optimum detectors with and without NSI provide identical performances. Second, we note that the expression in (4.46) provides a tight upper performance bound to both detectors. Third, we see clearly that, at high SNRs, the performance of the optimum detector in impulse noise degrades as the impulsive index A decreases. Therefore, we note that the gap in the SNR between the performances of the optimum detectors for impulse noise and Gaussian noise is in accordance with (4.47). To confirm the performance of the optimum detector in spatially correlated impulse noise, we simulate the BER versus ρ at $E_b/2\sigma_G^2 = 50$ dB for different values of A as illustrated in Fig. 4.8. In this figure, we show how the performance improves a ρ increases, which is consistent with (4.47). Furthermore, we observe that the performance loss of the optimum detector due to impulse noise increases inversely with respect to A, which is in agreement with the last term of (4.47)

4.2.2 Spatial Diversity Combining

We investigate the noise state estimate of multivariate MCA noise, which realizes the optimum decision rule in a closed-form approximation. Herewith, we start with the 2-

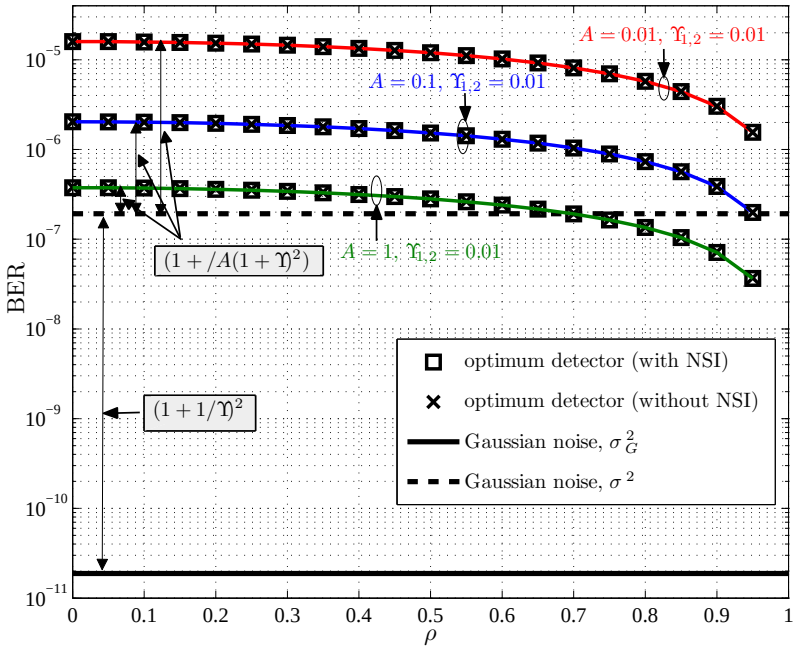

Figure 4.8: BER performances of the optimum detectors versus ρ for different A and $\Upsilon_{1,2} = 0.01$ at an SNR=50 dB

term approximation of the multivariate MCA noise, which can be expressed as

$$p_{\mathbf{z}}(\mathbf{z}) \approx \frac{\alpha_0}{(2\pi)^{N_R}|\mathbf{\Sigma}_0|} \mathrm{e}^{-\frac{1}{2}\mathbf{z}^H \mathbf{\Sigma}_0^{-1}\mathbf{z}} + \frac{\alpha_1}{(2\pi)^{N_R}|\mathbf{\Sigma}_1|} \mathrm{e}^{-\frac{1}{2}\mathbf{z}^H \mathbf{\Sigma}_1^{-1}\mathbf{z}} \,. \tag{4.48}$$

Similar to (4.20), the multivariate MCA model can be further approximated as

$$p_{\mathbf{z}}(\mathbf{z}) \approx \begin{cases} \frac{\alpha_0}{(2\pi)^{N_R}|\mathbf{\Sigma}_0|} \mathrm{e}^{-\frac{1}{2}\mathbf{z}^H \mathbf{\Sigma}_0^{-1}\mathbf{z}} & \text{if } \overbrace{\mathbf{z}^H \mathbf{M} \mathbf{z}}^{\tilde{m}=0} \leq d_2 \,, \\ \frac{\alpha_1}{(2\pi)^{N_R}|\mathbf{\Sigma}_1|} \mathrm{e}^{-\frac{1}{2}\mathbf{z}^H \mathbf{\Sigma}_1^{-1}\mathbf{z}} & \text{if } \overbrace{\mathbf{z}^H \mathbf{M} \mathbf{z}}^{\tilde{m}=1} > d_2 \,, \end{cases} \tag{4.49}$$

where $\mathbf{M} = \mathbf{\Sigma}_0^{-1} - \mathbf{\Sigma}_1^{-1}$ and $d_2 = 2\log\left(\frac{\alpha_0|\mathbf{\Sigma}_1|}{\alpha_1|\mathbf{\Sigma}_0|}\right)$. From (4.49), we note that the elements of $\mathbf{z}$ are subject to interference of identical noise states, $\tilde{m}$. From (4.49) and (4.27), suppose the signal s was sent, the NSI can be extracted from the received signal vector, $\mathbf{y}$, as follows:

$$\tilde{m}_{\mathbf{y}|s} = \begin{cases} 0 & \text{if } \left(\mathbf{y} - \sqrt{E_b} s\mathbf{h}\right)^H \mathbf{M} \left(\mathbf{y} - \sqrt{E_b} s\mathbf{h}\right) \leq d_2 \,, \\ 1 & \text{otherwise} \,, \end{cases} \tag{4.50}$$

where $\tilde{m}_{\mathbf{y}|s=+1}$ and $\tilde{m}_{\mathbf{y}|s=-1}$ are the noise state estimates under hypotheses S_1 and S_0, respectively. Thus, the likelihood functions $p_{\mathbf{z}}(\mathbf{y} - \sqrt{E_b}\mathbf{h})$ and $p_{\mathbf{z}}(\mathbf{y} + \sqrt{E_b}\mathbf{h})$ can be given

as

$$p_{\mathbf{z}}(\mathbf{y}-\sqrt{E_b}\mathbf{h}) \approx \begin{cases} \frac{\alpha_0}{(2\pi)^{N_R}|\mathbf{\Sigma}_0|}\mathrm{e}^{-\frac{1}{2}(\mathbf{y}-\sqrt{E_b}\mathbf{h})^H\mathbf{\Sigma}_0^{-1}(\mathbf{y}-\sqrt{E_b}\mathbf{h})} & \text{if } \tilde{m}_{\mathbf{y}|+1}=0\ , \\ \frac{\alpha_1}{(2\pi)^{N_R}|\mathbf{\Sigma}_1|}\mathrm{e}^{-\frac{1}{2}(\mathbf{y}-\sqrt{E_b}\mathbf{h})^H\mathbf{\Sigma}_1^{-1}(\mathbf{y}-\sqrt{E_b}\mathbf{h})} & \text{otherwise}\ , \end{cases} \tag{4.51}$$

and

$$p_{\mathbf{z}}(\mathbf{y}+\sqrt{E_b}\mathbf{h}) \approx \begin{cases} \frac{\alpha_0}{(2\pi)^{N_R}|\mathbf{\Sigma}_0|}\mathrm{e}^{-\frac{1}{2}(\mathbf{y}+\sqrt{E_b}\mathbf{h})^H\mathbf{\Sigma}_0^{-1}(\mathbf{y}-\sqrt{E_b}\mathbf{h})} & \text{if } \tilde{m}_{\mathbf{y}|-1}=0\ , \\ \frac{\alpha_1}{(2\pi)^{N_R}|\mathbf{\Sigma}_1|}\mathrm{e}^{-\frac{1}{2}(\mathbf{y}+\sqrt{E_b}\mathbf{h})^H\mathbf{\Sigma}_1^{-1}(\mathbf{y}-\sqrt{E_b}\mathbf{h})} & \text{otherwise}\ , \end{cases} \tag{4.52}$$

respectively. The above approximation divides the optimum decision rule in (4.30) into four decision rules. For $\tilde{m}_{\mathbf{y}|+1}=1$ and $\tilde{m}_{\mathbf{y}|-1}=1$, the estimate of the NSI is impulsive for both hypotheses. Hence, substituting (4.51) and (4.52) in (4.30) leads to

$$\mathrm{Re}\{\mathbf{h}^H\mathbf{\Sigma}_1^{-1}\mathbf{y}\} \underset{S_0}{\overset{S_1}{\gtrless}} 0\ . \tag{4.53}$$

The decision rule for $\tilde{m}_{\mathbf{y}|+1}=0$ and $\tilde{m}_{\mathbf{y}|-1}=0$ can be expressed as

$$\mathrm{Re}\{\mathbf{h}^H\mathbf{\Sigma}_0^{-1}\mathbf{y}\} \underset{S_0}{\overset{S_1}{\gtrless}} 0\ . \tag{4.54}$$

For $\tilde{m}_{\mathbf{y}|+1}=1$ and $\tilde{m}_{\mathbf{y}|-1}=0$, the decision rule is

$$\left(\mathbf{y}+\sqrt{E_b}\mathbf{h}\right)^H\mathbf{M}\left(\mathbf{y}+\sqrt{E_b}\mathbf{h}\right)+4\sqrt{E_b}\mathrm{Re}\left\{\mathbf{h}^H\mathbf{\Sigma}_1^{-1}\mathbf{y}\right\}-d_2 \underset{S_0}{\overset{S_1}{\gtrless}} 0\ . \tag{4.55}$$

Finally, the decision rule for $\tilde{m}_{\mathbf{y}|+1}=0$ and $\tilde{m}_{\mathbf{y}|-1}=1$ leads to

$$\left(\mathbf{y}-\sqrt{E_b}\mathbf{h}\right)^H\mathbf{M}\left(\mathbf{y}-\sqrt{E_b}\mathbf{h}\right)-4\sqrt{E_b}\mathrm{Re}\left\{\mathbf{h}^H\mathbf{\Sigma}_1^{-1}\mathbf{y}\right\}-d_2 \underset{S_1}{\overset{S_0}{\gtrless}} 0\ . \tag{4.56}$$

To confirm the above analysis, we consider spatial diversity with $N_R=2$. Therefore, the threshold boundary equation, $\left(\mathbf{y}-\sqrt{E_b}s\mathbf{h}\right)^H\mathbf{M}\left(\mathbf{y}-\sqrt{E_b}s\mathbf{h}\right)=d_2$, reduces to a general ellipse equation in the complex N_R-dimensional space. However, for two-receive antennas $N_R=2$, assuming real-valued $\mathbf{hy}$ and $\mathbf{h}$, the threshold boundary equation depicts a rotated ellipse regarding the spatial dimensions. Figure 4.9 illustrates the threshold boundary equations in a two-dimensional space for hypotheses S_1 and S_0. Under both hypotheses, the ellipses are centered at $\left(+\sqrt{E_b}h_1,\,+\sqrt{E_b}h_2\right)$ and $\left(-\sqrt{E_b}h_1,\,-\sqrt{E_b}h_2\right)$, respectively. The inner and outer regions of each ellipse are corresponding to $\tilde{m}_{\mathbf{y}|s}=0$ and $\tilde{m}_{\mathbf{y}|s}=1$, respectively. Therefore, the spatial space can be divided into four decision regions D_0, D_1, D_2, and D_3 as illustrated in Fig 4.9. The decision rules for the regions D_0 and D_2 lead to (4.53) and (4.54), respectively. However, the decision rules for the regions

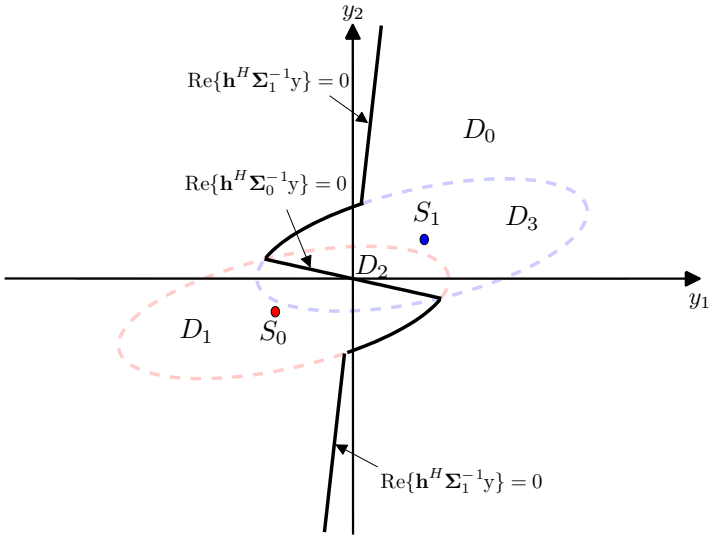

Figure 4.9: Decision boundaries for spatially coupled impulse noise

D_1 and D_3 result in (4.55) and (4.56), respectively. To investigate the decision boundaries of the optimum detector in spatially uncorrelated impulse noise, we assume MCA noise with $\Upsilon_{n_R} = \Upsilon$, $\forall n_R$, and $\rho_m = 0$. Thus, the covariance matrix $\boldsymbol{\Sigma}_m$ reduces to $\sigma_m^2\mathbf{I}_{N_R}$. Consequently, the threshold boundary equations reduce to $|\left(\mathbf{y} - \sqrt{E_b}s\mathbf{h}\right)|^2 = \frac{\sigma_0^2\sigma_1^2}{\sigma_1^2-\sigma_0^2}d_2$,

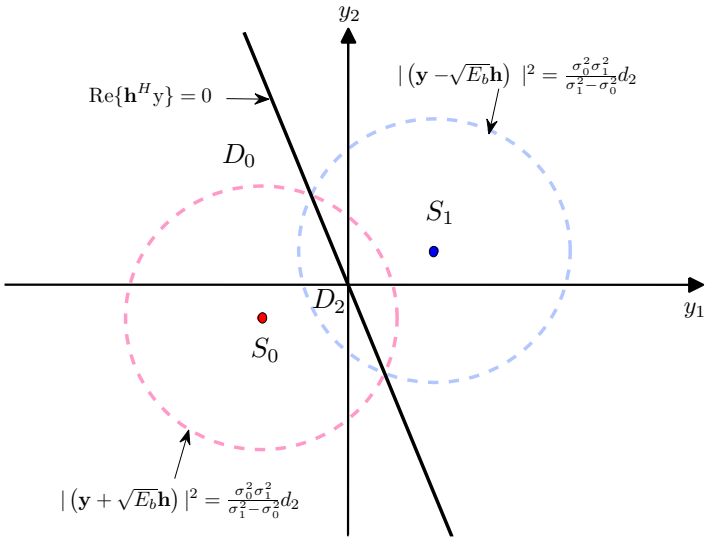

Figure 4.10: Decision regions for spatially uncorrelated impulse noise

which depict circles centered at $\left(\sqrt{E_b}sh_1, \sqrt{E_b}sh_2\right)$ in the 2-dimensional space. Figure 4.10 depicts the threshold boundary equations for hypotheses S_1 and S_0. We observe that the decision boundaries are confined only to regions D_0 and D_2. Since $\boldsymbol{\Sigma}_m^{-1} = \frac{1}{\sigma_m^2}\mathbf{I}$,

the decision rules in (4.53) and (4.54) reduce to

$$\mathrm{Re}\{\mathbf{h}^H\mathbf{y}\} \underset{S_0}{\overset{S_1}{\gtrless}} 0 \,, \tag{4.57}$$

which represents the optimum combining scheme for Gaussian noise. The above expression can justify why the conventional MRC provides the same performance of the optimum detector in the case of spatially uncorrelated impulse noise. In Fig. 4.11, we investigate the performances of the optimum detector and MRC in uncorrelated MCA noise with $A = 0.1$ and $\Upsilon = 0.01$. From this figure, we observe that both detectors offer the same performance for different numbers of receive antennas N_R, which is in line with the above analysis.

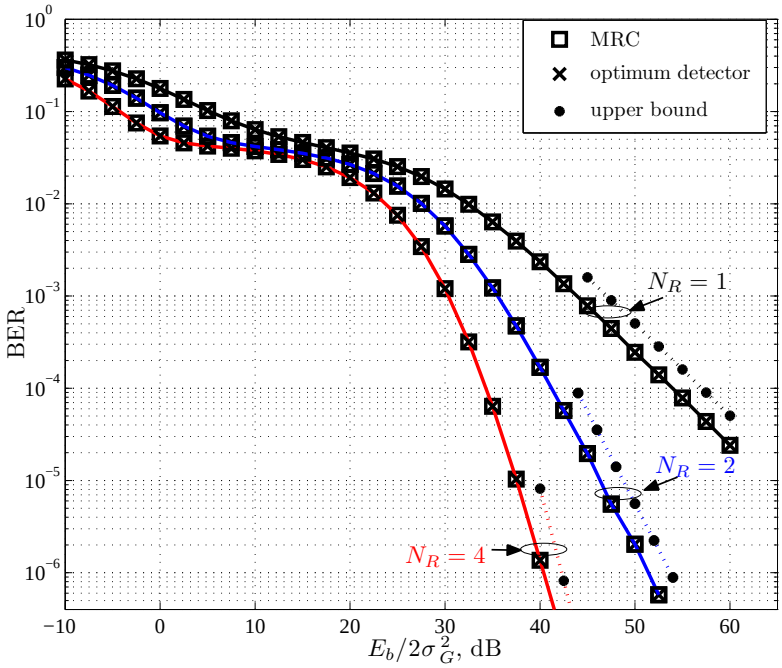

Figure 4.11: BER performances of the optimum detector and MRC in impulse noise with $A = 0.1$ and $\Upsilon = 0.01$ for different N_R

4.3 Space-Time Coding

We conclude this chapter with the performance evaluation of orthogonal ST block coding (OSTBC) in the presence of spatially correlated MCA noise. Herewith, we recall the baseband model (see Fig. 1.6) for $N_T \times N_R$ OSTBC-MIMO systems. The OSTBC scheme uses N_D time slots to encode $N_B \leq N_T$ data symbols into an $N_T \times N_D$ ST code matrix.

Therefore, the baseband received signal vectors $\mathbf{y}_{n_D}$ can be expressed as

$$\mathbf{y}_{n_D} = \sqrt{\frac{E_b}{N_T}}\mathbf{H}\mathbf{c}_{n_D} + \mathbf{z}_{n_D} \ , \quad n_D = 1, \cdots, N_D \ , \tag{4.58}$$

where $\mathbf{H} \in \mathbb{C}^{N_R \times N_T}$ is a MIMO channel matrix of i.i.d. complex Gaussian entries with zero mean and unit variance. $\mathbf{c}_{n_D} \in \mathbb{C}^{N_T \times 1}$ denotes the n_D^{th} column vector of the OSTBC matrix, $\mathbf{C} \in \mathbb{C}^{N_T \times N_D}$. For spatially coupled impulse noise, the received noise vector, $\mathbf{z}_{n_D} \in \mathbb{C}^{N_R \times 1}$, can be modeled by

$$p_{\mathbf{z}}(\mathbf{z}_{n_D}) = \sum_{m_{n_D}=0}^{\infty} \frac{\alpha_{m_{n_D}}}{(2\pi)^{N_R}|\mathbf{\Sigma}_{m_{n_D}}|} \mathrm{e}^{-\frac{1}{2}\mathbf{z}_{n_D}^H \mathbf{\Sigma}_{m_{n_D}}{}^{-1}\mathbf{z}_{n_D}} \ , \tag{4.59}$$

where $\mathbf{\Sigma}_{m_{n_D}}$ can be given by (4.29). To specify (4.59) over the N_D time slots, we assume that the noise vectors $\mathbf{z}_{n_D}$, $n_D = 1, \cdots, N_D$, are statistically independent. Therefore, the optimum ML decoder selects the code matrix that maximizes the log-likelihood function as follows:

$$\hat{\mathbf{C}}_{\text{ML}} = \arg\max_{\mathbf{C}} \sum_{n_D=1}^{N_D} \log\left(p_{\mathbf{z}}\left(\mathbf{y}_{n_D} - \sqrt{\tfrac{E_b}{N_T}}\mathbf{H}\mathbf{c}_{n_D}\right)\right) \ . \tag{4.60}$$

Similar to the optimum ML decoding of OSTBC in uncorrelated impulse noise, (4.60) cannot be further simplified. However, by stacking the N_D received vectors, $\mathbf{y}_{n_D}$, $\forall n_D$, into a single column vector $\mathbf{y} = [\mathbf{y}_1^T, \cdots, \mathbf{y}_{N_D}^T]^T$, we have

$$\mathbf{y} = \sqrt{\frac{E_b}{N_T}}\left(\mathbf{C}^T \otimes \mathbf{I}_{N_R}\right)\mathbf{h} + \mathbf{z} \ , \tag{4.61}$$

where $\mathbf{C}$ is the OSTBC matrix, $\otimes$ is the Kronecker product, $\mathbf{I}_{N_R}$ denotes the identity matrix of size N_R, and $\mathbf{h} = [\mathbf{h}_1^T, \cdots, \mathbf{h}_{N_T}^T]^T$ sorts the MIMO channel $\mathbf{H}$ into a single column vector. Under perfect knowledge of noise states m_{n_D}, $n_D = 1, \cdots, N_D$, the noise vector $\mathbf{z} = [\mathbf{z}_1^T, \cdots, \mathbf{z}_{N_D}^T]^T$ can be seen as a complex multivariate Gaussian vector with the following covariance matrix

$$\mathbf{\Sigma} = \mathrm{E}\left[\mathbf{z}\mathbf{z}^H\right] = \begin{pmatrix} \mathbf{\Sigma}_{m_1} & \mathbf{0} & \cdots & \mathbf{0} \\ \mathbf{0} & \mathbf{\Sigma}_{m_2} & \cdots & \mathbf{0} \\ \vdots & \vdots & \ddots & \vdots \\ \mathbf{0} & \mathbf{0} & \cdots & \mathbf{\Sigma}_{m_{N_D}} \end{pmatrix} \ , \tag{4.62}$$

where $\mathbf{\Sigma}_{m_{n_D}}$ is the covariance matrix of $\mathbf{z}_{n_D}$ during the n_D^{th} time slot. Similar to a conventional system when the received signals are impaired by correlated Gaussian noise,

a noise-whitening matrix is applied to obtain the equivalent samples with uncorrelated noise. The inverse of the positive definite covariance matrix $\mathbf{\Sigma}$ can be factorized as $\mathbf{\Sigma}^{-1} = \mathbf{L}\mathbf{R} = \mathbf{L}\mathbf{L}^H$. Multiplying (4.61) by $\mathbf{L}^H$, we obtain

$$\mathbf{L}^H\mathbf{y} = \sqrt{\frac{E_b}{N_T}}\mathbf{L}^H(\mathbf{C}^T \otimes \mathbf{I}_{N_R})\mathbf{h} + \mathbf{L}^H\mathbf{z}\,, \tag{4.63}$$

where the elements of $\mathbf{L}^H\mathbf{z}$ are i.i.d. Gaussian distributed random variables with unit variance. Then, the optimum ML receiver reduces to

$$\hat{\mathbf{C}} = \arg\min_{\mathbf{C}} \left|\mathbf{L}^H\mathbf{y} - \sqrt{\tfrac{E_b}{N_T}}\mathbf{L}^H(\mathbf{C}^T \otimes \mathbf{I}_{N_R})\mathbf{h}\right|^2 . \tag{4.64}$$

In the following, we use (4.64) to evaluate the asymptotic PEP of the optimum ST decoder for OSTBC in spatially correlated impulse noise. Furthermore, we show how the threshold detection of noise states can realize (4.64) under no knowledge of noise states.

4.3.1 Asymptotic Pairwise Error Probability

Assume that $\mathbf{C}_0$ is the transmitted ST code matrix and the receiver can decide between two ST code matrices $\mathbf{C}_0$ and $\mathbf{C}_1$. Denote $\mathbf{\Psi}_0 = \mathbf{C}_0^T \otimes \mathbf{I}_{N_R}$ and $\mathbf{\Psi}_1 = \mathbf{C}_1^T \otimes \mathbf{I}_{N_R}$, the probability that $\mathbf{C}_0$ was sent and $\mathbf{C}_1$ is detected can be expressed as

$$\begin{aligned} P(\mathbf{C}_0 \to \mathbf{C}_1|\mathbf{h}, m_{n_D}) &= P\left(\left|\mathbf{L}^H\mathbf{y}_0 - \sqrt{\tfrac{E_b}{N_T}}\mathbf{L}^H\mathbf{\Psi}_1\mathbf{h}\right|^2 \le \left|\mathbf{L}^H\mathbf{y}_0 - \sqrt{\tfrac{E_b}{N_T}}\mathbf{L}^H\mathbf{\Psi}_0\mathbf{h}\right|^2\right)\,, \\ &= P\left(\chi_{ST} \le 0\right)\,. \end{aligned} \tag{4.65}$$

By substituting (4.61) in (4.65), χ_{ST} can be given as

$$\chi_{ST} = \frac{E_b}{N_T}\mathbf{h}^H\mathbf{B}\mathbf{h} + 2\sqrt{\tfrac{E_b}{N_T}}\mathrm{Re}\left\{\mathbf{h}^H\left(\mathbf{\Psi}_0 - \mathbf{\Psi}_1\right)^H\mathbf{\Sigma}^{-1}\mathbf{z}\right\}\,, \tag{4.66}$$

where $\mathbf{B} = (\mathbf{\Psi}_0 - \mathbf{\Psi}_1)^H\mathbf{\Sigma}^{-1}(\mathbf{\Psi}_0 - \mathbf{\Psi}_1)$ is a code distance matrix. Since χ_{ST} is Gaussian with

$$\mu_{\chi_{ST}} = \frac{E_b}{N_T}\mathbf{h}^H\mathbf{B}\mathbf{h}\,, \tag{4.67}$$

and

$$\sigma^2_{\chi_{ST}} = \frac{4E_b}{N_T}\mathbf{h}^H\mathbf{B}\mathbf{h}\,, \tag{4.68}$$

the conditional PEP can be written as

$$P(\mathbf{C}_0 \to \mathbf{C}_1|\mathbf{h}, m_{n_D}) = \mathrm{Q}\left(\frac{\mu_{\chi_{ST}}}{\sigma_{\chi_{ST}}}\right) , \\ = \mathrm{Q}\left(\sqrt{\tfrac{E_b}{4N_T}\mathbf{h}^H\mathbf{B}\mathbf{h}}\right) . \tag{4.69}$$

Since $\mathbf{B}$ is Hermitian, then there exists a unitary matrix $\mathbf{U}$, i.e., $\mathbf{U}^H\mathbf{U} = \mathbf{I}$, such that $\mathbf{U}^H\mathbf{B}\mathbf{U} = \mathbf{\Delta}$, where $\mathbf{\Delta}$ is a diagonal matrix. The diagonal elements, $\mathbf{\Delta}$, $\lambda_{(n_T-1)N_R+n_R}$, $n_T = 1, \cdots, N_T$ and $n_R = 1, \cdots, N_R$, of $\mathbf{\Delta}$ are equivalent to the eigenvalues of $\mathbf{B}$. Therefore, (4.69) reduces to

$$P(\mathbf{C}_0 \to \mathbf{C}_1|\mathbf{h}, m_{n_D}) = \mathrm{Q}\left(\sqrt{\tfrac{E_b}{4N_T}\boldsymbol{\hbar}^H\mathbf{\Delta}\boldsymbol{\hbar}}\right) . \\ = \mathrm{Q}\left(\sqrt{\tfrac{E_b}{4N_T}\sum_{n_T=1}^{N_T}\sum_{n_R=1}^{N_R}|\hbar_{n_Rn_T}|^2\lambda_{(n_T-1)N_R+n_R}}\right) , \tag{4.70}$$

where $\boldsymbol{\hbar} = \mathbf{U}^H\mathbf{h}$. Using the Chernoff bound, (4.70) can be upper-bounded as

$$P(\mathbf{C}_0 \to \mathbf{C}_1|\mathbf{h}, m_{n_D}) \leq \frac{1}{2}\prod_{n_T=1}^{N_T}\prod_{n_R=1}^{N_R}\exp\left(-\tfrac{E_b}{8N_T}|\hbar_{n_Rn_T}|^2\lambda_{(n_T-1)N_R+n_R}\right) . \tag{4.71}$$

Since $\mathbf{U}$ is unitary, then $\boldsymbol{\hbar}$ will follow the same distribution of $\mathbf{h}$. Therefore, $\hbar_{n_Rn_T}$, $\forall n_R$ and $\forall n_T$, are i.i.d. Gaussian random variables. Similar to (4.13), we average the right-hand side of (4.71) with respect the statistics of $|\hbar_{n_Rn_T}|^2$ to arrive at

$$P(\mathbf{C}_0 \to \mathbf{C}_1|m_{n_D}) \leq \frac{1}{2}\prod_{n_T=1}^{N_T}\prod_{n_R=1}^{N_R}\left(\tfrac{1}{1+\frac{E_b}{8N_T}\lambda_{(n_T-1)N_R+n_R}}\right) . \tag{4.72}$$

To simplify the analysis, we consider an $N_T \times N_T$ OSTBC matrix. Since $\mathbf{C}$ is orthogonal, i.e., $\mathbf{C}\mathbf{C}^H = \sum_{n_B=1}^{N_B}|s_{n_B}|^2\mathbf{I}_{N_T}$, and $\mathbf{\Psi} = \mathbf{C}^T \otimes \mathbf{I}_{N_R}$, the eigenvalues of $\mathbf{B}$ can be split as

$$\lambda_{(n_T-1)N_R+n_R} = \beta_{n_T}\zeta_{m_{n_D},n_R} , \quad n_D \equiv n_T = 1, \cdots, N_T , \tag{4.73}$$

where β_{n_T} and $\zeta_{m_{n_D},n_R}$ are the eigenvalues of $(\mathbf{C}_0-\mathbf{C}_1)(\mathbf{C}_0-\mathbf{C}_1)^H$ and $\mathbf{\Sigma}^{-1}_{m_{n_D}}$, respectively. The last step in this derivation is to average $P(\mathbf{C}_0 \to \mathbf{C}_1|m_{n_D})$ over the statistics of m_{n_D}, $n_D = 1, \cdots, N_D$. Since m_{n_D} are independent at different time slots, it follows that $\zeta_{m_{n_D},n_R}$, $n_D \equiv n_T = 1, \cdots N_T$, are also independent for different n_T. Thus, we have

$$P(\mathbf{C}_0 \to \mathbf{C}_1) \leq \frac{1}{2}\prod_{n_T=1}^{N_T}\mathrm{E}_{m_{n_D}}\left\{\prod_{n_R=1}^{N_R}\left(\tfrac{1}{1+\frac{E_b\beta_{n_T}}{8N_T}\zeta_{m_{n_D},n_R}}\right)\right\} . \tag{4.74}$$

At high SNRs, the right-hand side of (4.74) can be approximated as

$$P(\mathbf{C}_0 \to \mathbf{C}_1) < \frac{1}{2}\left(\frac{E_b}{8N_T}\right)^{-N_R N_T}\left(\prod_{n_T=1}^{N_T}\beta_{n_T}\right)^{-N_R}\overbrace{\prod_{n_T=1}^{N_T}\mathrm{E}_{m_{n_D}}\left\{\prod_{n_R=1}^{N_R}\frac{1}{\zeta_{m_{n_D},n_R}}\right\}}^{G_{ST}}. \quad (4.75)$$

For $\mathbf{\Sigma}_{m_{n_D}} = \sigma_G^2\mathbf{I}_{N_R}$, $\forall m_{n_D}$, the eigenvalues $\zeta_{m_{n_D},n_R}$ can be given by $1/\sigma_G^2$, $\forall n_R$. Therefore, the above expression goes to the exact upper bound PEP of OSTBC in the absence of impulse noise [50]. However, in the presence of impulse noise, the last term in (4.75) is related directly to the eigenvalues of $\mathbf{\Sigma}_{m_{n_D}}^{-1}$. To investigate this term in a closed-form expression, we assume MIMO systems with two receive antennas. For $N_R = 2$, $\zeta_{m_{n_D},n_R}$, $n_R = 1, 2$, are given by (4.42). Thus, substituting (4.42) into (4.75) leads to

$$G_{ST} = \prod_{n_T=1}^{N_T}\mathrm{E}_{m_{n_D}}\left\{\sigma^2_{m_{n_D},1}\sigma^2_{m_{n_D},2}\left(1-\rho^2_{m_{n_D}}\right)\right\}. \quad (4.76)$$

For $\rho_{m_{n_D}} = \rho$, G_{ST} can be expressed in terms of σ_G as follows:

$$G_{ST} = \left((\sigma_G^2)^2(1-\rho^2)\left(1+\frac{1}{\Upsilon_1}\right)\left(1+\frac{1}{\Upsilon_2}\right)\left(1+\frac{1}{A(1+\Upsilon_1)(1+\Upsilon_2)}\right)\right)^{N_T}. \quad (4.77)$$

By substituting (4.77) in (4.75), the asymptotic PEP of the optimum ST decoding for $N_T \times 2$ MIMO systems can be given as

$$P(\mathbf{C}_0 \to \mathbf{C}_1) < \frac{1}{2}\left(\frac{E_b}{8N_T\sigma_G^2}\right)^{-2N_T}\left(\prod_{n_T=1}^{N_T}\beta_{n_T}\right)^{-2} \times \left((1-\rho^2)\left(1+\frac{1}{\Upsilon_1}\right)\left(1+\frac{1}{\Upsilon_2}\right)\left(1+\frac{1}{A(1+\Upsilon_1)(1+\Upsilon_2)}\right)\right)^{N_T}. \quad (4.78)$$

Similar to (4.45), the last term measures the performance gap between the impulse-free noise and correlated MCA noise in fading channels. However, we observe that the performance gap in (4.78) is highly dependent on the number of transmit antennas. To confirm this analysis, we simulate the BER of a 2×2 MIMO system with Alamouti ST coding scheme in fading with impulse noise. We assume impulse noise environments with

$\Upsilon_{n_R} = \Upsilon$, $n_R = 1, 2$, and hence, (4.78) can be rewritten as

$$P(\mathbf{C}_0 \to \mathbf{C}_1) < \frac{1}{2}\left(\frac{E_b}{8N_T\sigma_G^2}\right)^{-2N_T}\left(\prod_{n_T=1}^{N_T}\beta_{n_T}\right)^{-2} \times (1-\rho^2)^{N_T}\left(1+\frac{1}{\Upsilon}\right)^{2N_T}\left(1+\frac{1}{A(1+\Upsilon_1)(1+\Upsilon_2)}\right)^{N_T}. \quad (4.79)$$

Since $\sigma_{n_R}^2 \equiv \sigma^2 = \sigma_G^2(1+\frac{1}{\Upsilon})$, $\forall n_R$, (4.79) can be expressed in terms of σ^2 as follows:

$$P(\mathbf{C}_0 \to \mathbf{C}_1) < \frac{1}{2}\left(\frac{E_b}{8N_T\sigma^2}\right)^{-2N_T}\left(\prod_{n_T=1}^{N_T}\beta_{n_T}\right)^{-2}\left((1-\rho^2)\left(1+\frac{1}{A(1+\Upsilon)^2}\right)\right)^{N_T}, \quad (4.80)$$

where $\left(1+\frac{1}{\Upsilon}\right)^{2N_R}$ is the gap between the BER performances for Gaussian noise with variances σ_G^2 and σ^2. Figure. (4.12) illustrates the BER performance of the optimum ST decoding (with and without NSI) versus ρ in impulse noise with different A and $\Upsilon_{1,2} = 0.01$ at an SNR of 45 dB. Additionally, we depict the performances of Gaussian noise with

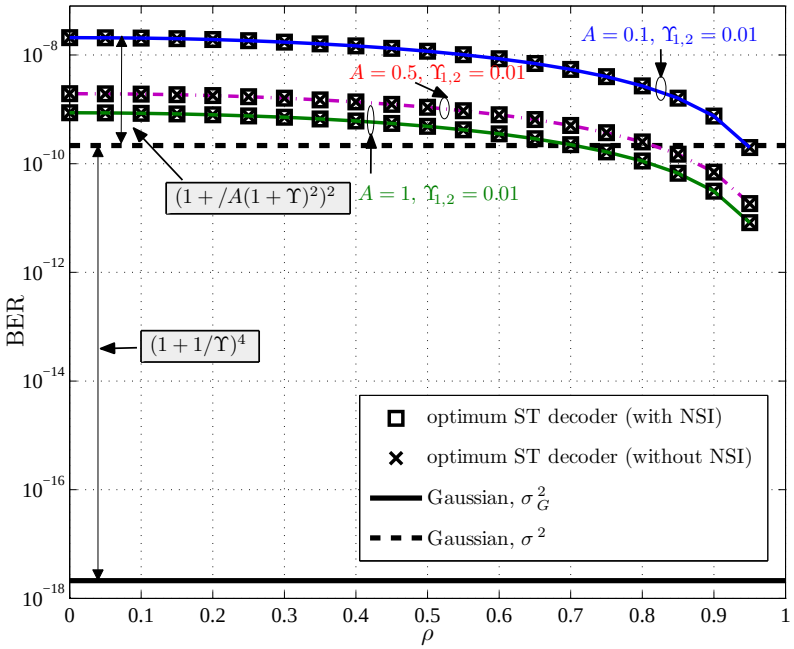

Figure 4.12: The BER performance of the optimum ST decoding versus the correlation coefficient ρ for a 2×2 MIMO system at an SNR = 45 dB

variances σ_G^2 and σ^2 as references. We observe that the performance gaps between the Gaussian limit (with variance σ^2) and MCA noise is proportional to $\left(1+\frac{1}{A(1+\Upsilon)^2}\right)^2$. This explains the performance limitation of OSTBC in impulse noise, which is further increased

by the number of transmit antennas, N_T. However, we observe that the BER performances improve only with increasing ρ, which is in agreement with (4.80). It is worth mentioning that the dependency of the performance gap on impulse noise parameters A and Υ can be removed in the case of a single receive antenna. For $N_R = 1$, (4.76) can be given as

$$G_{ST} = \left(\mathrm{E}_{m_{n_D}}\left\{\sigma^2_{m_{n_D}}\right\}\right)^{N_T} = \left(\sigma^2\right)^{N_T} \ . \tag{4.81}$$

Therefore, the performance gap of OSTBC does neither depend on A nor on N_T, and hence, the performance of the optimum ST decoding in impulse noise approaches the Gaussian limit (with variance σ^2) at high SNRs.

4.3.2 Approximately Optimum Receiver Metrics

The ML decoding of OSTBC in Gaussian noise leads to an MD decoder. However, when it comes to MCA noise, we observe that the optimum ST decoding metric in (4.60) cannot be further simplified. We hence again employed a threshold detection scheme to estimate the noise states m_{n_D} for different time slots. Thus, similar to (4.50), the noise state m_{n_D} can be extracted from the received vector $\mathbf{y}_{n_D}$ during the n_D^{th} time slot as

$$\tilde{m}_{\mathbf{y}_{n_D}|\mathbf{c}_{n_D}} = \begin{cases} 0 & \text{if } (\mathbf{y}_{n_D} - \sqrt{\frac{E_b}{N_T}}\mathbf{H}\mathbf{c}_{n_D})^H \mathbf{M} (\mathbf{y}_{n_D} - \sqrt{\frac{E_b}{N_T}}\mathbf{H}\mathbf{c}_{n_D}) \leq d_2 \ , \\ 1 & \text{otherwise} \ , \end{cases} \tag{4.82}$$

where $\mathbf{M} = \mathbf{\Sigma}_0^{-1} - \mathbf{\Sigma}_1^{-1}$ and $d_2 = 2\log\left(\frac{\alpha_0|\mathbf{\Sigma}_1|}{\alpha_1|\mathbf{\Sigma}_0|}\right)$. Using this estimate, the ML metric in (4.60) can be approximated as follows:

$$\hat{\mathbf{C}}_{\text{ML}} \approx \arg\min_{\mathbf{C}} \sum_{n_D=1}^{N_D} \left| \mathbf{L}^H_{\tilde{m}_{\mathbf{y}_{n_D}|\mathbf{c}_{n_D}}} \mathbf{y}_{n_D} - \sqrt{\tfrac{E_b}{N_T}} \mathbf{L}^H_{\tilde{m}_{\mathbf{y}_{n_D}|\mathbf{c}_{n_D}}} \mathbf{H}\mathbf{c}_{n_D} \right|^2 - \sum_{n_D=1}^{N_D} \log\left(\frac{\alpha_{\tilde{m}_{\mathbf{y}_{n_D}|\mathbf{c}_{n_D}}}}{|\mathbf{\Sigma}_{\tilde{m}_{\mathbf{y}_{n_D}|\mathbf{c}_{n_D}}}|} \right) . \tag{4.83}$$

From (4.64) and (4.83), we note that the difference between the optimum decoding metric (under perfect NSI) and the approximate ML metrics is the bias term, which depends on the noise state estimate at the n_D^{th} time slot. To assess this approximation, we simulated the BER performance of the approximate ML metric and the optimum ST decoding of OSTBC in different impulse noise environments. Figure (4.13) depicts the BER results of the 2×2 MIMO system in spatially uncorrelated MCA noise with different A and $\Upsilon_{1,2} = 0.01$. We observe that the approximate ML decoder offers similar performances to the optimum ST decoder for different impulse noise environments. Moreover, we note that, at high SNRs, there is a gap in the SNR between of the performances of OSTBC in

impulse noise and Gaussian noise (with variance σ^2). We observe that this gap increases as A decreases, which is consistent with the performance loss of the optimum ST decoding. To deduce the performance loss of multiple-antenna systems with $N_R = 1$, we simulate

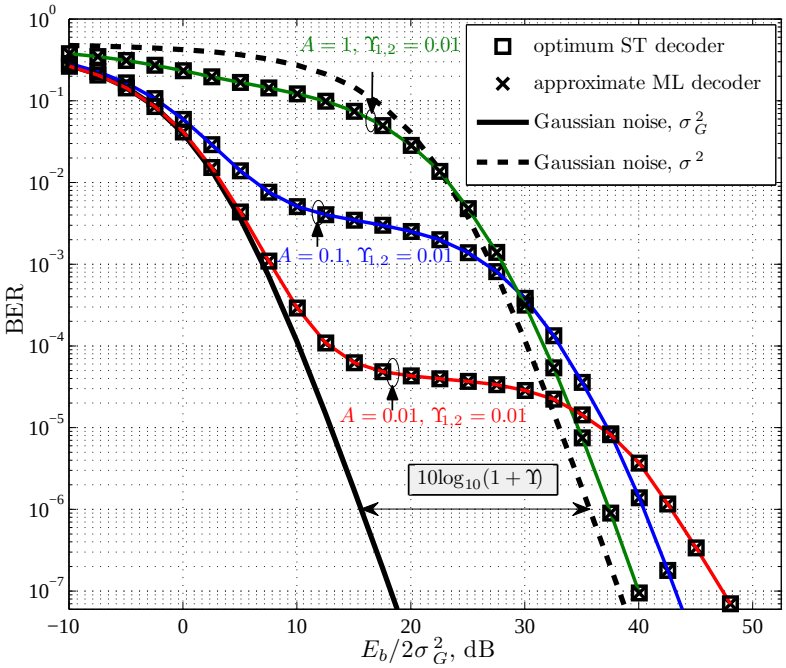

Figure 4.13: BER Performance of the optimum ST decoding for a 2×2 MIMO system in impulse noise

the BER of a 2×1 multiple-input single-output (MISO) system in the presence of MCA noise. Figure (4.14) depicts the BER performances of the optimum and approximate ML decoding schemes in impulse noise with different A and $\Upsilon_{1,2} = 0.01$. We observe that, at high SNRs, the achievable performances in impulse noise with different A approach those of Gaussian noise with variance σ^2, which is in agreement with (4.81).

4.4 Conclusion

In this chapter, we investigated the optimum combining schemes for time and spatial diversity of wireless communication systems in the presence of fading and impulse noise. Analytically, we evaluated an expression for the upper performance bound of the optimum detectors for time diversity, multiple antenna systems, and space-time coding in Rayleigh fading and MCA noise. To simplify the analysis, we assume perfect knowledge of noise states, which leads to tractable upper performance bounds. For time diversity, we showed that the performance of the optimum detector in impulse noise with variance σ^2 is upper-bounded by those of Gaussian noise with variance σ^2. However, for multiple antenna

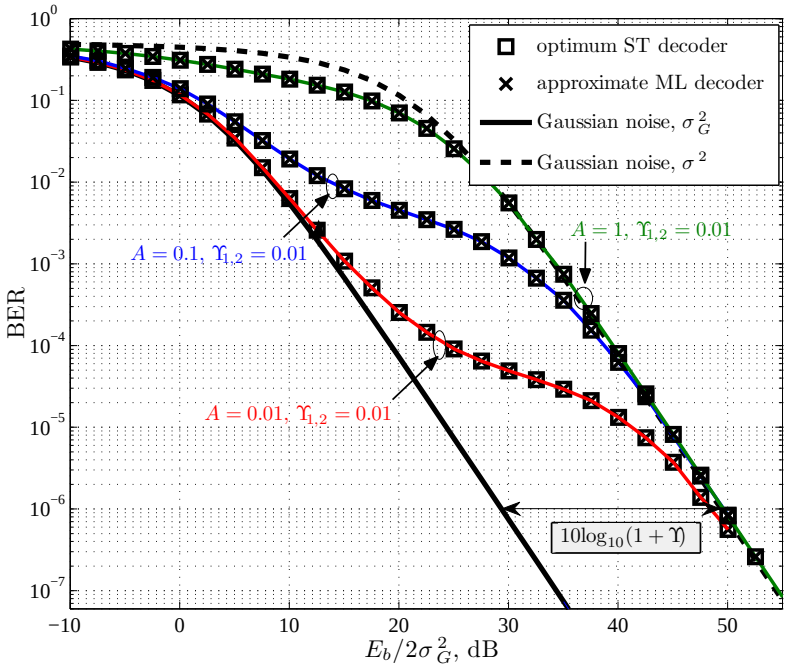

Figure 4.14: BER Performance of the optimum ST decoding for a 2×1 MISO system in impulse noise

systems, we showed that the upper performance bound of the optimum detector in spatially coupled impulse noise is limited by the impulsiveness of the noise. Moreover, we indicated how this limitation increases significantly with the numbers of transmit and receive antennas. One interesting conclusion to be drawn from this chapter is that the limitation of MIMO systems in impulse noise can be reduced by using a single receive antenna, i.e., MISO systems. Then, increasing the number of transmit antennas will not reduce the performance improvements of the optimum detector in different impulse noise environments.

Chapter 5

Multicarrier Systems in Impulse Noise

Our treatment of impulse noise up to this point has been focused on a single-carrier systems involving dimensions in time and space. In this chapter, we shift the focus to multicarrier systems in the presence of impulse noise. We consider several detection schemes of OFDM signals corrupted by MCA noise, such as an optimum detector, a conventional receiver, and a nonlinear detector. To investigate the error probability of the optimum detector, we assume that the noise states of MCA noise are available at the receiver. Under this assumption, we show that the performance of the optimum detector in different impulse noise environments approaches the impulse-free limit as the number of subcarriers increases. To realize such performances, we introduce a lattice decoder along with sparse Bayesian learning (SBL) to implement the optimum detector for OFDM systems in impulse noise.

5.1 Detection Techniques

Impulse noise often appears in the form of short pulses, which can be assumed very short compared with the duration of an OFDM symbol. Since the spectrum of MCA noise is comparable to the bandwidth of the OFDM system, all subcarriers are impaired by impulse noise. This explains the limited performance of the conventional OFDM system in strong impulse noise. There are several signal processing methods to mitigate the effect of impulse noise in OFDM systems [37, 41, 42, 49, 51, 52]. Those methods can be classified according to impulse noise suppression either in time or frequency. In a time-

domain approach, impulse noise cancellation is implemented before OFDM demodulation such as a clipping and a blanking nonlinearity [37, 41, 52]. However, this approach has the disadvantage that it cancels the desired OFDM signal together with the impulse noise, which degrades the system performance. In frequency-domain, there are several algorithms for compensating the effect of impulse noise after OFDM demodulation [42,49]. However, none of these methods realizes an optimum detection of the OFDM signal corrupted by impulse noise. In this section, we consider the optimum detection scheme of OFDM signals in impulse noise. Thus, we consider a multicarrier system with N subcarriers. The transmitted OFDM symbol $\mathbf{x} = [x_0\ x_1\ \cdots\ x_{N-1}]^T$ can be generated via an IDFT matrix as follows:

$$\mathbf{x} = \mathbf{W}_N^H \mathbf{s}\ , \tag{5.1}$$

where $\mathbf{W}_N^H$ is the IDFT matrix and $\mathbf{s} \in \mathbb{C}^{N\times 1}$ is the column vector of information symbols taken from a complex constellation set. As in (1.49), the received OFDM symbol after the CP removal is given by

$$\mathbf{y} = \sqrt{E_b}\bar{\mathbf{H}}\mathbf{x} + \mathbf{z}\ , \tag{5.2}$$

where $\bar{\mathbf{H}} \in \mathbb{C}^{N\times N}$ is a circulant convolution channel matrix of i.i.d. complex Gaussian entries and $\mathbf{z} \in \mathbb{C}^{N\times 1}$ denotes the complex-valued MCA noise vector. Since the samples of $\mathbf{z}$ are statistically independent, the noise vector $\mathbf{z} = [z_0, \cdots, z_{N-1}]^T$ can be modeled as

$$p_{\mathbf{z}}(\mathbf{z}) = \prod_{n=0}^{N-1} \sum_{m_n=0}^{\infty} \frac{\alpha_{m_n}}{2\pi\sigma_{m_n}^2} \mathrm{e}^{-|z_n|^2/2\sigma_{m_n}^2}\ , \tag{5.3}$$

where $\sigma_{m_n}^2 = \sigma_G^2 + \frac{m_n}{A}\sigma_I^2$. m_n, $n = 0, \cdots, N-1$, represents the NSI of the received noise vector $\mathbf{z}$. α_{m_n} is the Poisson distribution of a noise state m_n for the n^{th} noise observation, z_n. In the following, we introduce the optimum receiver design for OFDM systems in the presence of MCA noise. Then, we discus two suboptimum detectors such as a zero-forcing detector and a minimum mean-square error detector.

5.1.1 The Optimum Detector

We assume that the channel matrix $\bar{\mathbf{H}}$ is known at the receiver. Moreover, we further assume that the noise statistics A and Υ are perfectly estimated from the received samples [53]. From (5.3), the joint PDF of the received signal vector, $\mathbf{y}$, conditioned on the transmitted information symbol, $\mathbf{s}_0$, is given by

$$p(\mathbf{y}|\mathbf{s}_0) = \prod_{n=0}^{N-1} \sum_{m_n=0}^{\infty} \frac{\alpha_{m_n}}{2\pi\sigma_{m_n}^2} \mathrm{e}^{-\frac{\left|y_n - \sqrt{E_b}\bar{\mathbf{h}}_n \mathbf{W}_N^H \mathbf{s}_0\right|^2}{2\sigma_{m_n}^2}}\ , \tag{5.4}$$

where $\bar{\mathbf{h}}_n$ is the n^{th} row vector of the circulant channel matrix $\bar{\mathbf{H}}$. The optimum detector selects the sequence, $\hat{\mathbf{s}}_0$, that maximizes this quantity as

$$\hat{\mathbf{s}}_{\text{ML}} = \arg\max_{\mathbf{s}} \prod_{n=0}^{N-1} \sum_{m_n=0}^{\infty} \frac{\alpha_{m_n}}{2\pi\sigma_{m_n}^2} \mathrm{e}^{-\frac{\left|y_n - \sqrt{E_b}\bar{\mathbf{h}}_n \mathbf{W}_N^H \mathbf{s}\right|^2}{2\sigma_{m_n}^2}} . \tag{5.5}$$

For antipodal information sequences, the optimum detector should search over 2^N possible choices of the bits in the received signal vector $\mathbf{y}$. Under perfect knowledge of the NSI, m_n, $n = 0, \cdots, N-1$, the likelihood functions, $p(\mathbf{y}|\mathbf{s})$, reduce to a conditional N-dimensional complex Gaussian PDF as follows:

$$p(\mathbf{y}|\mathbf{s}, m_n) = \frac{1}{(2\pi)^N |\mathbf{\Sigma}_z|} e^{-\frac{1}{2}\left(\mathbf{y} - \sqrt{E_b}\bar{\mathbf{H}}\mathbf{W}_N^H \mathbf{s}\right)^H \mathbf{\Sigma}_z^{-1} \left(\mathbf{y} - \sqrt{E_b}\bar{\mathbf{H}}\mathbf{W}_N^H \mathbf{s}\right)} . \tag{5.6}$$

Since the noise observations are statistically independent, the covariance matrix $\mathbf{\Sigma_z}$ is given by $\mathbf{\Sigma_z} = \text{diag}[\sigma_{m_0}^2, \cdots, \sigma_{m_{N-1}}^2]$. For $\mathbf{\Sigma_z}^{-1} = \mathbf{L}\mathbf{L}^H$, the ML estimate of $\mathbf{s}_0$ leads to

$$\hat{\mathbf{s}}_{\text{ML}} = \arg\min_{\mathbf{s}} \left| \mathbf{L}^H \mathbf{y} - \sqrt{E_b}\mathbf{L}^H \bar{\mathbf{H}} \mathbf{W}_N^H \mathbf{s} \right|^2 , \tag{5.7}$$

which searches over all possible information symbols to select a closest signal vector $\hat{\mathbf{s}}_0 = \hat{\mathbf{s}}_{\text{ML}}$ to the received vector $\mathbf{L}^H\mathbf{y}$. Therefore, the optimum detector that assumes perfect NSI requires the same exhaustive searching process as in (5.5). However, the minimum distance (MD) metrics in (5.7) can lead to a tractable performance evaluation of the optimum detector for multicarrier systems in impulse noise.

5.1.2 Suboptimum Detectors

As a suboptimum solution, there are two well-known criteria to minimize (5.7). One is a zero-forcing (ZF) criterion and the other is a mean-squared error (MSE) criterion. The ZF solution provides a linear estimate of $\mathbf{s}_0$, which minimizes the MD metric defined as

$$\Lambda(\mathbf{s}) = \left| \mathbf{L}^H \mathbf{y} - \sqrt{E_b}\mathbf{L}^H \bar{\mathbf{H}} \mathbf{W}_N^H \mathbf{s} \right|^2 . \tag{5.8}$$

This metric can easily be minimized with respect to $\mathbf{s}$, which yields

$$\begin{aligned} \hat{\mathbf{s}}_{\text{ZF}} &= \tfrac{1}{\sqrt{E_b}} \mathbf{W}_N \bar{\mathbf{H}}^{-1} \mathbf{y} , \\ &= \mathbf{s}_0 + \tfrac{1}{\sqrt{E_b}} \mathbf{W}_N \bar{\mathbf{H}}^{-1} \mathbf{z} . \end{aligned} \tag{5.9}$$

From (5.9), we observe that the ZF detector applies a DFT matrix after eliminating the channel matrix $\bar{\mathbf{H}}$. This leads to a conventional OFDM detector, which has a limited performance in strong impulse noise ($A\Upsilon < 1$). In the MSE criterion, we provide an estimate of the OFDM symbol $\mathbf{x}$, which minimizes the mean square value of the error

$$J(\mathbf{x}) = \mathrm{E}\left[\left|\sqrt{E_b}\bar{\mathbf{H}}\mathbf{x} - \mathbf{A}\mathbf{y}\right|^2\right] , \tag{5.10}$$

where $\mathbf{A}$ is a transformation matrix. The optimum choice of $\mathbf{A}$ that minimizes $J(\mathbf{x})$ is

$$\mathbf{A} = \left(\sigma_s^2\mathbf{I}_N\left(\sigma_s^2\mathbf{I}_N + \mathbf{\Sigma_z}\right)^{-1}\right) , \tag{5.11}$$

where $\sigma_s^2 = E_b\sum_{l_p=0}^{L_p-1}|h_{l_p}|^2$. Hence, the MMSE estimate $\hat{\mathbf{x}}_{\mathrm{MSE}}$ follows as

$$\hat{\mathbf{x}}_{\mathrm{MSE}} = \left(\sigma_s^2\mathbf{I}_N\left(\sigma_s^2\mathbf{I}_N + \mathbf{\Sigma_z}\right)^{-1}\right)\mathbf{y} . \tag{5.12}$$

We observe from (5.12) that the MMSE solution requires perfect knowledge of $\mathbf{\Sigma}_z$, which depends on the noise states, m_n. Since $\mathbf{\Sigma_z}$ is a diagonal matrix, the MMSE estimate of the n^{th} observation is $\hat{x}_n = \frac{\sigma_s^2}{\sigma_s^2+\sigma_{m_n}^2}y_n$. For impulse noise with two states, i.e., $m_n = 0$ for Gaussian noise and $m_n = 1$ for impulse, we have

$$\hat{x}_n = \begin{cases} \frac{\sigma_s^2}{\sigma_s^2+\sigma_0^2}y_n & \text{if } m_n = 0 , \\ \frac{\sigma_s^2}{\sigma_s^2+\sigma_1^2}y_n & \text{if } m_n = 1 . \end{cases} \tag{5.13}$$

Thus, the received OFDM observations are scaled according to the variances of the received noise. Since $\sigma_1^2 >> \sigma_0^2$ for $A\Upsilon < 1$, the MMSE solution can be approximated by a blanking nonlinearity [39] as follows:

$$\hat{x}_n \approx \begin{cases} y_n & \text{if } m_n = 0 , \\ 0 & \text{if } m_n = 1 , \end{cases} \tag{5.14}$$

which justifies the widespread use of the blanking nonlinearities in multicarrier systems to mitigate the effects of impulse noise.

5.2 Performance Analysis of the Optimum Detector

Due to the lattice structure of the IDFT transform, the optimum detector is equivalent to determine the ML estimate of a lattice point $\hat{\mathbf{x}}_{\mathrm{ML}}$ from the received OFDM symbol $\mathbf{y}$ in the

N-dimensional lattice space. Figure 5.1 illustrates the lattice space of the transmitted OFDM symbols using a two-dimensional IDFT transform for binary PSK information signals. To show how the decision regions of the optimum detector look like in the lattice

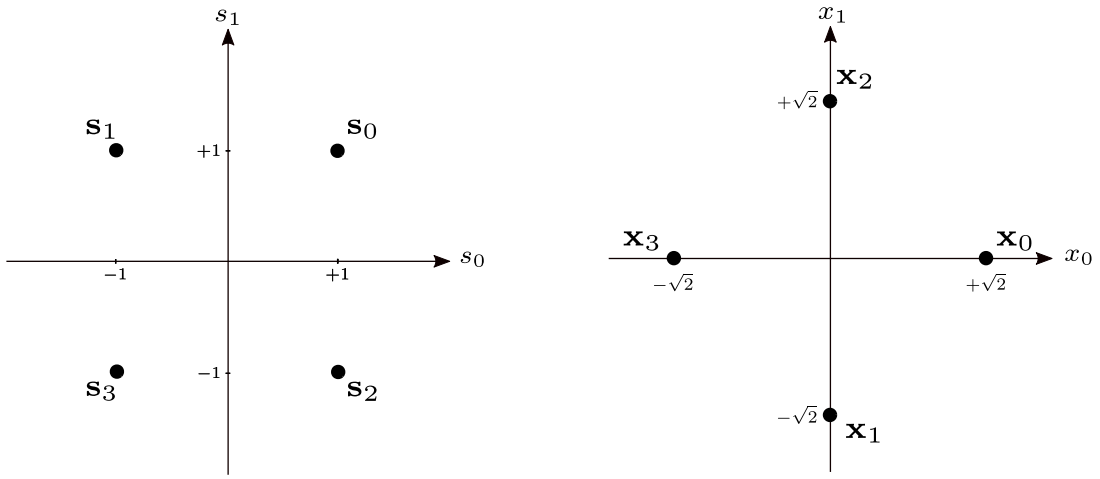

(a) Signal space (b) Lattice space

Figure 5.1: The two-dimensional lattice of $\mathbf{W}_2^H$ contains all lattice points for binary PSK modulated symbols

space, we assume that the detector decides between two lattice points $\mathbf{x}_i$ and $\mathbf{x}_j$. Under no knowledge of the NSI, the optimum detector should estimate the noise states, m_n, $\forall n$, from the received OFDM samples y_n. Under each lattice point, the NSI can be estimated as

$$\hat{m}_{n|\mathbf{x}_{i,j}} = \begin{cases} 0 & \text{if } \left|y_n - \sqrt{E_b}\bar{\mathbf{h}}_n \mathbf{x}_{i,j}\right|^2 \leq d_1^2 \ , \\ 1 & \text{if elsewhere} \ , \end{cases} \tag{5.15}$$

where $d_1 = \sqrt{\frac{2\sigma_0^2\sigma_1}{\sigma_1^2-\sigma_0^2}\log\frac{\alpha_0\sigma_1^2}{\alpha_1\sigma_0^2}}$. This means the NSI seen by each lattice point $\mathbf{x}_i$ and $\mathbf{x}_j$ are not necessarily identical. Then, the likelihood functions, $p(\mathbf{y}|\mathbf{x}_{i,j}, \hat{m}_{n|\mathbf{x}_{i,j}})$, can be given as

$$p(\mathbf{y}|\mathbf{x}_{i,j}, \hat{m}_{n|\mathbf{x}_{i,j}}) = \frac{1}{(2\pi)^N |\mathbf{\Sigma}_{\mathbf{z}|\mathbf{x}_{i,j}}|} e^{-\frac{1}{2}\left(\mathbf{y}-\sqrt{E_b}\bar{\mathbf{H}}\mathbf{x}_{i,j}\right)^H \mathbf{\Sigma}_{\mathbf{z}|\mathbf{x}_{i,j}}^{-1}\left(\mathbf{y}-\sqrt{E_b}\bar{\mathbf{H}}\mathbf{x}_{i,j}\right)} \ , \tag{5.16}$$

where $\mathbf{\Sigma}_{\mathbf{z}|\mathbf{x}_{i,j}} = \text{diag}[\sigma^2_{\hat{m}_{0|\mathbf{x}_{i,j}}}, \cdots, \sigma^2_{\hat{m}_{N-1|\mathbf{x}_{i,j}}}]$ are the covariance matrices conditioned on the noise state estimates $\hat{m}_{n|\mathbf{x}_{i,j}}$. For equally likely lattice points, the optimum decision regions between the lattice points $\mathbf{x}_i$ and $\mathbf{x}_j$ can be derived as

$$\log\left(p(\hat{m}_{0|\mathbf{x}_j}, \cdots, \hat{m}_{N-1|\mathbf{x}_j}) p(\mathbf{y}|\mathbf{x}_i, \hat{m}_{n|\mathbf{x}_i})\right) = \log\left(p(\hat{m}_{0|\mathbf{x}_j}, \cdots, \hat{m}_{N-1|\mathbf{x}_j}) p(\mathbf{y}|\mathbf{x}_j, \hat{m}_{n|\mathbf{x}_j})\right) \ . \tag{5.17}$$

Since the noise states are independent and $p(\hat{m}_{n|\mathbf{x}})$ is given by $\alpha_{\hat{m}_{n|\mathbf{x}}}$, the joint PDF $p(\hat{m}_{0|\mathbf{x}}, \cdots, \hat{m}_{N-1|\mathbf{x}})$ cab be expressed as $\prod_{n=0}^{N-1} \alpha_{\hat{m}_{n|\mathbf{x}}}$. Therefore, by substituting (5.16)

in (5.17), we have

$$\mathbf{y}^H(\boldsymbol{\Sigma}^{-1}_{\mathbf{z}|\mathbf{x}_j}-\boldsymbol{\Sigma}^{-1}_{\mathbf{z}|\mathbf{x}_i})\mathbf{y}+2\sqrt{E_b}\mathrm{Re}\{(\mathbf{x}_i^H\bar{\mathbf{H}}^H\boldsymbol{\Sigma}^{-1}_{\mathbf{z}|\mathbf{x}_i}-\mathbf{x}_j^H\bar{\mathbf{H}}^H\boldsymbol{\Sigma}^{-1}_{\mathbf{z}|\mathbf{x}_j})\mathbf{y}\} \\ -E_b(\mathbf{x}_i^H\bar{\mathbf{H}}^H\boldsymbol{\Sigma}^{-1}_{\mathbf{z}|\mathbf{x}_i}\bar{\mathbf{H}}\mathbf{x}_i-\mathbf{x}_j^H\bar{\mathbf{H}}^H\boldsymbol{\Sigma}^{-1}_{\mathbf{z}|\mathbf{x}_j}\bar{\mathbf{H}}\mathbf{x}_j)=2\sum_{n=0}^{N-1}\log\left(\frac{\sigma^2_{\hat{m}_n|\mathbf{x}_i}\alpha_{\hat{m}_n|\mathbf{x}_j}}{\sigma^2_{\hat{m}_n|\mathbf{x}_j}\alpha_{\hat{m}_n|\mathbf{x}_i}}\right), \tag{5.18}$$

which depicts the nonlinear decision regions for $\mathbf{x}_i$ and $\mathbf{x}_j$ in the N-dimensional lattice space. The decision region in (5.18) leads to an intractable performance evaluation of the optimum detector for multicarrier systems in impulse noise. However, under perfect knowledge of the noise states, we have $\boldsymbol{\Sigma}_{\mathbf{z}|\mathbf{x}_{i,j}}=\boldsymbol{\Sigma}_{\mathbf{z}}$ and $\alpha_{m_n}=1$. Hence, the decision region in (5.18) reduces to

$$2\sqrt{E_b}\mathrm{Re}\{(\mathbf{x}_i-\mathbf{x}_j)^H\bar{\mathbf{H}}^H\boldsymbol{\Sigma}_{\mathbf{z}}^{-1}\mathbf{y}\}-E_b(\mathbf{x}_i^H\bar{\mathbf{H}}^H\boldsymbol{\Sigma}_{\mathbf{z}}^{-1}\bar{\mathbf{H}}\mathbf{x}_i-\mathbf{x}_j^H\bar{\mathbf{H}}^H\boldsymbol{\Sigma}_{\mathbf{z}}^{-1}\bar{\mathbf{H}}\mathbf{x}_j)=0\,. \tag{5.19}$$

The decision boundary in (5.19) depicts an affine hyperplane in the N-dimensional lattice space. It is worth mentioning that, in the absence of impulse noise, i.e., $\boldsymbol{\Sigma}_{\mathbf{z}}=\sigma_G^2\mathbf{I}_N$, the affine hyperplane is further reduced to

$$2\sqrt{E_b}\mathrm{Re}\{(\mathbf{x}_0-\mathbf{x}_1)^H\bar{\mathbf{H}}^H\boldsymbol{\Sigma}_{\mathbf{z}}^{-1}\mathbf{y}\}=0\,, \tag{5.20}$$

which represents a set of linear equations of that goes through the origin. This justifies why the DFT transformation is optimum for OFDM signals corrupted by Gaussian noise. In the following, we use (5.19) to evaluate the PEP between the lattice points $\mathbf{x}_i$ and $\mathbf{x}_j$. Then, we introduce the asymptotic probability of error for the optimum detector of a multicarrier system in impulse noise.

5.2.1 Pairwise Error Probability

From (5.19), the optimum decision rule can be expressed as

$$\mathrm{Re}\{(\mathbf{x}_i-\mathbf{x}_j)^H\bar{\mathbf{H}}^H\boldsymbol{\Sigma}_{\mathbf{z}}^{-1}\mathbf{y}\}-\sqrt{\tfrac{E_b}{4}}(\mathbf{x}_i^H\bar{\mathbf{H}}^H\boldsymbol{\Sigma}_{\mathbf{z}}^{-1}\bar{\mathbf{H}}\mathbf{x}_i-\mathbf{x}_j^H\bar{\mathbf{H}}^H\boldsymbol{\Sigma}_{\mathbf{z}}^{-1}\bar{\mathbf{H}}\mathbf{x}_j)\underset{\mathbf{x}_j}{\overset{\mathbf{x}_i}{\gtrless}}0\,. \tag{5.21}$$

Under perfect knowledge of $\bar{\mathbf{H}}$ and m_n, $\forall n$, supposing $\mathbf{x}_i$ was sent, the decision variable in (5.21) reduces to

$$\chi_{MC}=\mathrm{Re}\{(\mathbf{x}_i-\mathbf{x}_j)^H\bar{\mathbf{H}}^H\boldsymbol{\Sigma}_z^{-1}\mathbf{z}\}+\sqrt{\tfrac{E_b}{4}}(\mathbf{x}_i-\mathbf{x}_j)^H\bar{\mathbf{H}}^H\boldsymbol{\Sigma}_z^{-1}\bar{\mathbf{H}}(\mathbf{x}_i-\mathbf{x}_j)\underset{\mathbf{x}_j}{\overset{\mathbf{x}_i}{\gtrless}}0\,. \tag{5.22}$$

The PEP is simply the probability that χ_{MC} is less than zero. The decision variable, χ_{MC}, is Gaussian with mean

$$\mu_{\chi_{MC}} = \sqrt{\tfrac{E_b}{4}}(\mathbf{x}_i - \mathbf{x}_j)^H \bar{\mathbf{H}}^H \mathbf{\Sigma}_z^{-1} \bar{\mathbf{H}}(\mathbf{x}_i - \mathbf{x}_j) \; , \tag{5.23}$$

and variance

$$\sigma^2_{\chi_{MC}} = (\mathbf{x}_i - \mathbf{x}_j)^H \bar{\mathbf{H}}^H \mathbf{\Sigma}_z^{-1} \bar{\mathbf{H}}(\mathbf{x}_i - \mathbf{x}_j) \; . \tag{5.24}$$

Hence, the conditional PEP can be computed as

$$\begin{aligned} P(\mathbf{x}_i \to \mathbf{x}_j | \bar{\mathbf{H}}, m_n) &= \mathrm{Q}\left(\frac{\mu_{\chi_{MC}}}{\sigma_{\chi_{MC}}}\right) \; , \\ &= \mathrm{Q}\left(\sqrt{\tfrac{E_b}{4}(\mathbf{x}_i - \mathbf{x}_j)^H \bar{\mathbf{H}}^H \mathbf{\Sigma}_z^{-1} \bar{\mathbf{H}}(\mathbf{x}_i - \mathbf{x}_j)}\right) \; . \end{aligned} \tag{5.25}$$

For simplicity, we assume that the fading channel is flat, e.g., $\bar{\mathbf{H}} = h_0 \mathbf{I}_N$. Since $\sigma^2_{m_n} = \sigma^2_G(1 + \frac{m_n}{A\Upsilon})$, $n = 0, \cdots, N-1$, (5.25) reduces to

$$P(\mathbf{x}_i \to \mathbf{x}_j | h_0, m_n) = \mathrm{Q}\left(\sqrt{\tfrac{E_b}{4\sigma^2_G}|h_0|^2 d^2(\mathbf{x}_i, \mathbf{x}_j, m_n)}\right) \; , \tag{5.26}$$

where

$$d^2(\mathbf{x}_i, \mathbf{x}_j, m_n) = \sum_{n=0}^{N-1} \frac{|x_{i,n} - x_{j,n}|^2}{1 + \frac{m_n}{A\Upsilon}} \; . \tag{5.27}$$

Using the Chernoff bound, (5.26) can be upper-bounded as

$$P(\mathbf{x}_i \to \mathbf{x}_j | h_0, m_n) \leq \frac{1}{2} \exp\left(-\tfrac{E_b}{8\sigma^2_G}|h_0|^2 d^2(\mathbf{x}_i, \mathbf{x}_j, m_n)\right) \; . \tag{5.28}$$

Since $|h_0|$ is a Rayleigh-distributed random variable, $|h_0|^2$ has a chi-square probability distribution with two degrees of freedom. Thus, we have

$$p(|h_0|^2) = \frac{1}{\bar{h}} \exp\left(-\frac{|h_0|^2}{\bar{h}}\right) \; , \quad |h_0|^2 \geq 0 \; , \tag{5.29}$$

where $\bar{h} = \mathrm{E}\{|h_0|^2\}$ denotes the average power of the channel. We average the conditional PEP, given in (5.28), over the PDF of $|h_0|^2$ as follows:

$$\begin{aligned} P(\mathbf{x}_i \to \mathbf{x}_j | m_n) &= \int_0^\infty P(\mathbf{x}_i \to \mathbf{x}_j | h_0, \mathbf{m}) p\left(|h_0|^2\right) d|h_0| \; , \\ &\leq \frac{1}{2} \frac{1}{1 + \frac{E_b}{8\sigma^2_G} d^2(\mathbf{x}_i, \mathbf{x}_j, m_n)} \; . \end{aligned} \tag{5.30}$$

At high SNR, the right-hand side of (5.30) can be approximated as

$$P(\mathbf{x}_i \to \mathbf{x}_j | m_n) < \left(\frac{E_b}{\sigma_G^2}\right)^{-1} \frac{4}{d^2(\mathbf{x}_i, \mathbf{x}_j, m_n)} \,. \tag{5.31}$$

By averaging (5.31) over the noise state probabilities, α_{m_n}, the upper bound of the PEP is

$$P(\mathbf{x}_i \to \mathbf{x}_j) < \left(\frac{E_b}{\sigma_G^2}\right)^{-1} \overbrace{\sum_{m_0=0}^{\infty} \cdots \sum_{m_{N-1}=0}^{\infty} \frac{4 \prod_{n=0}^{N-1} \alpha_{m_n}}{d^2(\mathbf{x}_i, \mathbf{x}_j, m_n)}}^{G(\mathbf{x}_i, \mathbf{x}_j)} \,. \tag{5.32}$$

From (5.32), we observe that the upper bound of the PEP performance consists of two terms. The first term decreases inversely with the SNR, $E_b/2\sigma_G^2$. The second term depends on the parameters of the MCA noise.

5.2.2 Upper Performance Bound

We assume a binary PSK modulation scheme for the information symbols $\mathbf{s}$. Using the union bound, the probability of error is upper-bounded by

$$P_e \leq \frac{1}{2^N} \sum_{i=0}^{2^{N-1}} \sum_{\substack{j=0 \\ j \neq i}}^{2^N - 1} \frac{n_d(i,j)}{N} P(\mathbf{x}_i \to \mathbf{x}_j) \,, \tag{5.33}$$

where $n_d(i,j)$ is the number of bit errors when the symbol $\mathbf{x}_i$ is erroneously detected as a symbol $\mathbf{x}_j$. We first assess the asymptotic probability of error for the optimum detector in Gaussian noise with variance $\sigma_G^2 = \sigma_0^2$. In the absence of impulse noise, i.e., $m_n = 0$, $\forall n$, the linear decision boundaries in (5.20) divides the lattice space (in two-dimensional lattices) into 4 symmetric decision regions as illustrated in Fig. 5.2. Accordingly, $d^2(\mathbf{x}_i, \mathbf{x}_j, m_n)$, for $m_n = 0$, reduces to the Euclidean squared distance between the corresponding signal points, $(\mathbf{s}_i - \mathbf{s}_j)^H (\mathbf{s}_i - \mathbf{s}_j)$. Therefore, the probability of error is upper-bounded by summing the PEPs of nearest-neighbor (Euclidean) lattice points as

$$P_e < \left(\frac{E_b}{\sigma_G^2}\right)^{-1} \frac{1}{2^N} \sum_{i=0}^{2^{N-1}} \sum_{\substack{j=1 \\ j \neq i}}^{N_i} \frac{n_d(i,j)}{N} \frac{4}{d_{\min}^2(\mathbf{x}_i, \mathbf{x}_j)} \,, \tag{5.34}$$

where $d_{\min}^2(\mathbf{x}_i, \mathbf{x}_j)$ denotes the minimum Euclidean distance and N_i is the number of neighboring lattice points for the point $\mathbf{x}_i$. Since $d_{\min}^2(\mathbf{x}_i, \mathbf{x}_j) = 4$ and $N_i = N$ for binary

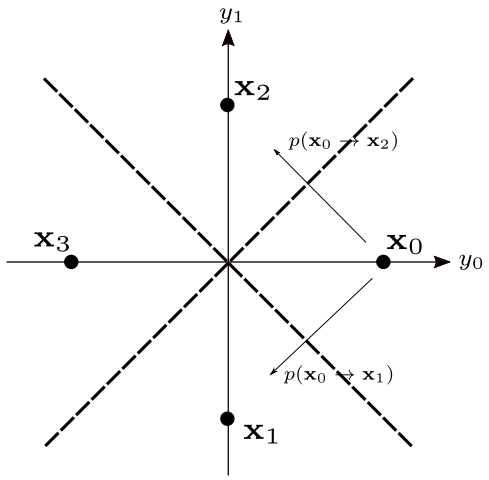

Figure 5.2: Decision boundaries of the optimum detector for Gaussian noise

PSK, (5.34) is further reduced to

$$P_e < \left(\frac{E_b}{\sigma_G^2}\right)^{-1} , \tag{5.35}$$

which provides the upper performance bound of the optimum detector in Gaussian noise. However, in the presence of impulse noise, we observe in (5.19) that the optimum detector modifies the decision boundaries according to the noise states of received impulse noise vector $\mathbf{z}$. In the one hand, when the noise states of z_n, $n = 0, \cdots, N-1$, are identical, i.e., $\mathbf{\Sigma_z} = \sigma_m^2 \mathbf{I}_N$, the decision boundaries reduce to a set of linear equations as in Fig. 5.2 for $N = 2$. On the other hand, when the noise states are not identical, the optimum decision boundaries illustrate an affine hyperplane to cope with the effects of impulse noise. In Fig. 5.3, we depict the decision boundaries given in (5.19) for a two-dimensional received signal, $\mathbf{y} = [y_0\ y_1]^T$, corrupted by impulse noise. Figures 5.3a and 5.3b, show the decision boundaries of the received signal corrupted by impulse noise with the noise states $[m_0 = 1, m_1 = 0]$ and $[m_0 = 0, m_1 = 1]$, respectively. We observe that the probability of error is dominated by the PEPs of lattice points that fall on the direction of impulse noise. Thus, considering only the nearest-neighbor lattice points will not be correct for the upper performance bound in the presence of impulse noise. In (5.32), we note that $P(\mathbf{x}_i \to \mathbf{x}_j)$ is directly proportional to

$$G(\mathbf{x}_i, \mathbf{x}_j) = \sum_{m_0=0}^{\infty} \cdots \sum_{m_{N-1}=0}^{\infty} \frac{4 \prod_{n=0}^{N-1} \alpha_{m_n}}{d^2(\mathbf{x}_i, \mathbf{x}_j, m_n)} . \tag{5.36}$$

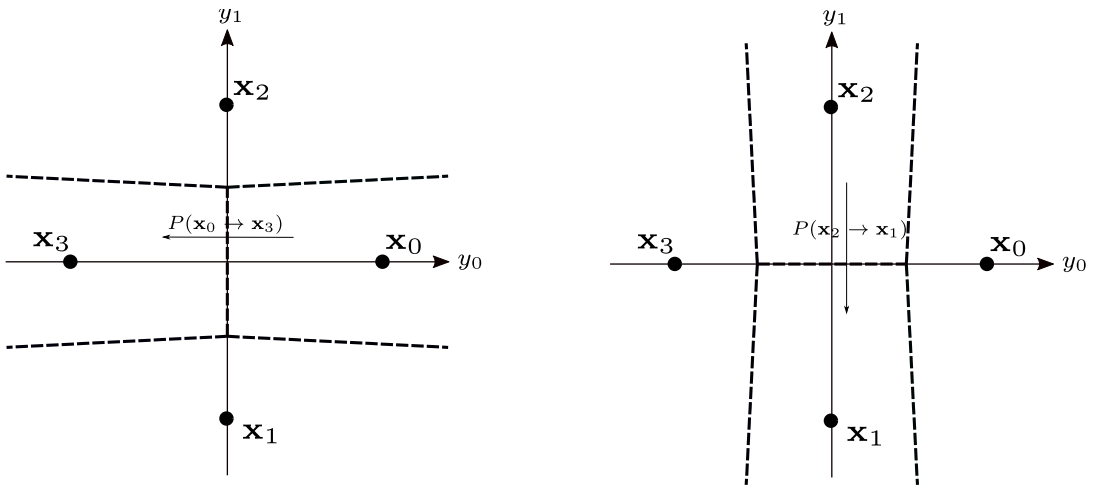

(a) $m_0 = 1$ and $m_1 = 0$ (b) $m_0 = 0$ and $m_1 = 1$

Figure 5.3: Decision boundaries of the optimum detector in impulse noise with two different noise states and $\sigma_1^2 = 20\sigma_0^2$

The probability of error of the optimum detector in impulse noise is upper-bounded by summing the PEPs of maximum $G(\mathbf{x}_i, \mathbf{x}_j)$, $\forall i$ and $\forall j$, as

$$P_e < \left(\frac{E_b}{\sigma_G^2}\right)^{-1} \overbrace{\frac{1}{2^N} \sum_{i=0}^{2^{N-1}} \sum_{\substack{j=1 \\ j \neq i}}^{M_i} \frac{n_d(i,j)}{N} G_{\max}(\mathbf{x}_i, \mathbf{x}_j)}^{G_{MC}} , \tag{5.37}$$

where $G_{\max}(\mathbf{x}_i, \mathbf{x}_j)$ represents the maximum value of (5.36), $\forall i$ and $\forall j$. M_i is the number of lattice points of maximum $G(\mathbf{x}_i, \mathbf{x}_j)$ for the point $\mathbf{x}_i$. To investigate the probability of error for different number of subcarriers N, we first consider a single-carrier case. For $N = 1$, the expression in (5.37) reduces to

$$\begin{aligned} P_e &< \left(\frac{E_b}{\sigma_G^2}\right)^{-1} \sum_{m_0=0}^{\infty} \alpha_{m_0} \left(1 + \frac{m_0}{A\Upsilon}\right) , \\ &< \left(\frac{E_b}{\sigma_G^2}\right)^{-1} \overbrace{\left(1 + \frac{1}{\Upsilon}\right)}^{G_{MC}} . \end{aligned} \tag{5.38}$$

The single-carrier systems in impulse noise is limited by a factor $G_{MC} = (1 + \frac{1}{\Upsilon})$, which increases as Υ decreases. For $N = 2$, we observe in Fig. 5.3 that the probability of error is dominated by $P(\mathbf{x}_0 \to \mathbf{x}_3)$ and $P(\mathbf{x}_2 \to \mathbf{x}_1)$ due to the presence of impulse noise. Since

$d^2(\mathbf{x}_0, \mathbf{x}_3, m_n) = 8/(1 + \frac{m_0}{A\Upsilon})$ and $n_d(0, 3) = 2$, (5.37) can be rewritten as

$$P_e < \left(\frac{E_b}{\sigma_G^2}\right)^{-1} \sum_{m_0=0}^{\infty} \sum_{m_1=0}^{\infty} \frac{4\alpha_{m_0}\alpha_{m_1}}{8/\left(1 + \frac{m_0}{A\Upsilon}\right)},$$
$$< \left(\frac{E_b}{\sigma_G^2}\right)^{-1} \overbrace{\frac{\left(1 + \frac{1}{\Upsilon}\right)}{2}}^{G_{MC}}. \tag{5.39}$$

This result shows that the performance loss, G_{MC}, is reduced by a factor of 2. However, in the case of OFDM systems with $N > 2$, it is not clear how the performance loss, G_{MC}, is reduced as N increases. To assess the performance improvements of the optimum detector in different impulse noise environments, we used a Monte Carlo simulation to compute G_{MC} at various number of subcarriers. In Fig. 5.4, we illustrate G_{MC} versus the number of subcarriers, N, for MCA noise with different A and $\Upsilon = 0.01$. Additionally,

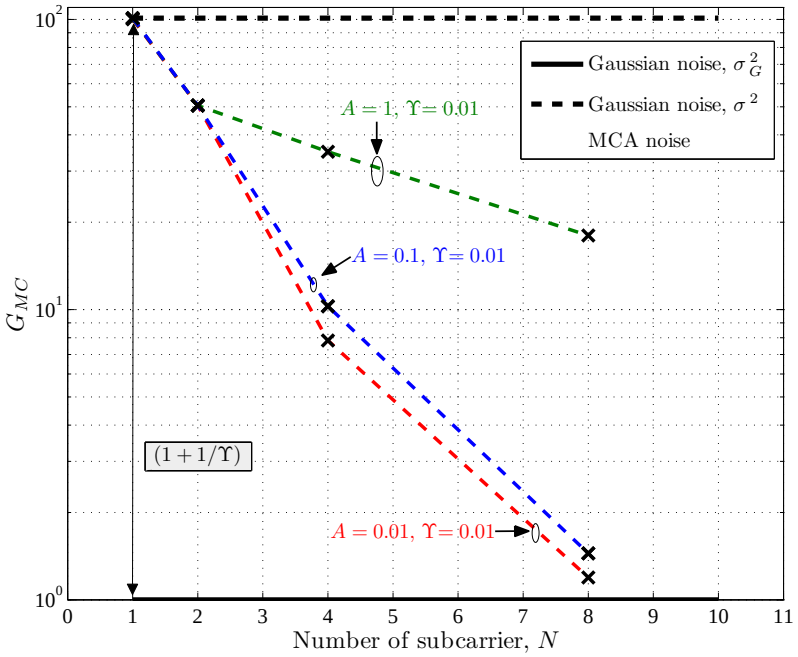

Figure 5.4: G_{MC} versus the number of subcarriers for MCA noise with different A

we depict the single-carrier limits in Gaussian noise with σ_G^2 and $\sigma^2 = \sigma_G^2(1 + \frac{1}{\Upsilon})$ as references. The shown results indicate that the optimum detector of multicarrier systems yields a significant reduction in G_{MC} as N increases. Furthermore, we note that G_{MC} obtained for impulse noise with equal Gaussian factors, Υ, reduces significantly as the average rate of impulses, A, decreases. To examine the performance improvement of the optimum multicarrier detector in different conditions of impulse noise, we compute G_{MC} versus N for impulse noise with various Gaussian factors. The results of the simulation

are depicted in Fig. 5.5 for impulse noise environments with $A = 0.1$ and different Υ. The shown results state an interesting point of the optimum detector for the multicarrier

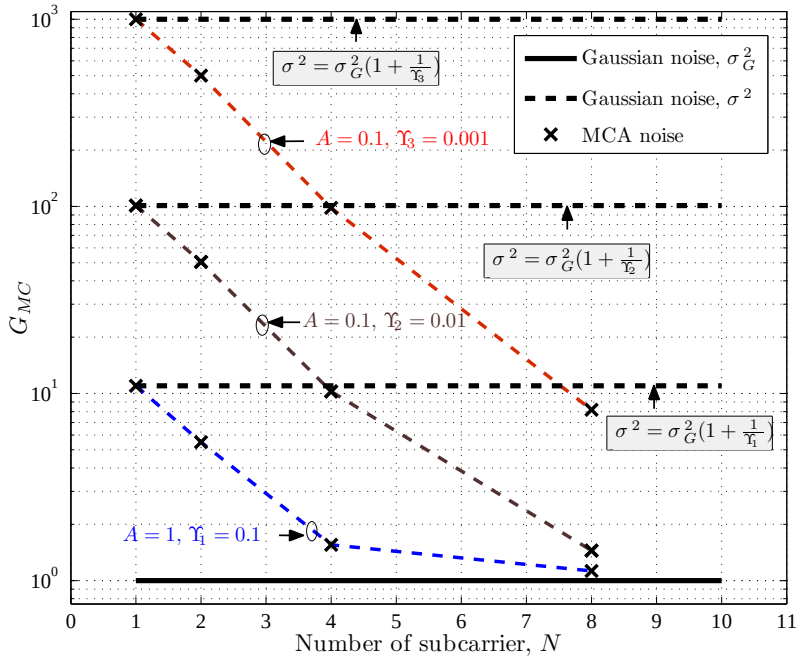

Figure 5.5: G_{MC} versus the number of subcarriers for MCA noise with different Υ

systems in strong impulse noise. We observe that the optimum detector in impulse noise with $\Upsilon = 0.001$ reduces the loss factor from 10^3 to 10 at for $N = 8$. In addition, we note that G_{MC} approaches the impulse-free limit as Υ increases.

5.3 Optimum Detector Using Lattice Decoding

In the previous analysis, we showed how the optimum detector utilizes the lattice structure of the OFDM symbols (in time domain) to minimize the performance loss as the number of subcarriers increases. Herewith, we take a first step towards a practical realization of the optimum detector of OFDM signals in MCA noise.

5.3.1 Lattice Sphere Decoding

We observe from (5.7) that the optimum decision rule is equivalent to finding the closest lattice point to a received point $\mathbf{L}^H\mathbf{y}$. Thus, the lattice decoder [54] can be used to realize the implementation of the optimum detector under perfect knowledge of the NSI. The lattice decoder searches over all possible lattice points that lie within a sphere of radius

β_0 around the received point $\mathbf{L}^H\mathbf{y}$. The sphere equation of the optimum detector can be expressed as

$$\left|\mathbf{L}^H\mathbf{y} - \mathbf{G}\mathbf{s}\right|^2 \leq \beta_0 \,, \tag{5.40}$$

where $\mathbf{G} = \sqrt{E_b}\mathbf{L}^H\bar{\mathbf{H}}\mathbf{W}_N^H$. The sphere equation in (5.40) requires perfect knowledge of the noise states m_n, $n = 0, \cdots, N-1$, to compute $\mathbf{\Sigma}_\mathbf{z}^{-1} = \mathbf{L}\mathbf{L}^H$. Thus, we first use perfect estimate of $\mathbf{\Sigma}_\mathbf{z}$ to realize the performance improvements of the optimum detector. Using a QR decomposition, the matrix $\mathbf{G}$ can be factorized into a product of a unitary matrix $\mathbf{Q}$ and an upper triangular matrix $\mathbf{R}$. Thus, (5.40) reduces to

$$\begin{aligned} \left|\mathbf{L}^H\mathbf{y} - \mathbf{Q}\mathbf{R}\mathbf{s}\right|^2 &\leq \beta_0 \,, \\ \left|\mathbf{Q}^H\mathbf{L}^H\mathbf{y} - \mathbf{Q}^H\mathbf{Q}\mathbf{R}\mathbf{s}\right|^2 &\leq \beta_0 \,, \\ \left|\mathbf{y}' - \mathbf{R}\mathbf{s}\right|^2 &\leq \beta_0 \,, \end{aligned} \tag{5.41}$$

which is equivalent to solving the following linear least squares problem

$$\sum_{j=n}^{N-1} \left| y_j' - \textstyle\sum_{i=j}^{N-1} R_{j,i}s_i \right|^2 \leq \beta_0 \,, \quad n = 0, \cdots, N-1 \,, \tag{5.42}$$

which is the typical problem of the lattice (sphere) decoder for finding the closest signal vector that satisfies the above set of conditions in the order from $n = N-1$ to $n = 0$. The searching algorithms of the lattice decoder can be implemented sequentially as in [54, 55], or concurrently as in [56,57]. In the simulation results, we examine the performance of the K-best algorithm [56, 57] of lattice decoding for multicarrier systems in impulse noise. As an illustration of the performance improvements of the optimum detector for multicarrier systems in the presence of impulsive interference. Figures 5.6, 5.7, and 5.8 depict the BER of the lattice decoder for BPSK-OFDM signals in a Rayleigh flat fading channel and MCA noise with $A = 1$, $A = 0.1$, and $A = 0.01$, respectively. For comparison, the performances obtained for a channel with Gaussian noise are also depicted as references. In Fig. 5.6, we observe that the results obtained for MCA noise with $A = 1$ and $\Upsilon = 0.01$ improve as the number of subcarriers, N, increases. However, in moderate and strong impulse noise, figures. 5.7 and 5.8 show that the optimum detector approaches the impulse-free limit as N increases, which is in agreement with the results obtained in Fig. 5.4.

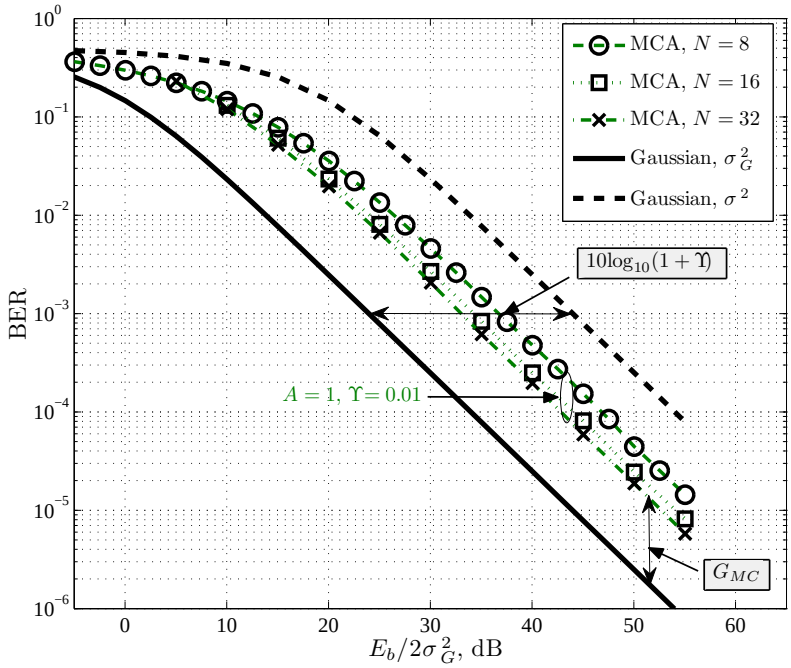

Figure 5.6: The BER Performance of the sphere decoder for an BPSK-OFDM system in MCA noise with $A = 1$ and $\Upsilon = 0.01$

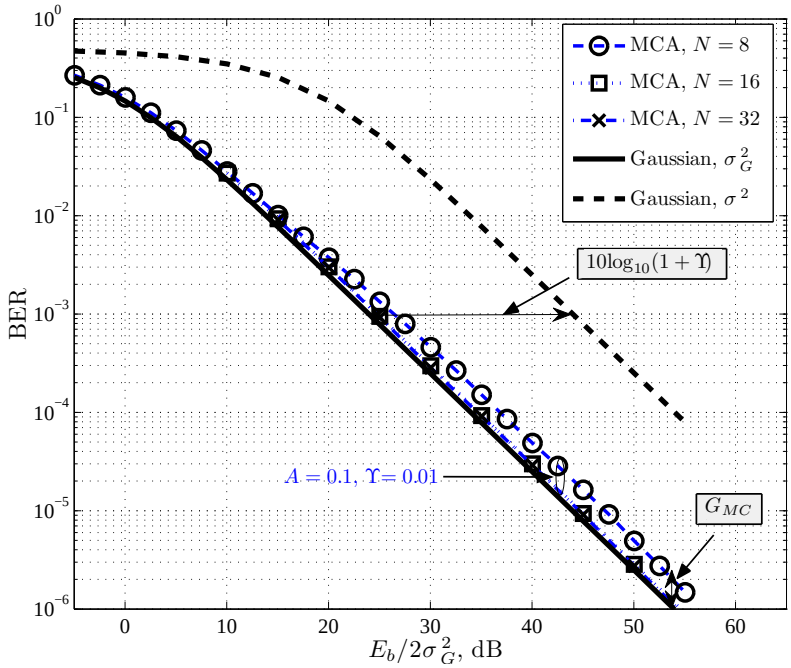

Figure 5.7: The BER Performance of the sphere decoder for an BPSK-OFDM system in MCA noise with $A = 0.1$ and $\Upsilon = 0.01$

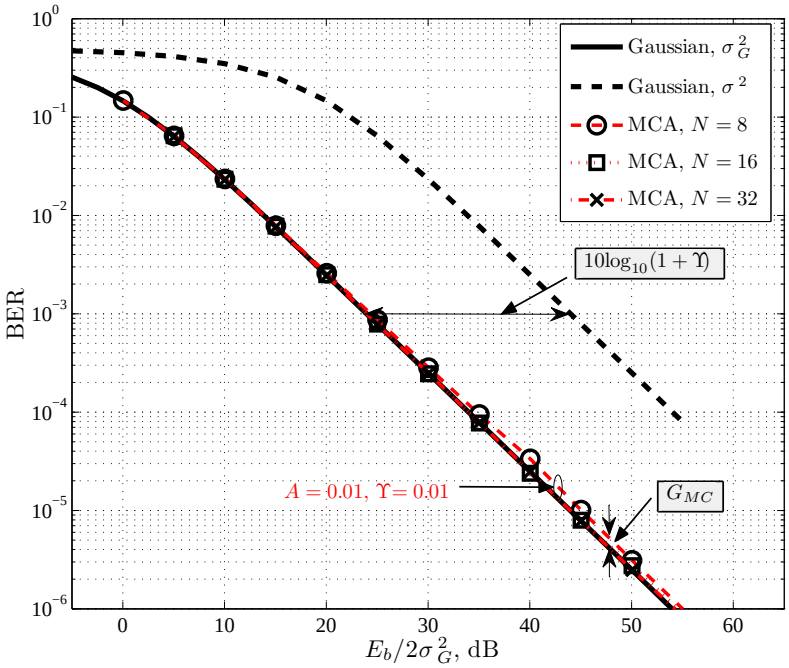

Figure 5.8: The BER Performance of the sphere decoder for an BPSK-OFDM system in MCA noise with $A = 0.01$ and $\Upsilon = 0.01$

5.3.2 Noise Covariance Estimation

The results of the previous subsection assume perfect knowledge of the impulse noise covariance matrix $\Sigma_{\mathbf{z}}$. To realize this assumption, we develop a sparse Bayesian learning (SBL) scheme [43, 44] with the lattice decoder for multicarrier systems in the presence of impulse noise. SBL treats impulse noise as a random sparse signal corrupted by Gaussian noise, which provides a reliable estimate of noise locations as well as noise amplitudes. Figure 5.9 illustrates a receiver structure of multicarrier systems in impulse noise using lattice decoding and SBL. We consider the N subcarriers consisting of null subcarriers

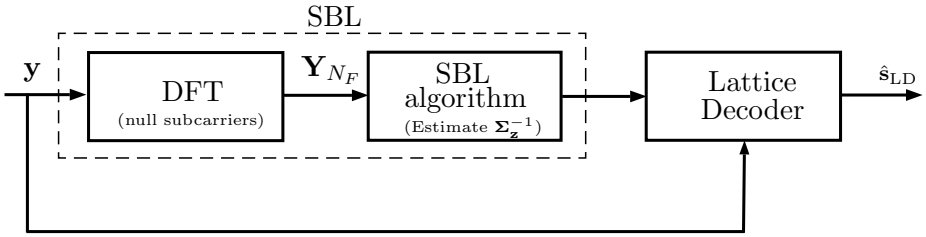

Figure 5.9: A receiver structure of multicarrier systems using lattice decoding and the SBL scheme

and data subcarriers. Since the received noise vector $\mathbf{z}$ has two noise components $\mathbf{z}_I$ and

$\mathbf{z}_G$, the received signal on the null subcarriers (after the DFT operation) can be given as

$$\mathbf{Y}_{N_F} = \mathbf{W}_{N_F}\mathbf{z}_I + \mathbf{V} \ , \tag{5.43}$$

where N_F is the number of null subcarriers. $\mathbf{W}_{N_F}$ is an $N_F \times N$ submatrix of $\mathbf{W}_N$ formed by selecting the rows of the null signal subspace. $\mathbf{V} = \mathbf{W}_{N_F}\mathbf{z}_G$ is an $N_F \times 1$ Gaussian noise vector with zero mean and variance σ_G^2. Then, the conditional PDF of $\mathbf{Y}_{N_f}$ given $\mathbf{z}_I$ can be expressed as

$$p(\mathbf{Y}_{N_F}|\mathbf{z}_I) = \frac{1}{(2\pi\sigma_G^2)^{N_F}} e^{-\frac{1}{2}\frac{\left(\mathbf{Y}_{N_F}-\mathbf{W}_{N_F}\mathbf{z}_I\right)^H\left(\mathbf{Y}_{N_F}-\mathbf{W}_{N_F}\mathbf{z}_I\right)}{2\sigma_G^2}} \ . \tag{5.44}$$

For MCA noise, the entries of the impulse noise vector, $\mathbf{z}_I$, are Gaussian with zero mean and variance $\frac{m_n/A}{1+\Upsilon}\sigma_G^2$, $n = 0, \cdots, N-1$. Thus, the prior distribution of $\mathbf{z}_I$ can be given as

$$p(\mathbf{z}_I) = \frac{1}{(2\pi)^N|\mathbf{\Sigma}_{\mathbf{z}_I}|} e^{-\frac{1}{2}\mathbf{z}_I^H\mathbf{\Sigma}_{\mathbf{z}_I}^{-1}\mathbf{z}_I} \ , \tag{5.45}$$

where the covariance matrix $\mathbf{\Sigma}_{\mathbf{z}_I}$ is diagonal. Indeed, the diagonal elements of $\mathbf{\Sigma}_{\mathbf{z}_I}$ are the variances of the elements of $\mathbf{z}_I$. According to [43, 44], the nonzero variances indicate to the presence of impulse noise. From (5.44) and (5.45), the distribution of $\mathbf{Y}_{N_F}$ is

$$\begin{aligned} p(\mathbf{Y}_{N_F}) &= \int p(\mathbf{Y}_{N_F}|\mathbf{z}_I)p(\mathbf{z}_I)d\mathbf{z}_I \ , \\ &= \frac{1}{(2\pi)^{N_F}|\mathbf{\Sigma}_{\mathbf{Y}_{N_F}}|} e^{-\frac{1}{2}\mathbf{Y}_{N_F}^H\mathbf{\Sigma}_{\mathbf{Y}_{N_F}}^{-1}\mathbf{Y}_{N_F}} \ , \end{aligned} \tag{5.46}$$

where $\mathbf{\Sigma}_{\mathbf{Y}_{N_F}} = \sigma_G^2\mathbf{I}_{N_F} + \mathbf{W}_{N_F}\mathbf{\Sigma}_{\mathbf{z}_I}\mathbf{W}_{N_F}^H$. Using Bayes' rule, the posterior probability of $\mathbf{z}_I$ can be computed as

$$\begin{aligned} p(\mathbf{z}_I|\mathbf{Y}_{N_F}) &= \frac{p(\mathbf{Y}_{N_F}|\mathbf{z}_I)p(\mathbf{z}_I)}{p(\mathbf{Y}_{N_F})} \ , \\ &= \frac{1}{(2\pi)^N|\mathbf{\Sigma}|} e^{-\frac{1}{2}(\mathbf{z}_I-\boldsymbol{\mu}_I)^H\mathbf{\Sigma}^{-1}(\mathbf{z}_I-\boldsymbol{\mu}_I)} \ , \end{aligned} \tag{5.47}$$

where

$$\mathbf{\Sigma} = \left(\frac{1}{\sigma_G^2}\mathbf{W}_{N_F}^H\mathbf{W}_{N_F} + \mathbf{\Sigma}_I^{-1}\right)^{-1} \ , \tag{5.48}$$

and

$$\boldsymbol{\mu}_I = \frac{1}{\sigma_G^2}\mathbf{\Sigma}\mathbf{W}_{N_F}^H\mathbf{Y}_{N_F} \ , \tag{5.49}$$

are the posterior covariance and mean, respectively. We follow the SBL scheme in [43] to estimate $\mathbf{\Sigma}_I$ that maximizes $\log\left(p(\mathbf{Y}_{N_F})\right)$ as follows:

$$\mathbf{\Sigma}_I = \mathbf{\Sigma} + \boldsymbol{\mu}_I \boldsymbol{\mu}_I^H \ . \tag{5.50}$$

The learning algorithm of the SBL scheme starts with an initial value of $\mathbf{\Sigma}_I$ to compute the updates of the posterior statistics $\mathbf{\Sigma}$ and $\boldsymbol{\mu}_I$ from (5.48) and (5.48), respectively. The algorithm converges within a few iterations. Upon convergence, the current values of $\boldsymbol{\mu}_I$ and $\mathbf{\Sigma}_I$ yields an estimate of the sparse vector $\mathbf{z}_I$ and the covariance matrix $\mathbf{\Sigma}_I$, respectively. Therefore, the estimate of the covariance matrix $\mathbf{\Sigma}_\mathbf{z}$ can be given by $\sigma_G^2 \mathbf{I}_N + \mathbf{\Sigma}_I$. In the simulation results, we investigate the SBL algorithm with the sphere decoder for multicarrier systems in impulse noise. We assume a BPSK-OFDM system with $N = 64$ in the presence of MCA noise with $A = 0.1$ and 0.01. Since the SBL algorithm requires a set of null subcarriers, we limit the data subcarriers to 32 subcarriers. The SBL algorithm with two different numbers of nulled subcarriers is used, i.e., $N_F = 24$ and 32. For the purposes of comparison, we simulated the performances of a conventional OFDM detector in the same impulse noise environments. Figure 5.10 depicts the BER of the conventional OFDM detector and the sphere decoder employing the SBL algorithm for estimating impulse noise variances in a flat fading channel. Additionally, we illustrate

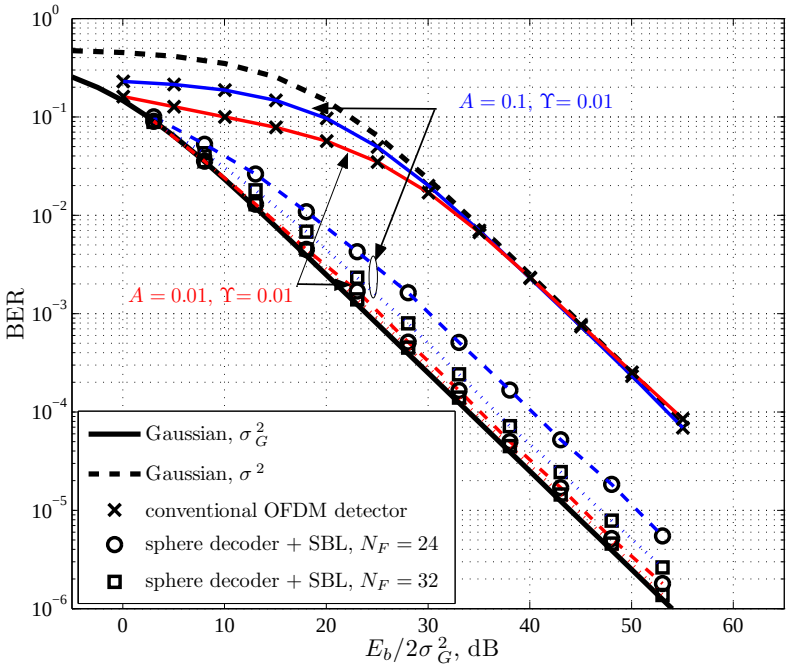

Figure 5.10: The BER Performance of a sphere decoder employing the SBL scheme for estimating impulse noise variances

the performance of the impulse-free channel as a reference. From this figure, we observe

that the SBL scheme with a sphere decoder provides much better performance than the conventional OFDM detector. In addition, we note that the SBL scheme with $N_F = 32$ improves the performance of the sphere decoder more than with $N_F = 24$. This was expected, since increasing N_F improves the estimates of noise variances $\mathbf{\Sigma_z}$. This improvement increases significantly when the noise becomes more sparse (decreasing A).

5.4 Conclusion

In this chapter, we considered different detection schemes for multicarrier systems in the presence of MCA noise. We investigated the optimum detector as well as the suboptimum detectors such as a conventional OFDM detector and a minimum mean square error detector. Under perfect knowledge of the NSI, we derived the upper performance bound of the optimum detector in impulse noise. The performance analysis showed that the performance loss due to impulse noise reduces significantly with the number of subcarriers. Therefore, we developed a lattice decoder to realize the optimum multicarrier detector in impulse noise. We further investigated the SBL scheme for estimating the NSI of MCA noise using null subcarriers. The simulation results showed that the lattice decoder with the SBL scheme approaches the impulse-free limit as the number of null subcarriers increases.

Chapter 6

Concluding Remarks

In this thesis, we have investigated modern detection schemes for binary signaling in fading channels with impulse noise. In particular, we provided a simple representation of a Middleton Class-A (MCA) model for impulse noise. This representation leads to suitable approximations of the optimum detection by determining noise states (Gaussian or impulsive) at the receiver. Diversity techniques were also considered, and the approximate MCA representation played an important role in finding and analyzing the optimum schemes for wireless communication systems utilizing time and space diversity. We also provided the optimum receiver design of orthogonal frequency division multiplexing (OFDM) systems in impulse noise. We found analytically that the OFDM system employing the optimum receiver appears to be the most effective method for significantly combating the effects of impulse noise.

The first portion of this work concentrated on analyzing and verifying the statistical properties of the MCA model for wireless impulse noise. Since MCA noise is characterized by very short pulses, we showed that temporal characteristics of impulse noise are dominated by the impulse response of a passband filter. Additionally, we presented a multivariate MCA distribution to model the spatial property of impulse noise for multi-antenna systems. The measurement results showed that the wireless interference at a 2.4 GHz band possesses the impulsive character of MCA noise. We observed that a few first terms of the MCA distribution are sufficient to fit the voltage histograms of the measured data. For multi-antenna systems, we verified the multivariate MCA distribution in modeling the received interference at different receive antennas. The measurements showed that the spatial properties of the received interference are in accordance with a correlated multivariate model of MCA noise with unequal Gaussian factors.

Second, we considered an optimum detection approach of binary signals corrupted by MCA noise. We introduced a simplified MCA model to derive a closed-form approximation of nonlinear operations of the optimum detector. The simplified MCA model uses a threshold detection scheme to determine the noise states of impulse noise. We observed that the optimum detector applies two different nonlinearities on the received signal observations according to signal levels with respect to a detection threshold of impulse noise. Thus, at a low signal-to-noise ratio (SNR), we showed that the optimum nonlinearities provide an impulse-free performance as the number of observations increases. However, at a high SNR, the performance of the optimum detector approaches the one of a linear detector in impulse noise. For two received observations, we used the simplified MCA model to introduce a decision boundary evaluation of the optimum detector in MCA noise. This investigation explains the nonlinearity behaviors the optimum detector in different impulse noise environments. We further used the approximate nonlinearities to evaluate the operations of suboptimum nonlinearities such a locally optimum and a clipping nonlinearity. We then studied a linear approximation of the optimum nonlinearities, which introduces new suboptimum detectors such as a piecewise linear detector and a clipping-like detector. The simulation results showed that the proposed approximations provide a near performance to the optimum detector for different impulse noise environments.

In the third part, we investigated time and space diversity techniques for wireless communication systems in the presence of fading and impulse noise. Under perfect knowledge of noise states, we analytically evaluated an upper performance bound of the optimum detectors for time and spatial diversity in Rayleigh fading and MCA noise. At high SNRs, we showed that the performance of the optimum detector for time diversity is limited by the Gaussian factor (a ratio of Gaussian noise power to impulse noise power) of impulse noise. However, the asymptotic performance of the optimum detector for receive diversity is further limited by the impulsive index (average rate of impulses) of MCA noise. Moreover, for transmit/receive diversity, we showed that the performance limitation of orthogonal space-time block coding (OSBTC) increases significantly with the numbers of transmit and receive antennas. To realize the assumption of perfect noise state information (NSI), we applied the herein simplified MCA model to provide a closed-form approximation of the optimum detection method for time diversity, receive diversity, and OSTBC schemes. Simulation results showed that the performance of the approximate optimum detectors approach the optimum one for different environments of impulse noise.

Lastly, we investigated the optimum receiver design for multicarrier systems in fading

and MCA noise. Under perfect knowledge of the NSI, we showed that the optimum detector of OFDM signals reduces to a lattice decoder. The performance analysis of the optimum detector with perfect NSI showed that the performance limitation of OFDM signals in impulse noise is reduced significantly with increasing the number of subcarriers. In particular, the performances approach the impulse-free limit for impulse noise with a small rate of impulses. This differs from the time and space diversity schemes whose performances are limited by the impulsive index and the Gaussian factor of MCA noise. To realize the NSI at the receiver, we investigated sparse Bayesian learning (SBL) to estimate the noise states using a set of nulling subcarriers. We then proposed a sphere decoding with SBL to realize the optimum OFDM receiver. The presented simulation results showed that the proposed implementation approaches the optimum performance as the number of nulling subcarriers increases.

List of Mathematical Symbols

A	impulsive index of MCA noise
$\mathbf{C}$	space-time code matrix
$\mathbf{c}_{n_D}$	n_D^{th} column vector of $\mathbf{C}$
d_0	threshold for discriminating impulse noise and Gaussian noise
d_1	threshold for discriminating the noise states of baseband impulse noise
$g(\cdot)$	optimum nonlinearity operation
$\mathbf{H}$	MIMO channel matrix
$\bar{\mathbf{H}}$	circulant convolution channel matrix
h_{n_D}	fading coefficient for the n_D^{th} time slot
$\mathbf{h}_{n_R}$	fading coefficient for the n_R^{th} receive antenna
$\bar{\mathbf{h}}$	first column vector of $\bar{\mathbf{H}}$
m	noise state information
N	number of received observations
N_D	number of time slots
N_R	number of receive antennas
N_T	number of transmit antennas
N_F	number of nulled subcarriers
P_e	error probability
$p_w(w)$	probability density function of real impulse noise
$p_z(z)$	probability density function of complex impulse noise
$\mathbf{\Sigma}_m$	covariance matrix of MCA noise for the m^{th} noise state
σ_G^2	variance of Gaussian noise
σ_I^2	variance of impulse noise
σ^2	average noise variance of an MCA model
σ_m^2	noise variance of the m^{th} noise state
Υ	Gaussian factor of an MCA model
$\mathbf{W}_N^H$	inverse DFT matrix
$\mathbf{W}_N$	DFT matrix
$w(t)$	passband impulse noise process
$\mathbf{x}$	OFDM symbol
$\mathbf{Y}$	received vector after a DFT operation
y_k	k^{th} received observation
$\mathbf{y}_{n_D}$	received signal for the n_D^{th} time slot
$\mathbf{y}_{n_R}$	received signal for the n_R^{th} receive antenna

$z(t)$	baseband impulse noise process
$\mathbf{z}_{n_D}$	noise vector for the n_D^{th} time slot
$\mathbf{z}_{n_R}$	noise vector for the n_R^{th} receive antenna

List of Acronyms

AWGN	additive white Gaussian noise
BER	bit-error ratio
BPF	bandpass filter
BPSK	binary phase shift keying
CCDF	complementary cumulative distribution function
CP	cyclic prefix
DFT	discrete-Fourier transform
IDFT	inverse discrete-Fourier transform
IF	intermediate frequency
ISM	industrial, scientific, and medical
LAN	local area network
LLR	log-likelihood ratio
LO	local oscillator
LOD	locally optimum detector
MCA	Middleton Class-A
MD	minimum distance
MIMO	multiple-input multiple-output
MISO	multiple-input single-output
ML	maximum-likelihood
MMSE	minimum mean-square error
MRC	maximum ratio combining
NSI	noise state information
OFDM	orthogonal frequency division multiplexing
OSTBC	orthogonal space-time block coding
PDF	probability density function
PEP	pairwise error probability
QAM	quadrature amplitude modulation
RFI	radio frequency interference
SBL	Sparse Bayesian learning
SINR	Signal-to-interference-plus-noise ratio
SNR	signal-to-noise ratio
ST	space-time
SαS	symmetric alpha-stable
ZF	zero-forcing

Own Publications

- Oana Graur, K. A. Saaifan, Thejani Fernando, and W. Henkel, "Impulse noise in DSL, powerline, and wireless," in *ITG Fachgruppe Angewandte Informationstheorie*, Darmstadt, Germany, April 2014.

- K. A. Saaifan and W. Henkel, "A nonlinear diversity combiner of binary signals in the presence of impulsive interference," in *IEEE International Conference on Communications (ICC)*, Budapest, Hungary, June 2013.

- K. A. Saaifan and W. Henkel, "Decision boundary evaluation of optimum and suboptimum detectors in Class-A interference," *IEEE Transactions on Communications*, vol. 61, no. 1, pp. 197-205, January 2013.

- K. A. Saaifan and W. Henkel, "A receiver design for MIMO systems over Rayleigh fading channels with correlated impulse noise," in *IEEE Global Communications Conference (GLOBECOM)*, Anaheim, CA, USA, December 2012.

- K. A. Saaifan and W. Henkel, "Efficient nonlinear detector of binary signals in Rayleigh fading and impulsive interference," in *IEEE Vehicular Technology Conference (VTC Fall)*, Quebec City, Canada, September 2012.

- K. A. Saaifan and W. Henkel, "A spatial diversity reception of binary signal transmission over Rayleigh fading channels with correlated impulse noise," in *19th International Conference on Telecommunications (ICT)*, Jounieh, Lebanon, April 2012.

- K. A. Saaifan and W. Henkel, "A linear piecewise suboptimum detector for signals in Class-A noise," in *8th International Symposium on Wireless Communication Systems (ISWCS)*, Aachen, Germany, November 2011.

- K. A. Saaifan and W. Henkel, "Pulsed interference cancellation based on unused spatial dimensions and lattice signal sets," in *16th International OFDM-Workshop*, Hamburg, Germany, August 2011.

- K. A. Saaifan and W. Henkel, "Lattice signal sets to combat pulsed interference from aeronautical signals," in *IEEE International Conference on Communications (ICC)*, Kyoto, Japan, June 2011.

Bibliography

[1] D. Middleton, "Statistical-physical models of electromagnetic interference," *IEEE Transactions on Electromagnetic Compatiability*, vol. EMC-19, no. 3, pp. 106–127, August 1977.

[2] ——, "Non-Gaussian noise models in signal processing for telecommunications: new methods and results for Class-A and Class-B noise models," *IEEE Transactions on Information Theory*, vol. 45, no. 4, pp. 1129–1149, May 1999.

[3] X. Yang and A. Petropulu, "Co-channel interference modeling and analysis in a Poisson field of interferers in wireless communications," *IEEE Transactions on Signal Processing*, vol. 51, no. 1, pp. 64–76, January 2003.

[4] K. Blackard, T. Rappaport, and C. Bostian, "Measurements and models of radio frequency impulsive noise for indoor wireless communications," *IEEE Journal on Selected Areas in Communications*, vol. 11, no. 7, pp. 991–1001, September 1993.

[5] M. Sanchez, L. deHaro, M. Ramon, A. Mansilla, C. M. Ortega, and D. Oliver, "Impulsive noise measurements and characterization in a UHF digital TV channel," *IEEE Transactions on Electromagnetic Compatibility*, vol. 41, no. 2, pp. 124–136, May 1999.

[6] M. Nassar, K. Gulati, M. DeYoung, B. Evans, and K. Tinsley, "Mitigating near-field interference in laptop embedded wireless transceivers," *IEEE International Conference on Acoustics, Speech and Signal Processing*, pp. 1405–1408, March 2008.

[7] K. Gulati, B. Evans, J. Andrews, and K. Tinsley, "Statistics of co-channel interference in a field of Poisson and Poisson-Poisson clustered interferers," *IEEE Transactions on Signal Processing*, September 2010.

[8] S. Brandes, S. Gligorevic, M. Ehammer, T. Gräupl, C. H. Rokitansky, R. Dittrich, M. Schnell, and C. Rihacek, "Expected B-AMC system performance," DLR, Tech. Report, 2007.

[9] M. Schnell, S. Brandes, S. Gligorevic, C. Rokitansky, M. Ehammer, T. Gräupl, C. Rihacek, and M. Sajatovic, "B-AMC broadband aeronautical multicarrier communications," *8th Integrated Communications, Navigation, and Surveillance Conference*, September 2007.

[10] K. A. Saaifan and W. Henkel, "Pulsed interference cancellation based on unused spatial dimensions and lattice signal sets," in *16th International OFDM-Workshop*, Hamburg, Germany, August 2011.

[11] ——, "Lattice signal sets to combat pulsed interference from aeronautical signals," in *IEEE International Conference on Communications (ICC)*, Kyoto, Japan, June 2011.

[12] C. Nikias and M. Shao, *Signal processing with alpha-stable distributions and applications*. Jon Wiley, 1995.

[13] H. Inaltekin, S. B. Wicker, M. Chiang, and H. V. Poor, "On unbounded path-loss models: effects of singularity on wireless network performance," *IEEE Journal on Selected Areas in Communications*, vol. 27, no. 7, pp. 1078–1092, September 2009.

[14] A. Spaulding and D. Middleton, "Optimum reception in an impulsive interference environment-part I: coherent detection," *IEEE Transactions on Communications*, vol. 25, no. 9, pp. 910–923, September 1977.

[15] S. Rappaport and L. Kurz, "An optimal nonlinear detector for digital data transmission through non-Gaussian channels," *IEEE Transactions on Communication Technology*, vol. 14, no. 3, pp. 266–274, June 1966.

[16] K. S. Vastola, "Threshold detection in narrow-band non-Gaussian noise," *IEEE Transactions on Communications*, vol. 32, no. 2, pp. 134–139, February 1984.

[17] S. Miyamoto, M. Katayama, and N. Morinaga, "Optimum detection and design of TCM signals under impulsive noise environment," in *IEEE International Conference on Systems Engineering*, Kobe, Japan, September 1992.

[18] P. Gao and C. Tepedelenlioglu, "Space-time coding over fading channels with impulsive noise," *IEEE Transactions on Wireless Communications*, vol. 6, no. 1, pp. 220–229, January 2007.

[19] C. Tepedelenlioglu and P. Gao, "On diversity reception over fading channels with impulsive noise," *IEEE Transactions on Vehicular Technology*, vol. 54, no. 6, pp. 2037–2047, 2005.

[20] D. Middleton, "Canonical and quasi-canonical probability models of Class-A interference," *IEEE Transactions on Electromagnetic Compatiability*, vol. EMC-25, no. 2, pp. 76–106, May 1983.

[21] L. Berry, "Understanding Middleton's canonical formula for Class-A noise," *IEEE Transactions on Electromagnetic Compatiability*, vol. EMC-23, no. 4, pp. 337–344, november 1981.

[22] H. Zhan, J.-Y. L. Boudec, J. Farserotu, and J. Ayadi, "Statistical analysis of impulse radio ultra-wideband multi-user interference based on measurments," in *IEEE International Conference on Ultra-Wideband (ICUWB)*, vol. 3, 2008, pp. 189–192.

[23] K. Furutsu and T. Ishida, "On the theory of amplitude distributions of impulsive random noise," *Journal of Applied Physics*, vol. 32, no. 7, pp. 1206–1221, 1961.

[24] J. Ilow and D. Hatzinakos, "Analytic alpha-stable noise modeling in a Poisson field of interferers or scatterers," *IEEE Transactions on Signal Processing*, vol. 46, no. 6, pp. 1601–1611, June 1998.

[25] R. Blum, R. Kozick, and B. Sadler, "An adaptive spatial diversity receiver for non-Gaussian interference and noise," *IEEE Transactions on Signal Processing*, vol. 47, no. 8, pp. 2100–2111, August 1999.

[26] E. Kuruoglu, W. Fitzgerald, and P. Rayner, "Near optimal detection of signals in impulsive noise modeled with a symmetric α-stable distribution," *IEEE Communications Letters*, vol. 2, no. 10, pp. 282–284, October 1998.

[27] J. Miller and J. Thomas, "The detection of signals in impulsive noise modeled as a mixture process," *IEEE Transactions on Communications*, vol. 24, no. 5, pp. 559–563, May 1976.

[28] D. Andrews and C. Mallows, "Scale mixtures of normal distributions," *Journal of the Royal Statistical Society, Series B*, vol. B-36, pp. 99–102, 1974.

[29] A. Ayyar, M. Lentmaier, K. Giridhar, and G. Fettweis, "Robust initial LLRs for iterative decoders in presence of non-Gaussian noise," *Proceedings of the 2009 IEEE international conference on Symposium on Information Theory*, vol. 2, pp. 904–908, 2009.

[30] A. Tesei, R. Bozzano, and C. Regazzoni, "Comparison between asymmetric generalized Gaussian (AGG) and symmetric-α-stable ($S\alpha S$) noise models for signal estimation in non-Gaussian environments," *Proceedings of the IEEE Signal Processing Workshop on Higher-Order Statistics*, pp. 259–263, July 1997.

[31] A. Teschioni, C. Sacchi, and C. Regazzoni, "Non-Gaussian characterization of DS/CDMA noise in few-user systems with complex signature sequences," *IEEE Transactions on Signal Processing*, vol. 47, no. 1, pp. 234–237, January 1999.

[32] A. Tesei and C. Regazzoni, "The asymmetric generalized Gaussian function: a new HOS-based model for generic noise pdfs," *8th IEEE Signal Processing Workshop on Statistical Signal and Array Processing*, pp. 210–213, June 1996.

[33] W. Henkel and T. Kessler, "A wideband impulsive noise survey in the German telephone network statistical description and modeling," *AEU*, vol. 48, no. 1, pp. 277–288, November 1994.

[34] W. Henkel, T. Kessler, and H. Y. Chung, "Coded 64-CAP ADSL in an impulse-noise environment modeling of impulse noise and first simulation results," *IEEE Journal on Selected Areas in Communications*, vol. 13, no. 13, pp. 1611–1621, December 1995.

[35] T. S. Saleh, I. Marsland, and M. El-Tanany, "Suboptimal detectors for Alpha-Stable noise: simplifying design and improving performance," *IEEE Transactions on Communications*, vol. 60, no. 10, pp. 2982–2989, 2012.

[36] J. Häring and A. J. H. Vinck, "Performance bounds for optimum and suboptimum reception under Class-A impulsive noise," *IEEE Transaction on Communications*, vol. 50, no. 7, pp. 1130–1136, Jul 2002.

[37] S. V. Zhidkov, "Analysis and comparison of several simple impulsive noise mitigation schemes for OFDM receivers," *IEEE Transactions on Communications*, vol. 56, no. 1, pp. 5–9, January 2008.

[38] G. Ndo, P. Siohan, M.-H. Hamon, and J. Horard, "Optimization of turbo decoding performance in the presence of impulsive noise using soft limitation at the receiver side," in *Proc. IEEE Global Telecommunications Conference*, December 2008, pp. 1–5.

[39] G. Ndo, P. Siohan, and M.-H. Hamon, "Adaptive noise mitigation in impulsive environment: application to power-line communications," *IEEE Transactions on Power Delivery*, vol. 25, no. 2, pp. 647–656, April 2010.

[40] K. Gulati, A. Chopra, R. W. Heath, B. L. Evans, K. R. Tinsley, and X. E. Lin, "MIMO receiver design in the presence of radio frequency interference," *IEEE Global Telecommunications Conference*, December 2008.

[41] S. V. Zhidkov, "Performance analysis and optimization of OFDM receiver with blanking nonlinearity in impulsive noise environment," *IEEE Transactions on Vehicular Technology*, vol. 55, no. 1, pp. 234–242, 2006.

[42] ——, "Impulsive noise suppression in OFDM-based communication systems," *IEEE Transactions on Consumer Electronics*, vol. 49, no. 4, pp. 944–948, Nov 2003.

[43] M. E. Tipping, "Sparse Bayesian learning and the relevance vector machine," *Journal of Machine Learning Research*, vol. 1, pp. 211–244, 2001.

[44] D. P. Wipf and B. D. Rao, "Sparse Bayesian learning for basis selection," *IEEE Transactions on Signal Processing*, vol. 52, no. 8, pp. 2153–2164, August 2004.

[45] J. G. Proakis, *Digital communications*. New York: Mc Graw Hill, 1995.

[46] K. McDonald and R. Blum, "A physically-based impulsive noise model for array observations," *Conference Record of the Thirty-First Asilomar Conference on Signals, Systems & Computers*, vol. 1, pp. 448–452, November 1997.

[47] S. Alamouti, "A simple transmit diversity technique for wireless communications," *IEEE Journal on Selected Areas in Communications*, vol. 16, no. 8, pp. 1451–1458, October 1998.

[48] O. Tirkkonen and A. Hottinen, "Square-matrix embeddable space-time block codes for complex signal constellations," *IEEE Transactions on Information Theory*, vol. 48, no. 2, pp. 384–395, February 2002.

[49] J. Lin, M. Nassar, and B. L. Evans, "Impulsive noise mitigation in powerline communications using sparse Bayesian learning," *IEEE Journal on Selected Areas in Communications*, vol. 31, no. 7, pp. 1172–1183, 2013.

[50] V. Tarokh, H. Jafarkhani, and A. R. Calderbank, "Space-time block codes from orthogonal designs," *IEEE Transactions on Information Theory*, vol. 45, no. 5, pp. 1456–1467, July 1999.

[51] J. Häring and A. J. H. Vinck, "OFDM transmission corrupted by impulsive noise," in *In Proc. IEEE Int. Symp. Power Line Communications (ISPLC)*, Apr 2000.

[52] A. Mengi and A. J. H. Vinck, "Successive impulsive noise suppression in OFDM," in *IEEE International Symposium on Power Line Communications and Its Applications (ISPLC)*, March 2010.

[53] S. M. Zabin and H. V. Poor, "Efficient estimation of Class-A noise parameters via the EM algorithm," *IEEE Transactions on Information Theory*, vol. 37, no. 1, pp. 60–72, January 1991.

[54] E. Viterbo and J. Boutros, "A universal lattice code decoder for fading channels," *IEEE Transaction on Information Theory*, vol. 45, no. 5, pp. 1639–1642, Jul 1999.

[55] M. O. Damen, H. E. Gamal, and G. Caire, "On maximum-likelihood detection and the search for the closest lattice point," *IEEE Transaction on Information Theory*, vol. 49, no. 10, pp. 2389–2402, 2003.

[56] Z. Guo and P. Nilsson, "Algorithm and implementation of the K-Best sphere decoding for MIMO detection," *IEEE Journal on Selected Aera In Communications*, vol. 24, no. 3, pp. 491–503, 2006.

[57] K.-W. Wong, C.-Y. Tsui, R. S.-K. Cheng, and W.-H. Mow, "A VLSI architecture of a K-best lattice decoding algorithm for MIMO channels," in *IEEE International Symposium on Circuits and Systems*, May 2002.